Production of light flavor hadrons and anti-nuclei at the LHC

Doctoral Thesis by Alexander Kalweit
May 2012

TECHNISCHE
UNIVERSITÄT
DARMSTADT

Institut für Kernphysik
Prof. Dr. P. Braun-Munzinger
Priv. Doz. Dr. H. Oeschler

Dissertation

Messung der Produktion von aus leichten Quarks zusammengesetzten Hadronen und Anti-Kernen am Large Hadron Collider

Vom Fachbereich Physik
der Technischen Universität Darmstadt

zur Erlangung des Grades
eines Doktors der Naturwissenschaften (Dr. rer. nat.)

genehmigte Dissertation von
M.Sc. Alexander Kalweit
aus Schlüchtern

Referent: Prof. Dr. Peter Braun-Munzinger
Korreferent: Prof. Dr. Jochen Wambach

Tag der Einreichung: 11.05.2012
Tag der Prüfung: 18.07.2012

Darmstadt 2012
D17

Abstract

With the recording of the first collisions of the Large Hadron Collider (LHC) in November 2009, a new era in the domain of high energy and relativistic heavy-ion physics has started. As one of the early observables which can be addressed, the measurement of light quark flavor production is presented in this thesis. Hadrons that consist only of u, d, and s quarks constitute the majority of the produced particles in pp and Pb–Pb collisions. Their measurement forms the basis for a detailed understanding of the collision and for the answer of the question if hadronic matter undergoes a phase transition to the deconfined quark-gluon plasma at high temperatures. The basics of ultra-relativistic heavy-ion physics are briefly introduced in the first chapter followed by a short description of the ALICE experiment. A particular focus is put on the unique particle identification (PID) capabilities as they provide the basis of the measurements which are presented in the following chapters. The particle identification via the specific energy loss in the Time Projection Chamber (TPC) is an essential part of the overall particle identification within the experiment. Its underlying principles, the complex extraction of relevant calibration parameters, and the achieved performance belong to the main topics of this thesis and are presented in the second chapter.

The particle identification with the TPC can be directly used for the extraction of transverse momentum (p_t) spectra of charged pions, kaons, and protons. The analysis, together with its related systematic error, is discussed in detail in the third chapter. In order to enlarge the p_t-range of the spectrum, the analysis presented in this thesis was extended by a combined PID of the TPC $\mathrm{d}E/\mathrm{d}x$ signal together with the information from the Time-of-Flight (TOF) system. Together with two independent analyses, which are based on stand-alone tracking and PID in the Inner Tracking System (ITS) and on a TPC-independent PID with the TOF, a complete p_t-spectrum can be obtained. The different and independent analyses are overlapping in several p_t-intervals and provide thus a useful cross-check of the results. In the fourth chapter, the resulting p_t-spectra of pions, kaons, and protons are put into a larger context based on complementing ALICE measurements on strange particle production. In particular, it is found that the measured particle yields follow the trend from lower energies and that strange particle production in pp collisions is suppressed with respect to Pb–Pb collisions.

The measurement of light anti- and hyper-nuclei is presented in the following chapter. It is shown that nuclei up to the $^4\overline{\mathrm{He}}$ can be observed. The basic identification, reconstruction, and efficiency correction techniques for anti- and hyper-nuclei are outlined. In addition to this, trigger strategies for future running and searches for unknown hyper-matter states are briefly discussed. The thesis concludes in the last chapter with an interpretation of the obtained results based on hydrodynamical and thermal models. In particular, preliminary thermal fits of the measured particle yields are shown.

Zusammenfassung

Mit dem Aufzeichnen der ersten pp und Pb–Pb Kollisionen am Large Hadron Collider (LHC) im November 2009 begann eine neue Epoche in der Hochenergie- und relativistischen Schwerionenphysik. Die in dieser Arbeit beschriebene Messung der Produktion von Hadronen, welche aus den leichten u, d und s Quarks aufgebaut sind, wird typischerweise bereits in relativ kurzer Zeit nach Beginn des Experimentes durchgeführt. Dies liegt zum einen in der Tatsache begründet, dass diese Teilchen mit viel größerer Häufigkeit entstehen als solche aus schweren c oder b Quarks. Zum anderen bildet diese Messung die Basis für die Interpretation weiterer Observablen und damit ein detaillierteres Verständnis der Kollision, insbesondere im Hinblick auf die entscheidende Frage, ob die in den Kollisionen entstehende hadronische Materie bei hohen Temperaturen in einer Phase vorliegt, in der das *confinement* der Quarks aufgehoben ist. Letztere Eigenschaft beschreibt das Verhalten von Quarks, unter normalen Umgebungsbedingungen immer in farbneutralen Zuständen gebunden zu sein. Im Gegensatz dazu sind Quarks und Gluonen in der sogenannten Quark-Gluon-Plasma Phase nicht mehr zu einzelnen Hadronen lokalisierbar. Eine Voraussetzung dafür ist das Vorliegen eines Mediums im lokalen thermischen Gleichgewicht und damit die Anwendbarkeit thermodynamischer und hydrodynamischer Konzepte, welche in dieser Arbeit auf der Basis von Transversalimpulsspektren von Pionen, Kaonen und Protonen überprüft wird.

Die Grundlage für die Extraktion der entsprechenden Spektren ist die Identifikation der entsprechenden Teilchen. Das ALICE Experiment unterscheidet sich von den anderen großen LHC Experimenten ATLAS und CMS vor allem dadurch, dass in ihm alle bekannten Technologien zur Teilchenidentifizierung zur Anwendung kommen: spezifischer Energieverlust $\mathrm{d}E/\mathrm{d}x$, Übergangstrahlung, Flugzeitmessungen, Cherenkov-Strahlung und Kalorimetrie. Die entsprechenden Sub-Detektoren werden im ersten Kapitel dieser Arbeit vorgestellt. Die Teilchenidentifizierung über den spezifischen Energieverlust, welcher durch die Bethe-Bloch Funktion beschrieben werden kann, und die Vielzahl der dazu benötigten Kalibrierungen bilden einen Schwerpunkt der vorliegenden Arbeit und werden im zweiten Kapitel detailliert dargestellt. Die Angleichung der Signalstärke der 557 568 Auslesekanäle erfolgt mit Hilfe von radioaktivem Krypton-Gas, welches in das TPC Gasvolumen eingeleitet wird. Weiterhin muss beispielsweise die Abhängigkeit der Gasverstärkung als Funktion des Luftdrucks permanent berücksichtigt werden. Da die ALICE TPC insbesondere für Pb–Pb Kollisionen optimiert wurde, müssen auch multiplizitätsabhängige Effekte beachtet werden. Nach Berücksichtigung aller notwendigen Korrekturfaktoren kann eine $\mathrm{d}E/\mathrm{d}x$-Auflösung von ca. 5.2% und eine entsprechende Separation von ca. 11.5σ zwischen minimal ionisierenden Teilchen und Teilchen auf dem Fermi-Plateau erreicht werden, welche sogar die erwarteten Werte des Technischen Design Reports leicht übertrifft.

Die mit Hilfe der TPC identifizierten Pionen, Kaonen und Protonen bilden die Basis der entsprechenden p_t-Spektren. Die entsprechende Analyse wird zusammen mit der benötigten Korrektur für die Detektoreffizienz im zweiten Kapitel der vorliegenden Arbeit vorgestellt. Um den abgedeckten Bereich bezüglich des Transversalimpulses zu vergrößern, werden die erzielten Resultate mit unabhängigen Analysen basierend auf dem Energieverlust im Inner Tracking System und Flugzeitmessungen im TOF kombiniert. Die Spektren der individuellen Detektoren stimmen in den überlappenden Bereichen innerhalb von 5% in pp und 10% in Pb–Pb Kollisionen überein. Die zwei wichtigsten charakteristischen Größen der Spektren, der mittlere Transversalimpuls $\langle p_t \rangle$ und die integrierte Anzahl der produzierten Teilchen je Einheit Rapidität $\mathrm{d}N/\mathrm{d}y$, werden mit Hilfe entsprechender Fits in pp und Pb–Pb Kollisionen extrahiert.

Im darauffolgenden Kapitel werden die so erhaltenen Ergebnisse mit komplementären Messungen von Hadronen aus leichten Quarks (K_S^0, Λ, Ξ, Ω) verglichen, um sie in einen größeren Zusammenhang einzuordnen. Im Allgemeinen zeigt sich, dass sich die relative chemische Zusammensetzung der produzierten Teilchen nur leicht im Vergleich zu niedrigeren Energien verändert. Dies entspricht der Vorhersage des thermischen Modells, die genauer im abschließenden Kapitel diskutiert wird. Darüber hinaus ergibt sich, dass auch bei LHC Energien die Produktion von Teilchen mit Strange-Quarks in Pb–Pb Kollisionen weniger stark unterdrückt ist als in pp Kollisionen. Die Interpretation der Form der Spektren erfolgt auf der Basis von hydrodynamischen Methoden, die eine gute Beschreibung ermöglichen.

Die Messung von leichten Anti- und Hyper-Kernen wird im fünften Kapitel dargestellt. Mit der gegenwärtig zur Verfügung stehenden Statistik ist die Beobachtung von Anti-Kernen bis $^4\overline{\mathrm{He}}$ möglich. Die grundlegenden Techniken zur Identifikation und Effizienz-Korrektur dieser seltenen Teilchen werden gezeigt. Darüber hinaus werden als Ausblick mögliche Trigger-Konzepte präsentiert und die Suche nach exotischen Zuständen, insbesondere eines gebundenen Di-Baryons aus einem Lambda und einem Neutron, vorgestellt.

Contents

1 The ALICE experiment

Quantum chromodynamics (QCD), the theory of the strong interaction, predicts that nuclear matter at extreme temperature and densities transforms into a deconfined state - the quark-gluon plasma (QGP). This phase probably existed in the early universe from 10 ps until 10 μs after the big bang and might still exist in the core of dense neutron stars. On earth, a possibility to reach these energies and densities is given by relativistic heavy-ion collisions at large particle accelerators, like the Large Hadron Collider (LHC) at the European Particle Physics Laboratory CERN in Geneva. The main purpose of the ALICE (A Large Ion Collider Experiment) experiment is the measurement of signatures of this phase transition from the QGP to a confined hadronic state. In addition to this, its unique capabilities for particle identification and continuous track reconstruction from very low to very high p_t allow to complement the LHC physics program in pp collisions.

In general, the natural system of units with $\hbar = c = k_B = 1$ is used in this thesis. Chapter 2 presents an exception because of its direct relation to experimental quantities. In addition to this, the lifetimes of particles and the labels of official ALICE plots are written in the SI system of units.

1.1 Hadronic matter under extreme conditions

In QCD, the fundamental matter constituents are quarks which carry color charge. Gluons act as exchange bosons of the interaction in analogy to virtual photons mediating the electromagnetic interaction in QED. In contrast to QED, gluons carry color charge and can interact which each other. Table 1.1 summarizes the basic properties of the six quark flavors. Please note the different mass scale in the quark masses. The *light* flavors u, d, and s with masses in the MeV regime are clearly separated from the *heavy* flavors b and c and are thus produced much more abundantly.

Quark Flavor	Symbol	Weak Isospin	I_z	S	C	B	T	Charge $z \cdot e$	Mass (GeV)
up	u	+1/2	+ 1/2	0	0	0	0	+ 2/3	0.0015 – 0.003
down	d	– 1/2	– 1/2	0	0	0	0	– 1/3	0.003 – 0.007
charm	c	+1/2	0	0	1	0	0	+ 2/3	1.25 ± 0.09
strange	s	– 1/2	0	– 1	0	0	0	– 1/3	0.07 – 0.12
top	t	+1/2	0	0	0	0	1	+ 2/3	174.2 ± 3.3
bottom	b	– 1/2	0	0	0	– 1	0	– 1/3	4.2 – 4.7

Table 1.1: Basic properties of quarks including the current quark mass [1].

An interesting consequence of the fact that gluons carry color charge is the large variation of the strong coupling constant α_s as a function of the transferred momentum Q^2 in the interaction as shown in figure 1.1.

1.1.1 Properties of the strong interaction

In QED, the intensity of the electromagnetic interaction is given by the QED coupling constant. At small values of Q^2 it is given by the value of the fine-structure constant $\alpha \approx 1/137$. It only increases weakly towards larger values of Q^2 due to vacuum polarization. Since $\alpha \ll 1$, perturbation theory methods can be applied and cross-sections are calculated in expansion powers of α. In QCD, the dependence of α_S on Q^2 in first order is given by

$$\alpha_S(Q^2) \approx \frac{12\pi}{(33 - 2n_f) \cdot \ln(Q^2/\Lambda^2_{QCD})}\,, \tag{1.1}$$

where n_f is the number of participating quark flavors. The values of n_f range between 3 and 6 as heavy quark flavors only contribute at higher values of Q^2. Λ_{QCD} is the QCD scale parameter and the only free intrinsic parameter in QCD. It is determined by comparing QCD predictions with experimental observations and has a value of approximately $\Lambda_{QCD} \approx 250$ MeV.

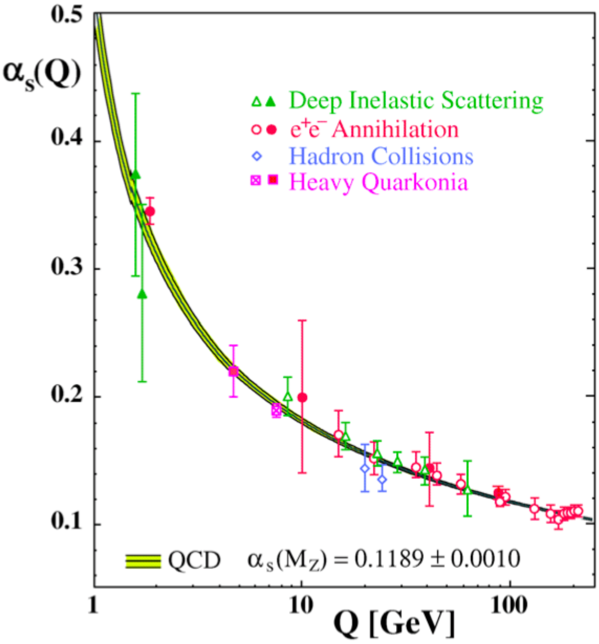

Figure 1.1: Variation of the strong coupling constant α_S as a function of the momentum transfer Q. From [2].

At large distances and small values of Q^2, the strong coupling α_S has large values ($\alpha_S > 1$). The quarks are bound in neutral color states, either in mesons ($q\bar{q}$-pairs) or baryons (qqq). This property is known as *confinement*. As perturbative calculations are impossible in this regime, non-perturbative theories as lattice QCD or effective models have to be used. At short distances or large values of Q^2, respectively, α_s decreases continuously until the quarks behave as quasi free particles: $\alpha_s \to 0$ for $Q^2 \to \infty$. This behavior is known as *asymptotic freedom* [3, 4]. One of the consequences is the applicability of perturbative calculations to hard QCD processes where $Q^2 \gg \Lambda_{QCD}$.

In a rather phenomenological way, the quark-antiquark potential is often taken to be of the form [5]

$$V_s = -\frac{4}{3}\frac{\alpha_s(r)}{r} + kr\,, \tag{1.2}$$

where the first term arises from the single-gluon exchange similar to the single-photon exchange of the Coulomb potential. The linear increase at larger separations is caused by the already mentioned self-interaction between gluons and described by the string tension $k \approx 880$ MeV/fm.

1.1.2 The QCD phase diagram

Even in everyday life we realize that matter comes in various forms and we distinguish between the solid, liquid and gas phase. Transitions between phases can be achieved by variations of external conditions or control parameters. Similarly in QCD, a fascinating consequence of asymptotic freedom appears at high temperatures or densities. The quarks and gluons become free and are not localized in individual hadrons. They form a deconfined phase of matter which is referred to as the *quark-gluon plasma* (QGP) [6, 7]. This phase probably existed in the early universe shortly after the Big Bang starting after the elektroweak phase transition (t > 10 ps) and lasting for about 10 μs. On earth, a possibility to create the QGP is given by ultra-relativistic heavy-ion collisions.

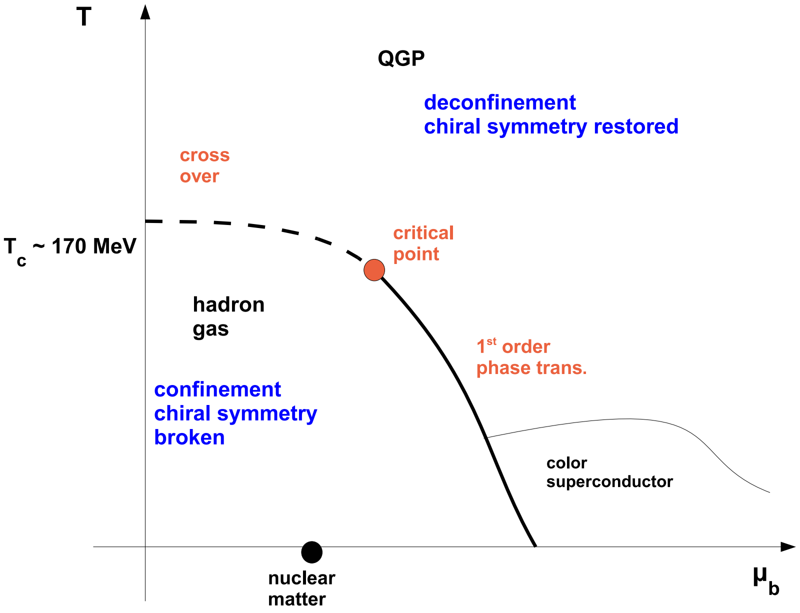

Figure 1.2: Schematic phase diagram of the strong interaction.

Thermodynamical information is often presented in the form of a phase diagram, in which the different manifestations of matter are shown as different regions as a function of the control parameters. In the case of QCD, the control parameters are the temperature T and the baryo-chemical potential μ_B. The baryo-chemical potential measures the net baryon density of the system and corresponds to the conservation of the baryon number $B = N_B - N_{\bar{B}}$ which is given by the number of baryons minus the number of anti-baryons in the hadronic phase (see also chapter 6.2). Figure 1.2 shows a schematic version of the QCD phase diagram. The phase transition between confined hadronic matter and the QGP is expected to be a first order phase transition at lower temperatures and high net baryon densities. At small net baryon densities and high temperatures - as they are expected in Pb–Pb collisions at the LHC and in the early universe - several models and calculations indicate a change into a continuous, but rapid crossover transition [8].

The phase transition temperature T_c can be estimated with simple approaches like the bag model (see appendix C) leading to temperatures of the order of 100-200 MeV. Modern lattice QCD calculations allow to investigate the phase transition at vanishing net baryon densities with much more precision. Recent results indicate a cross-over temperature of about 160 MeV [9, 10].

1.1.3 Relativistic heavy-ion collisions

Collisions of relativistic heavy-ions provide the only tool to probe matter at such high temperatures and densities in the laboratory. It is important to distinguish between a system of individual particles and a medium to which thermodynamical concepts can be applied. Thermodynamic concepts are typically used for locally equilibrated systems in the regime of 10^5 – 10^{23} particles. Even at LHC energies, average elementary particle collisions of protons ($\mathrm{d}N_{ch}/\mathrm{d}\eta|^{\eta=0}_{7TeV} = 6.01 \pm 0.2$) or electrons do not produce enough particles to fulfill such conditions. In contrast to this, central heavy-ion collisions provide a much larger system ($\mathrm{d}N_{ch}/\mathrm{d}\eta|^{\eta=0}_{2.76TeV} = 1584 \pm 74$) [11, 12]. In order to reach local equilibrium, the lifetime of the system must be large enough so that at least several (simulations indicate approximately 5-6) interactions occur for each constituent. The success of statistical models in the description of hadron yields and of hydrodynamical models in the description of flow effects strongly supports the idea of matter in local equilibrium (see chapter 6). The question if similar observations hold true for high multiplicity elementary collisions is an interesting topic of ongoing research and is addressed in chapter 4.3.

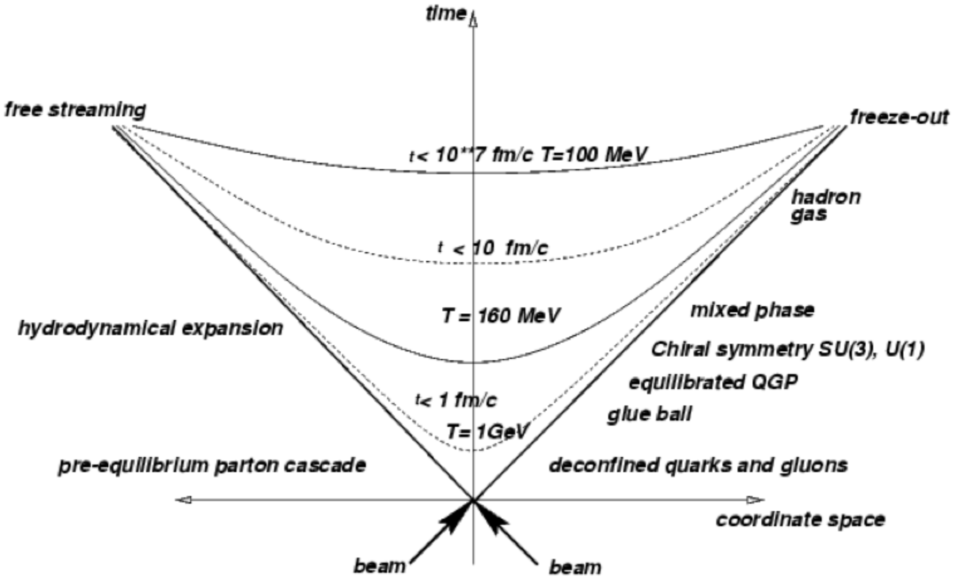

Figure 1.3: Schematic diagram of the space-time evolution of an ultra-relativistic nucleus-nucleus collision indicating the different stages of the collision. From [13].

The different stages of an ultra-relativistic heavy-ion collision are schematically illustrated in figure 1.3. The two nuclei are transparent for each other as they pass through in a crossing time $t_{cross} \approx 2R/\gamma \approx 10^{-2}$ fm which is much smaller than the typical timescale of the strong interaction $t_{strong} \approx 1/\Lambda_{QCD} \approx 1$ fm. We also note, that the crossing time t_{cross} as well as t_{strong} are much smaller than the transverse size of the nucleus. The initial energy density can be assessed in the Bjorken model [14] following

$$\epsilon(\tau) = \frac{1}{\tau A_{trans}} \frac{\mathrm{d}E_T}{\mathrm{d}y}|_{y=0}\,, \tag{1.3}$$

where A_{trans} is the transverse area of the incident nuclei and $\mathrm{d}E_T/\mathrm{d}y$ denotes the transverse energy of the collision products per unit of rapidity. If we assume that thermalization occurs in a typical QCD time-scale $\tau = t_{strong}$, we find that temperatures above $3 \cdot T_c$ should be reached at the LHC.

After a pre-equilibrium phase, the system reaches thermal equilibrium in an early stage of the collision. From then on, the space-time evolution can be described within hydrodynamical models. The assumed QGP system then expands adiabatically and cools down until the phase-transition temperature T_c is reached. The system stays at constant temperature until all partons have frozen out into hadrons. The hadron gas then further expands until inelastic collisions stop to occur at the chemical freeze-out. At this point, the particle yields are frozen. The momentum spectra can still change until elastic collisions stop to occur and the kinematic freeze-out is reached.

Experimental signatures of the QGP

Due to confinement and its short lifetime, a direct observation of the quark-gluon plasma is impossible. However, during the last decades numerous experimental signatures were proposed and to some extent verified in different experiments at SPS, RHIC, and now at the LHC. In this context, already the observation of hadron yields which are in agreement with statistical model predictions of an equilibrated system at the phase boundary is interesting (see chapter 6 for details). As the collision rates and timescales in the hadronic phase are too small to achieve the equilibrium, it could be that multi-particle collisions during hadronization [15] drive the system to equilibrium. In the following section, only two further signatures will be outlined briefly; for a more detailed discussion see e.g. [16] and references therein.

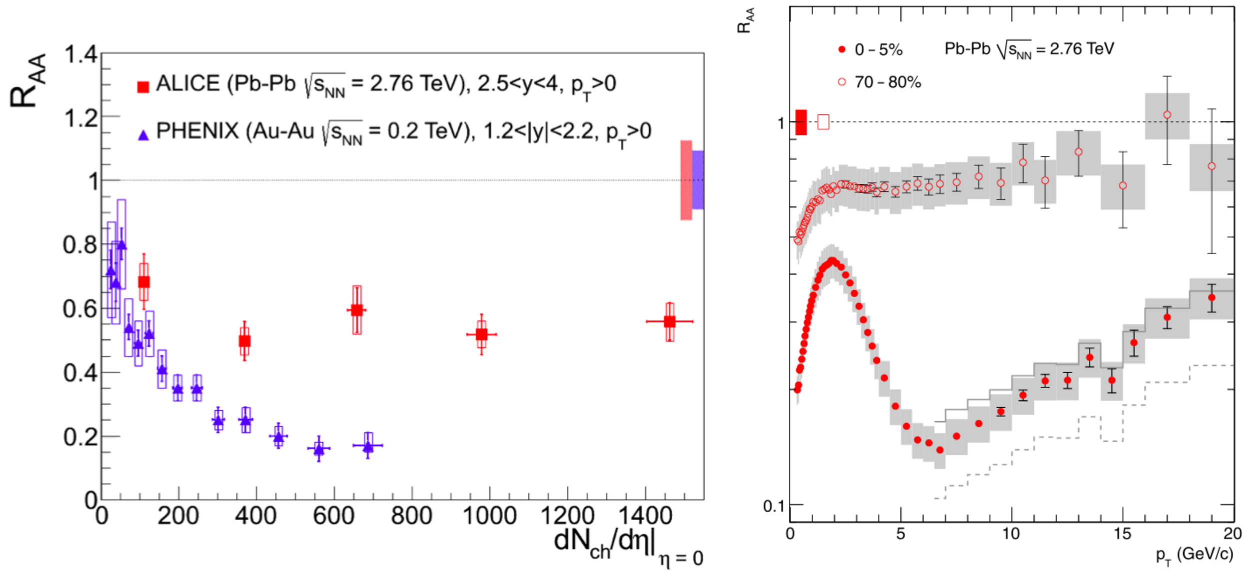

(a)

(b)

Figure 1.4: Nuclear modification factor for J/ψ-production as a function of charged particle density (left) and for charged particles as a function of transverse momentum (right). From [17] and [18]. Please note that the charged particle density is proportional to the energy density of the system.

J/ψ-suppression and enhancement. At the high density of gluons in a quark-gluon plasma, one expects that bound charmonium systems like the J/ψ are dissolved by screening effects [19].

At low energies, the mean number of charm-quark pairs produced in a collision is less than 1. Consequently, a suppression of charmonium is expected and was observed in this case. Unfortunately, there are as well other explanations for this observation which do not imply the formation of a quark-gluon plasma.

In a central Pb–Pb collision at top LHC energies however, up to 100 charm quark pairs are produced. Quarks from different pairs can combine to charmonium at the phase boundary, if the quarks can travel freely over large distances which is made possible by the QGP. Then the charmonium production scales quadratically with the number of charm quarks which would lead to a net enhancement of charmonium production. Finding an enhancement of charmonium production at the LHC would thus provide a unique signature of deconfinement [20, 21]. The first results at LHC already indicate that the production of J/ψ is less suppressed than at RHIC energies (see figure 1.4(a)).

Similar arguments can be made for bottomonium systems such as the Υ. As the production cross section for bottom quarks is significantly smaller than for charm quarks, they would remain suppressed also at LHC energies. Both particles are measured via their decays in the di-electron or di-muon channel, e.g.

$$J/\psi \rightarrow e^+ + e^- \quad (5.9\%)\,, \tag{1.4}$$

requiring a very good identification of electrons or muons.

Suppression of charged particle production at high $\mathbf{p}_t$. Hard scattering events between partons occur in heavy-ion collisions just as in proton-proton collisions. The number of such scattering processes scales with the number N_{coll} of individual nucleon-nucleon collisions. Under the assumption that they occur independently from each other, their number can be calculated from the distributions of nuclear densities, the nuclear overlap for a given impact parameter and the inelastic proton-proton cross-section (see appendix B). If a QGP is formed during the collision between nuclei, the partons might traverse it.

The two scattered partons form a jet by hadronizing mainly into mesons which are then emitted in a cone around the initial parton momentum. The observation of jets in heavy-ion collisions is much more difficult than in proton-proton collisions because of the larger number of particles, but their presence changes the transverse momentum spectra. The difference is typically quantified with the help of the nuclear modification factor

$$R_{AA} = \frac{\frac{\mathrm{d}^2 N_{AA}}{\mathrm{d}y\,\mathrm{d}p_t}}{N_{coll} \cdot \frac{\mathrm{d}^2 N_{pp}}{\mathrm{d}y\,\mathrm{d}p_t}}\,. \tag{1.5}$$

It is thus found that the production of high-momentum particles is suppressed by a factor of about seven in Pb–Pb compared to pp collisions (see figure 1.4(b)). The explanation of this modification is that partons flying through a hot and dense medium should lose substantially more energy by gluon bremsstrahlung than in cold nuclear matter. Initially produced hard photons can serve as a cross-check tool, because they are not subject to the strong interaction and hence leave the fireball without disturbance.

1.2 The ALICE experiment at the CERN LHC

The ALICE experiment is designed to investigate Pb–Pb and pp collisions in the unprecedented energy regime of the Large Hadron Collider. It is the only experiment at the LHC optimized for the analysis of heavy-ion reactions and can handle charged particle densities of up to $\mathrm{d}N/\mathrm{d}y \approx 8000$. In order to allow the study of soft observables, ALICE is the experiment with the lowest material budget in the central rapidity region and magnetic field among the four major LHC experiments.

1.2.1 General overview

The ALICE experiment has an overall length of 25 m, a diameter of 16 m and a weight of approximately 10000 t. The central detector part is housed in the homogeneous magnetic field of the L3-magnet with a maximal strength of 0.5 T. In forward direction, one can find the additional muon arm which is located outside the central magnetic field. In the following section, the main detector components are described (from the beam-pipe to the outside) with a particular focus on their capabilities for particle identification. The ALICE experiment exploits all known techniques for particle identification. This focus of the experiment on particle identification makes ALICE also unique among the four major LHC experiments and thereby allows also to complement the LHC pp physics program.

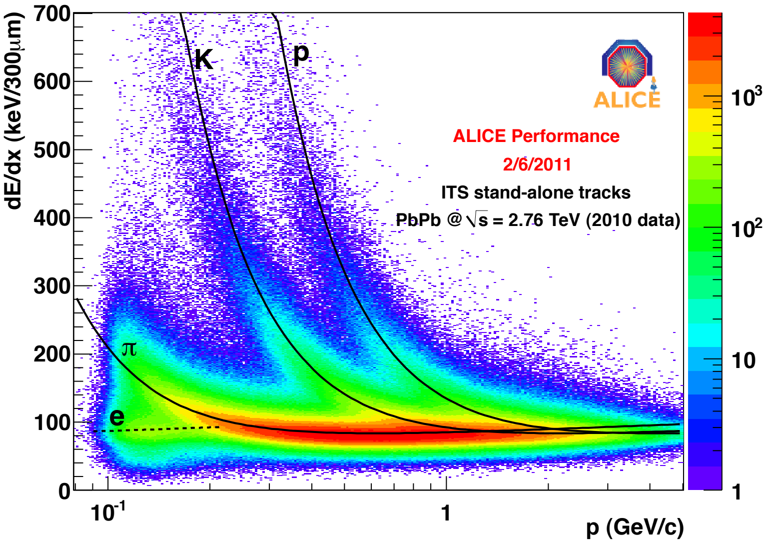

Figure 1.5: $\mathrm{d}E/\mathrm{d}x$ spectrum of the ITS.

The Inner Tracking System (ITS)

The Inner Tracking System consists of six cylindrical layers of high resolution position sensitive silicon detectors. The distance to the beam axis is 4 cm for the innermost and 43.6 cm for the outermost detector. The two inner sub-detectors are silicon pixels (SPD), followed by two silicon drift layers (SDD) and two double-sided silicon strip layers (SSD). The main task of the ITS is the precise determination of primary and secondary vertices in the region of high track density close to the primary interaction. Furthermore, the analog read-out of the SDD and SSD provide up to four samples for the particle identification via $\mathrm{d}E/\mathrm{d}x$ at small transverse momenta. Resolutions of the order of $\sigma_{dEdx} \approx 10-12\%$

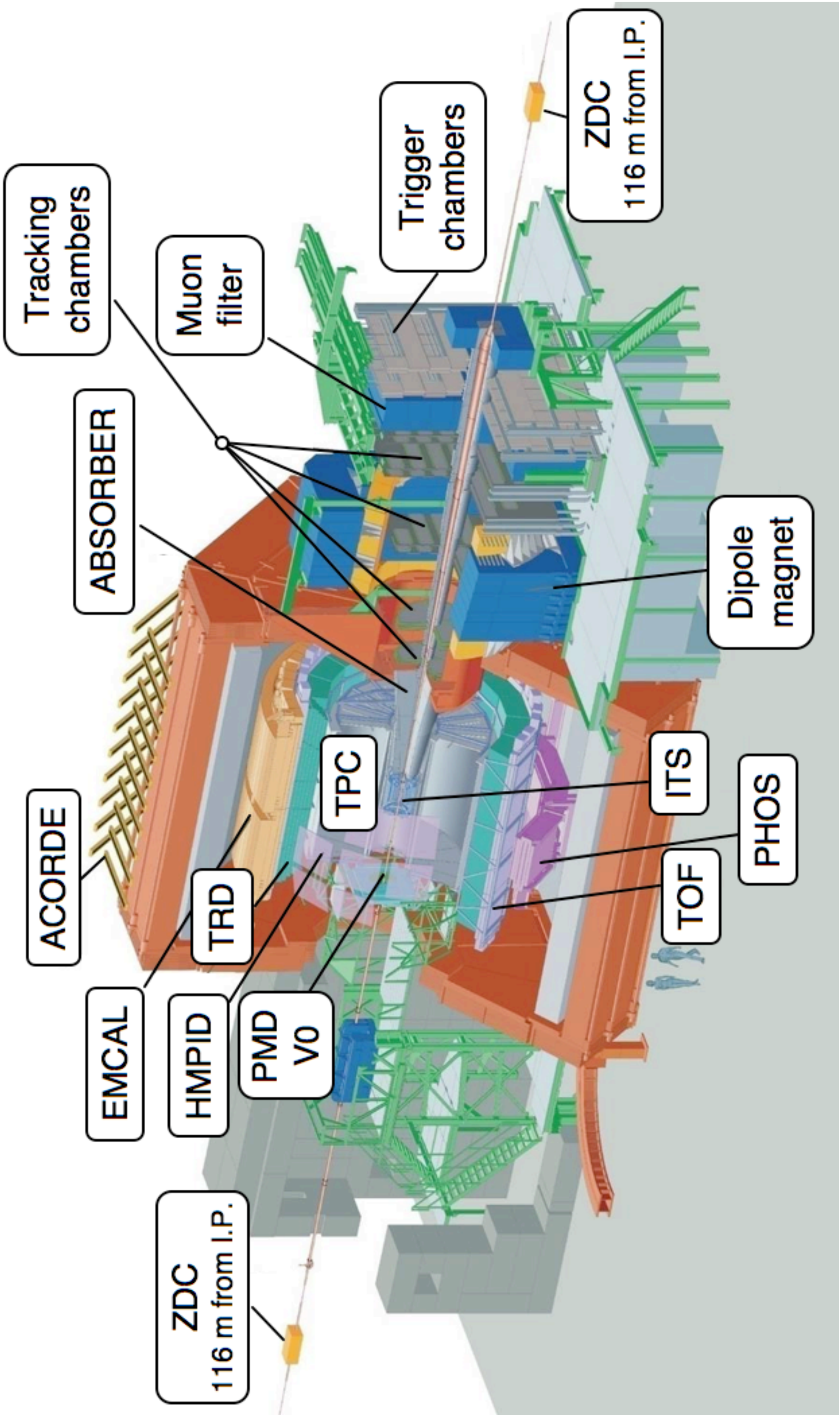

Figure 1.6: A cut view on the Alice experiment.

can be achieved. In a stand-alone tracking mode, pions with $p_t \approx 100$ MeV can still be reconstructed and identified allowing to reduce the systematics of yield extraction when extrapolating to the unmeasured region at low p_t. Figure 1.5 shows the obtained dE/dx vs. momentum spectrum in Pb–Pb collisions.

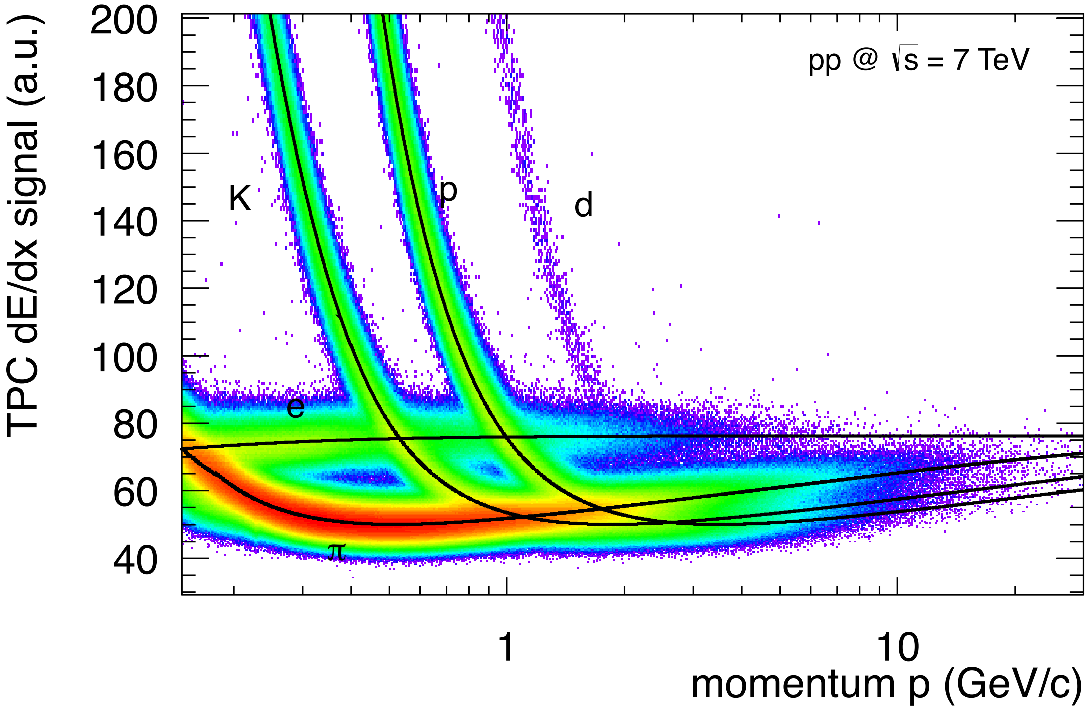

Figure 1.7: dE/dx spectrum of the TPC.

The Time Projection Chamber (TPC)

The TPC is the main detector for track reconstruction and particle identification via specific energy loss in ALICE [22]. It is of a cylindrical shape with a length of 5 m and an inner radius of approximately 80 cm and an outer radius of approximately 250 cm. As the particle identification via specific energy loss is one of the main topics of this thesis, a detailed description of the underlying principles, the necessary calibrations, and the achieved performance is given in section 2.1. Figure 1.7 shows a typical dE/dx vs. momentum spectrum from pp collisions at 7 TeV.

The Transition Radiation Detector (TRD)

The TRD consists of radiators and a multiwire proportional chambers. If a charged particle with $\gamma > 1000$ travels through the complex structure of hundreds of interfaces with different dielectrical constants in the radiator, transition radiation (TR) in the form of X-rays is emitted with some probability. The signal observed in the high-Z gas mixture of the chamber (Xe and CO_2 in the proportions 85%/15%) is a combination of absorbed TR photons and the ionization by the particle. Due to the small electron mass compared to the one of the pion, a clear separation of these particles can be achieved in a momentum region where an identification via specific energy loss is no longer applicable. Figure 1.8 illustrates the achieved separation between the two particle species.

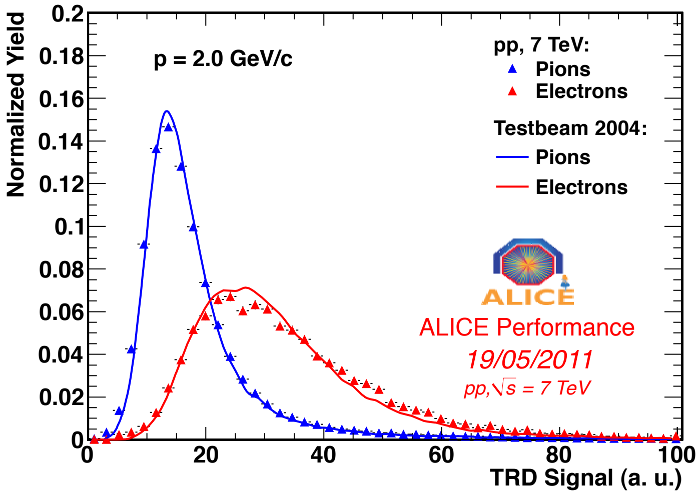

Figure 1.8: Signal amplitude for electrons and pions in the TRD.

In addition to this, the TRD is fast enough and its electronics is designed such that it can serve as a Level-1 trigger for the experiment. Triggering on medium and high p_t-electrons in order to enhance the available statistics of J/ψ and Υ particles is as well possible as a trigger on jets. A possible selection of light nuclei candidates based on similar techniques as for the electron trigger is currently under study (see chapter 5).

The Time-of-Flight Detector (TOF)

The Time-of-Flight detector is built for particle identification by flight time measurements in momentum regions where energy loss measurements are not sufficient enough. It is also the last station of the tracking chain. It consists of multi-gap resistive plate chambers (RPC) at a radial distance of 3.7 m from the beam line. The particle identification within the TOF system is completely independent of energy loss measurements. With a known momentum $p = m\beta\gamma$ the mass of a particle traveling along a track of length l in a time t is given by:

$$m = p \cdot \sqrt{\frac{t^2}{l^2} - 1}\,. \tag{1.6}$$

The 1638 individual chambers provide an intrinsic resolution of approximately 80 ps. The overall time resolution for particle identification also depends on the time-0 uncertainty of the event. This results in a resolution of $\sigma_{TOF} = \sqrt{\sigma_{intr}^2 + \sigma_{t0}^2} \approx 86$ ps for Pb–Pb collisions and $\sigma_{TOF} \approx 120$ ps for pp collisions. Hence a 2σ-separation between protons and kaons up to a momentum of 5 GeV can be achieved in the high-multiplicity environment (see figure 1.9 left). In practice, one usually looks at the difference between the measured time-of-flight and the expected arrival time for a given mass hypothesis or at m^2-distributions in which the signal shape is not distorted.

The High Momentum Particle Identification Detector (HMPID)

The HMPID is a proximity focusing Ring Imaging Cherenkov Detector with a liquid C_6F_{14} radiator. If a charged particle flies through a medium with a velocity higher than the speed of light in the medium, electromagnetic radiation is emitted in the form of a cone. The opening angle of the cone (or radius of the ring on the detection plane) contains information on the particle velocity. The acceptance covers $|\eta| < 0.49$ in pseudorapidity and $\Delta\varphi = 58°$ in azimuth. It provides a separation of kaons and protons up to a momentum of 5 GeV/c independent of the collision system. Figure 1.9 shows the Cherenkov angle vs. momentum distribution for tracks which were matched to the HMPID detector.

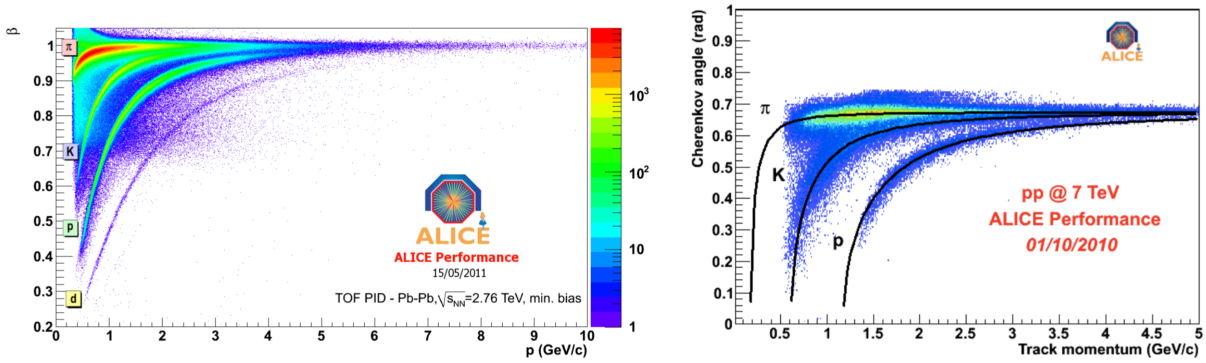

(a)

(b)

Figure 1.9: Track velocity β vs. momentum p from the TOF (left) and Cherenkov angle vs. track momentum for particles detected in the HMPID (right).

The VZERO detector

The VZERO detector consists of two rings of plastic scintillators which are read out with optical fibres. Its 32 scintillator tiles cover the full azimuth within $2.8 < \eta < 5.1$ (VZERO-A) and $-3.7 < \eta < -1.7$ (VZERO-C). It is mainly used for triggering and for the rejection of beam-gas events. In Pb–Pb collisions, it can be reliably used to determine the centrality of the event.

2 Particle identification and calibration of the ALICE Time Projection Chamber

The ALICE Time Projection Chamber is the largest TPC ever built. Large volume TPCs have the unique advantage that they combine excellent tracking and particle identification capabilities within a single detector. Thus, they can provide an almost complete picture of the collision. Please note, that in this chapter all formulas are written in the SI system of units because of their direct relation to experimental quantities.

2.1 The ALICE Time Projection Chamber

The ALICE TPC consists of two main parts: the field cage and the read-out chambers which are located at the end-plates (see figure (2.1)). The common gas volume is filled with a gas mixture of Neon, Nitrogen and CO_2. In the data taking from summer 2008 (cosmics) until the end of 2010, the TPC was filled in the proportions 90 Ne / 10 CO_2 / 5 N_2. Afterwards, the Nitrogen was removed from the gas mixture and a gas mixture of 90 Ne / 10 CO_2 was used.

If a charged particle travels through the gas volume, it excites and ionizes gas atoms along its track. As a consequence, it loses an amount of energy per unit track length ($\mathrm{d}E/\mathrm{d}x$) which is specific for each particle type.

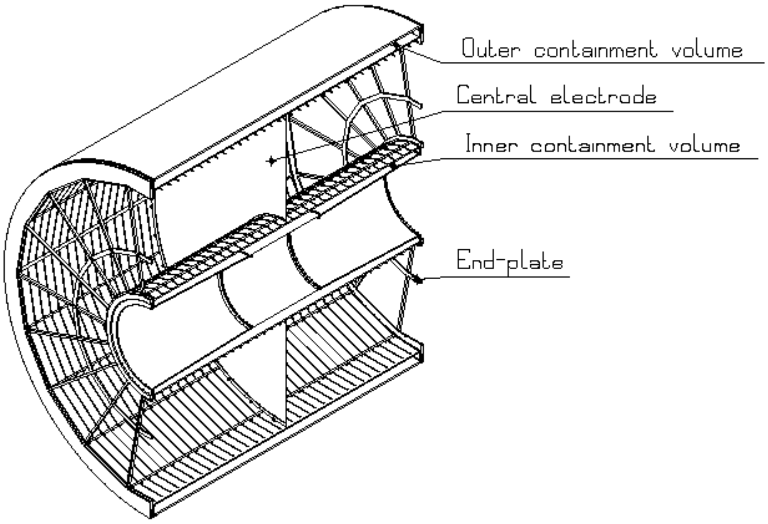

Figure 2.1: A cut view of the TPC. The read-out chambers are positioned close to the end plates.

Inside the field cage, a homogeneous electric field perpendicular to the read-out chambers is generated: the cathode plane of the read-out chambers is at a potential of 0 V and, in the middle of the TPC, the parallel central electrode is set to a negative voltage of 100 kV. At the borders of the field cage, the homogeneity of the field is achieved by special equipotential strips which are connected by a voltage divider. Every strip is put to a potential that its center would have in a homogeneous field.

The electrons created by ionization processes are accelerated along the field lines interrupted by collisions with gas molecules. Thus, their velocity is limited to

$$v_D = a\tau = \frac{eE}{m}\tau = \mu E\,, \tag{2.1}$$

where e is the electron charge, m the electron mass, τ the average time between collisions, E the electric field, and μ the mobility. This discontinuous motion appears macroscopically as a constant drift with the velocity v_D. Ions drift much slower than electrons due to their significantly larger mass which can lead to the creation of a substantial amount of space charge in the gas volume. Because of diffusion processes an electron cloud, which is point-like at its origin, shows a Gaussian density distribution ρ after time t [23]:

$$\rho = \frac{1}{\sqrt{4\pi D_L t}}\left(\frac{1}{\sqrt{4\pi D_T t}}\right)^2 \exp\left(-\frac{x^2+y^2}{4D_T t} - \frac{(z-v_D t)^2}{4D_L t}\right), \tag{2.2}$$

where D_L and D_T are the longitudinal and transverse diffusion constants. The magnetic field reduces the transverse diffusion by the factor

$$\frac{D_T(\omega)}{D_T(0)} = \frac{1}{1+\omega^2\tau^2}\,, \tag{2.3}$$

where $\omega = \frac{eB}{m}$ is the cyclotron frequency.

However, not all electrons reach the read-out chambers, because they attach to electronegative molecules like O_2. Therefore impurities in the counting gas must be kept as low as possible.

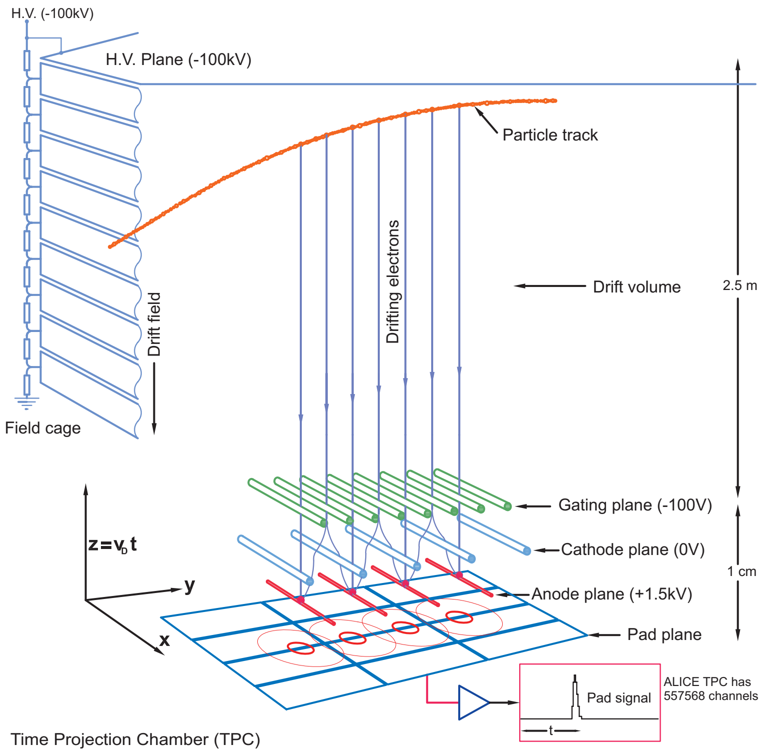

Figure 2.2: Schematic illustration of the working principle and the read-out chambers of the TPC. Picture taken from [24].

The read-out chamber is a multi-wire proportional chamber (MWPC) shown in figure 2.2. It consists of a segmented cathode pad plane and the anode, cathode, and gating wire planes. The anode wires are set to a positive voltage of 1500 V which leads to an amplification of the drifted electrons: in the vicinity of the wire, the electric field grows proportional to $\frac{1}{r}$. The electron energy rises which leads to ionization processes and the released electrons themselves cause further ionization - an avalanche process starts. Since the MWPCs are operated in proportional mode, the generated signal on the pads is proportional to the number of primary electrons and the energy loss of the projectile, respectively. This proportionality would break down if photons - that are generated in the avalanche - travel further than the longitudinal avalanche size and start another avalanche. This effect is minimized by the quenching gases CO_2 and N_2, which exhibit large photoabsorption coefficients over a broad wavelength range.

The read-out plane is segmented in inner (IROC) and outer read-out chambers (OROC). In total, there are three different pad sizes as shown in table 2.1. The pad sizes increase from the inner to outer wall following the decrease of the occupancy (see also figure 2.5). As a matter of fact, most calibrations must be treated separately for each pad region and thus repeated three times.

pad type	rows	size (mm^2)
short (IROC)	63	4 x 7.5
medium (OROC)	64	6 x 10
long (OROC)	32	6 x 15

Table 2.1: The different pad regions in the ALICE TPC.

The gating wires are alternatingly put to a negative and positive potential. In the latter case, the field lines end on the gating grid, drifted electrons do not reach the amplification region and positive ions generated during the amplification process cannot drift back in the direction of the central electrode which could lead to field distortions. The gating grid is only opened if one wants to read out a certain event.

This setup allows a three dimensional reconstruction of the track of the incident charged particle. Two dimensions (x and y) are accessible via the distribution of the induced signal on the pads and the z-dimension is given by the measurement of the drift time Δt. The measurement is started via the trigger system whenever a good event is expected. Together with the known drift velocity of electrons v_e in the gas, the $z-$component is easily calculated via $z = v_e \cdot \Delta t$. The resolution in z-direction and along the anode wires (one pad row) is improved by the determination of the center of gravity of the charge distributions.

2.2 Passage of charged particles through matter

Besides other track parameters, ionization plays a special role because it is a function of the particle velocity. Thus, a combined measurement of momentum and energy loss offers the possibility to determine the particle mass or its identity, respectively. As a matter of fact, only relative values of the ionization need to be known to distinguish between different particle types. With a TPC in a magnetic field like in ALICE, the simultaneous measurement of both quantities is routinely achieved. The specific energy loss is also measured by the ITS and TRD, but with much less precision.

Whenever a charged particle passes through matter, two main processes occur many times per unit path length:

1. A loss of energy by the particle caused by inelastic collisions with the atomic electrons of the material. The particle's energy loss is generally small in respect to its total energy - especially for the conditions given in the ALICE experiment. One usually distinguishes two different cases: soft collisions, in which the electrons of the target material are only excited, and hard collisions in which ionization occurs. If the electrons from ionization themselves cause substantial secondary ionization and form a secondary track, they are sometimes referred to as δ-rays.

2. A deflection of the particle due to elastic scattering from nuclei. The amount of energy transferred in these collisions is negligible compared to (1), because the masses of the nuclei of the traversed material are large in comparison to the incident particle.

Other possible reactions like Cherenkov radiation, nuclear reactions, bremsstrahlung or transition radiation are extremely rare in comparison to these [25].

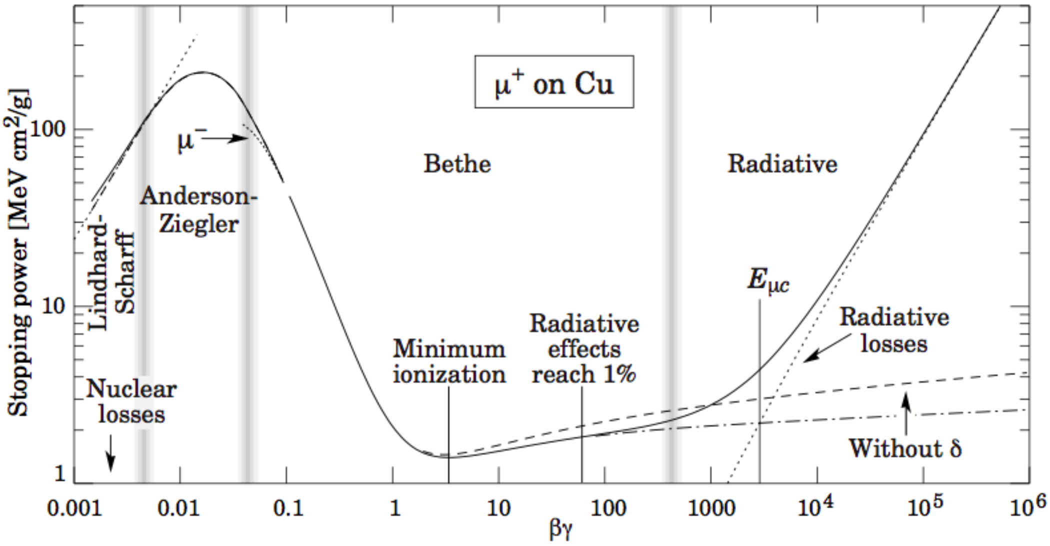

Figure 2.3: Mean energy loss per unit path length $< dE/dx >$ (or stopping power) for muons on copper as a function of $\beta\gamma$. From [1].

2.3 The Bethe-Bloch formula

The first calculation for the energy loss of charged particles in material was performed by Bethe [26]:

$$\langle \frac{dE}{dx} \rangle = \frac{4\pi N e^4}{mc^2} \frac{z^2}{\beta^2} \left(\ln \frac{2mc^2\beta^2\gamma^2}{I^2} - \beta^2 - \frac{\delta(\beta)}{2} \right), \tag{2.4}$$

where mc^2 is the rest energy of the electron, z the charge of the projectile, N the number density of electrons in the matter traversed, e the elementary charge, β the velocity of the projectile and I the mean excitation energy of the atom. For a given momentum, the mean energy loss of a particle depends only on the charge and mass of the particle.

As $\beta\gamma$ increases the curve falls at first proportional to $1/\beta^2$, then goes through a minimum (the minimum ionizing region close to $\beta\gamma \approx 3.6$) and grows again for larger values of $\beta\gamma$ due to the logarithmic term (relativistic rise). The origin of this effect has two components. On one hand, the maximal transferable energy in each collision is rising and on the other, the cross section for excitation and ionization rises due to the relativistic contraction of the electromagnetic field in longitudinal direction (see figure 2.3).

$\delta(\beta)$ is a correction term which accounts for the so-called density effect, which was first introduced by Fermi: for large values of $\beta\gamma$ the surrounding polarizable atoms shield the field of the propagating particle. The exact behavior of $\delta(\beta)$ is material dependent.

However, the track ionization for drift chambers cannot be calculated with the help of (2.4), because - above a certain maximal transferred energy E^{max}_{trans} - δ-electrons reach far enough to lead to an ionization which does not contribute to the original track [23]. The modified Bethe-Bloch formula for the restricted energy loss is given by:

$$\langle\frac{dE}{dx}\rangle = \frac{4\pi N e^4}{mc^2}\frac{z^2}{\beta^2}\left(\frac{1}{2}\ln\frac{2mc^2 E_{max}\beta^2\gamma^2}{I^2} - \frac{\beta^2}{2} - \frac{\delta(\beta)}{2}\right) . \tag{2.5}$$

This equation holds true as well for electrons, because the different kinematic limits have been replaced by the common cut-off E_{max}. In addition to this, in the limit $\beta \longrightarrow 1$ one observes now a complete cancellation of the γ dependence. The energy loss reaches a constant value, the so-called Fermi plateau.

2.3.1 Fluctuations in energy loss

Until now, the discussion was mainly focussed on the mean energy loss and not on the statistical fluctuation around the mean. An approximation of the energy loss distribution in thin absorbers $f(\lambda)$ was first calculated by Landau [27]:

$$f(\lambda) = \frac{1}{\sqrt{2\pi}}\exp\left(-\frac{1}{2}(\lambda + \exp(-\lambda))\right) \tag{2.6}$$

where λ describes the deviation of the energy loss ΔE from the most probable value ΔE_{MP} normalized to the mean energy loss $< \Delta E >$:

$$\lambda = \frac{\Delta E - \Delta E_{MP}}{< \Delta E >} . \tag{2.7}$$

Figure (2.4) shows an example of this distribution which clearly deviates from a Gaussian. Bichsel states that there are small differences between the Landau distribution and the energy loss in TPC gas cells [28]. The shapes are similar, only the width of the Bichsel distributions is larger.

2.4 TPC reconstruction: clusterization, tracking, and particle identification

It is not feasible to base the physics analysis on raw data of the TPC and the other detectors since too many CPU-intensive processes would have to be repeated for each individual physics analysis. Therefore, the raw data is *reconstructed* and for each event the found tracks together with their PID information are stored in the *Event Summary Data* (ESD), which serves as input for the various physics analyses. This step is called reconstruction and the corresponding calculations are performed on the large Tier-0 and Tier-1 compute farms of the ALICE experiment.

2.4.1 Clusters

The first step of the reconstruction is the cluster-finding in which the raw signals on neighboring pads and time-bins originating from an individual charged particle are combined. This clusterization is

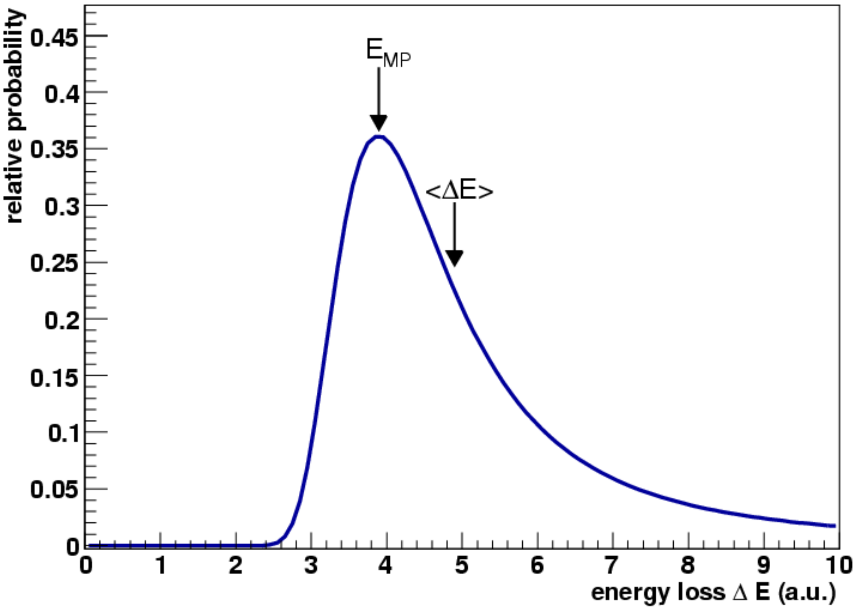

Figure 2.4: The Landau distribution. Its skewness is clearly visible as well as the long tail towards higher energy losses (E_{MP}: most probable energy loss, $< \Delta E >$: mean energy loss).

performed pad-row by pad-row. During the 2011 Pb–Pb run, the cluster finding for the ALICE TPC was carried out on-line in the High Level Trigger (HLT) system in order to reduce the data volume written to the tape storage.

Def. 1 (*TPC cluster*)

> A charged particle traversing the TPC induces a signal on a given pad-row. If the charge in a search window of 5 pads in wire direction and 5 bins in time direction exceeds a certain threshold and fulfills all necessary quality criteria, it is called a cluster. Therefore the maximum number of clusters per track n_{cl} is 159, which corresponds to the number of pad rows in a TPC sector. Curling track parts are reconstructed as separate tracks. The number of clusters assigned to a track is related to the track length in the sense that low p_t-tracks which do not reach the outer wall of the TPC have less clusters assigned. However, the relation is not straightforward, because the pad length in the TPC is increasing with radial distance to the center.

Due to the moderate gain setting of the ALICE TPC, the raw signal in a given pad-row might exceed the thresholds only in single pads and time-bins. This is in particular true for long driftlengths and for particles in the minimum ionizing region.

Def. 2 (*Single pad cluster*)

> Clusters with a low charge might have a signal only on one pad and the signal on the neighboring pads is below threshold. These clusters are not used for tracking purposes, but still contain valid information for the TPC dE/dx signal and for the track seeding. Please note, that the charge assigned to these clusters differs between the offline and the HLT cluster finder. In the case of the offline cluster finder, virtual charge is added based on the known pad response function.

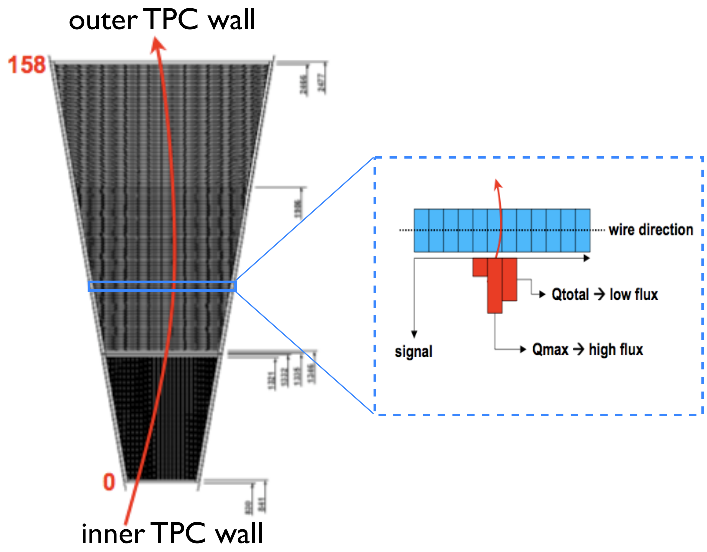

Figure 2.5: A charged particle in one TPC sector. In this case, the track crosses all 159 pad rows (63 in the inner read-out chamber and 96 in the outer read-out chamber).

Analogous to single pad clusters, single time-bin clusters would only contain information in a single time-bin. However, these clusters are already removed in the read-out electronics by the zero-suppression. In future, it might be possible to change the zero-suppression algorithm in such a way that also single time-bin clusters are stored for further offline processing.

Besides the position information $y_{i,cluster}$ in pad and $z_{i,cluster}$ in time direction, which is calculated based on the center-of-gravity, the relevant quantity for the $\mathrm{d}E/\mathrm{d}x$-calculation is the cluster charge or amplitude. In addition to this, the measured cluster width σ_{meas} is used to identify clusters from overlapping tracks (see 4.3).

Def. 3 (*Total cluster charge* Q_{tot})

The total cluster charge is given by the sum of all digits in a cluster. It corresponds to the energy deposit of a track on a given pad-row.

Def. 4 (*Maximum cluster charge* Q_{max})

The maximum cluster charge represents the maximum value among all digits in a cluster as shown in figure 2.5.

2.4.2 Tracks

In the next step, the found clusters must be connected in order to build tracks. A charged particle in the longitudinal magnetic field of the ALICE experiment follows the trajectory of a helix, which is parameterized with the 5 track parameters $(y, z, \sin(\varphi), \tan(\lambda), 1/p_t)$ in the local coordinate system as a function of x_{local} as illustrated in figure 2.6. As the kinematic properties of the particle can vary substantially along the path due to energy loss, scattering etc., a Kalman filter approach [29] is used, which allows a continuous variation of the track parameters along the trajectory.

The tracking starts on the outer pad-rows of the TPC with the seeding procedure. Several track hypotheses are formed by connecting clusters on neighboring pad-rows. Initial track parameters are

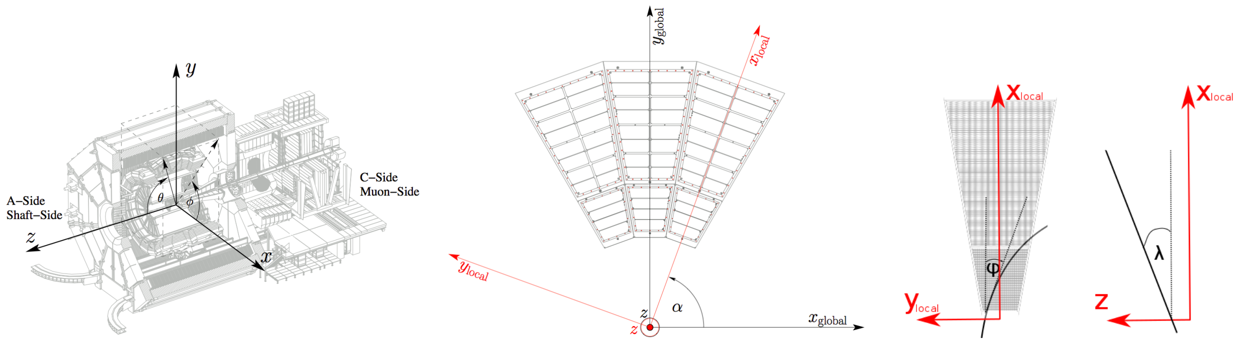

(a) (b) (c)

Figure 2.6: Global (left), local (middle) and tracking (right) coordinate system of ALICE. The left and middle plot are taken from [30].

calculated and continuously updated by adding more and more clusters during the inward propagation. For PID-related purposes, the track parameters at the inner wall of the TPC are stored. For the final physics analyses (e.g. the p_t-value which is filled into the spectrum), the track parameters are propagated to the primary vertex.

Several quantities can be used to judge the track quality in order to remove outliers and in order to select only tracks with the required p_t- and $\mathrm{d}E/\mathrm{d}x$-resolution. Some of them are introduced in the following section.

Def. 5 (χ^2/n_{cl})

The Kalman filter minimizes the track-to-cluster residuals in pad and drift direction. The χ^2 per cluster,

$$\frac{\chi^2}{n_{cl}} = \frac{1}{n_{cl}} \sum_{i=0}^{n_{cl}} \frac{(y_{i,clus} - y_{i,track})^2}{\sigma_{i,y}^2} + \frac{(z_{i,clus} - z_{i,track})^2}{\sigma_{i,z}^2} , \tag{2.8}$$

describes the quality of the fit. σ_y and σ_z correspond to the space point resolution in pad and drift direction. Please note, that σ_y and σ_z depend on the pad size, drift length, track inclination angle and the deposited charge as described in [31]. Each cluster provides two degrees of freedom.

In a Kalman filter approach the normalization of the χ^2-distribution to the number of degrees of freedom $n_{dof} = 2 \cdot n_{cl} - 5$ is only approximate as the five track parameters are permanently varied along the tracking path. As in usual track selections $2 \cdot n_{cl} \gg 5$, a typical cut of the form $\chi^2/n_{cl} < 4$ would correspond to a cut of approximately 2 per degree of freedom for ideal values of $\sigma_{i,y}$ and $\sigma_{i,z}$. As the χ^2-distribution for $n_{dof} > 100$ can be very well described by a Gaussian distribution with $\mu = n_{dof}$ and $\sigma = \sqrt{2n_{dof}}$, this corresponds to about $\frac{4n_{cl} - 2n_{cl}}{\sqrt{4n_{cl}}} \approx 9$ standard deviations for a track with 80 assigned clusters.

In many cases it is needed to compare the number of clusters attached to a track with the number of clusters which could possibly be attached to the track. In this context, it is important to distinguish between non-findable and missing clusters.

Def. 6 (*Findable clusters*)

The number of findable clusters is the number of geometrically possible clusters which can be assigned to a track. It takes into account dead zones due to chamber boundaries or the limited η-acceptance in which clusters are not findable. For the time being, clusters on dead front-end

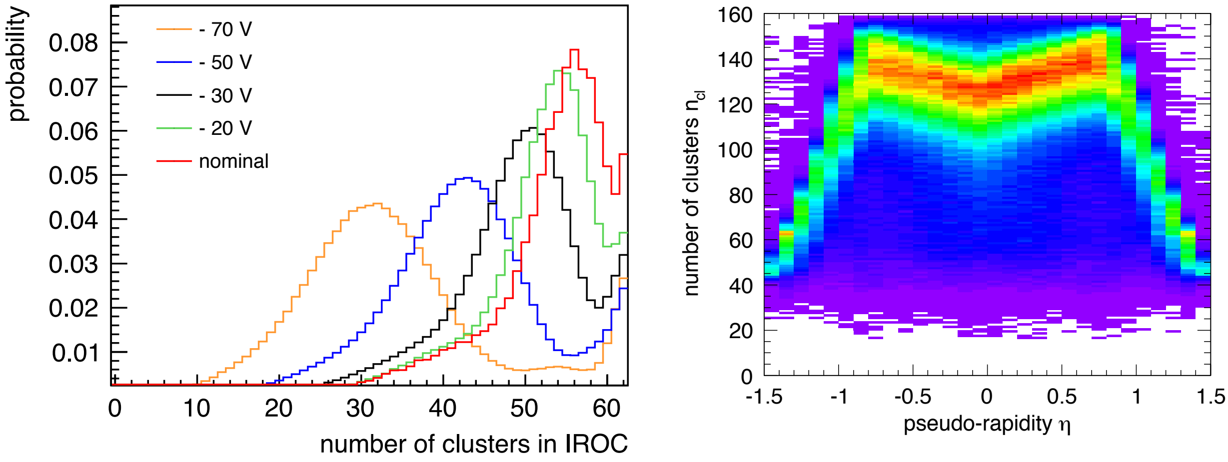

(a)

(b)

Figure 2.7: Distribution of number of clusters n_{cl} attached to tracks for IROCs as a function of the chamber voltage (left). The track sample is extracted from pp collisions and contains mainly minimum ionizing pions and a small fraction of highly ionizing protons which produce the small peak at saturation. Number of clusters as a function of η (right) showing the regions of full and limited tracking acceptance.

cards are counted as findable. In a few cases, the number of clusters on track can be larger than the number of findable clusters due to ExB effects.

Def. 7 (*Non-findable clusters*)

If a track crosses the boundary between two chambers or leaves the η-acceptance, the clusters in this area are declared as non-findable.

Depending on the high voltage setting of the read-out chambers, the collected charge on some padrows might be lower than the threshold which is required in order to reject noise. Figure 2.7 shows the number of clusters as a function of the pseudo-rapidity η illustrating the full and limited tracking acceptance of the TPC and the distribution of number of clusters attached to tracks as a function of the chamber voltage in IROCs.

Def. 8 (*Missing cluster / cluster below threshold*)

Findable clusters can be missing, because their charge is below threshold (e.g. due to baseline shifts etc.). They can be identified by looking into the neighboring pad-rows, e.g. if there is no reconstructed cluster on pad row i, but clusters are found on the pad rows $i-1$ and $i+1$ (or $i-r$ and $i+r$ in general). The number of clusters below threshold is called n_{miss}.

As a matter of fact, missing clusters mainly present a problem for the dE/dx-calibration, because they introduce non-linear threshold effects. The track quality is only slightly affected as the p_t-resolution σ_{p_t} is dominated by its dependence on the lever arm L, the magnetic field B, and the space point resolution $r\delta\varphi$ in pad direction [32]:

$$\frac{\sigma_{p_t}}{p_t} = p_t \cdot \frac{r\delta\varphi}{0.3 \cdot B \cdot L^2} \sqrt{\frac{720}{n_{cl}+4}} \,. \tag{2.9}$$

Effects of multiple scattering and energy loss in the detector material have been neglected here as they only dominate at small momenta $p_t < 1$ GeV. It is therefore convenient to introduce the number of crossed rows as quality criterion for tracks, in particular in runs where the TPC cannot be operated at the nominal chamber voltages.

Def. 9 (*Number of crossed rows n_{eff}*)

> The relevant quantity for the p_t-resolution of a track is the effectively sampled track length of a particle in the TPC, because the resolution scales roughly $\propto \frac{1}{\sqrt{n_{cl}}}$ (statistics) and $\propto n_{eff}^2$ (lever arm) where $n_{eff} = n_{cl} + n_{miss}$.

For technical reasons and for completeness, two more track related quantities need to be introduced, which are mainly related to the kink topology and to overlapping clusters.

Def. 10 (*Number of clusters after first iteration*)

> If a track is recognized as a kink candidate, it is split into a mother and a daughter track. However, the number of assigned clusters n_{cl} is the sum of the clusters assigned to the mother and the daughter. The number of clusters assigned to the mother track are still available via the number of clusters assigned during the first (inward) tracking iteration.

Def. 11 (*Number of clusters in the tracking road*)

> Not all clusters in the search road of the Kalman filter are used for the update of the track parameters, because they do not fulfill certain quality criteria. This is in particular important for overlapping clusters in the high flux environment, which are typically rejected because of a too large RMS in pad direction.

2.5 Particle identification via specific energy loss

The dE/dx-information for a given track must be extracted from the n_{cl} clusters (with $n_{cl} = 20, \ldots, 159$) which are assigned to this track. However, not all clusters which can be used for tracking are also used for particle identification.

Def. 12 (*Number of clusters used for PID n_{pid}*)

> Clusters which are located very close to the chamber boundaries or from overlapping tracks are not used for the calculation of the TPC dE/dx signal. Therefore the number of clusters used for the calculation of the dE/dx signal can be different from the number of clusters of a track. This quantity is the relevant one for the dE/dx-resolution.

Clusters close to the chamber boundaries are rejected, because the gain is lower due to edge effects and a calibration of this effect is difficult as the average size of the Krypton clusters (see section 2.6.2) is larger than the pad size. Since the position information is significantly less affected, these clusters can still be used for tracking.

For low multiplicity environments like pp data, the total charge Q_{tot} of each cluster is used as it is found to provide the best separation power. In Pb–Pb events, the dE/dx-calculation is based on the maximum charge Q_{max}. It provides slightly less separation power for peripheral events, but better separation power in central events as it is more robust with respect to cluster overlaps. Before the cluster charges can serve as an input for particle identification, they need to be equalized with the help of several calibration parameters (see section 2.6). Thus dependencies on the local track topology and on the read-out pad (gain map) are removed. In addition to this, the sample of cluster charges is complemented by the $n_{miss} \ll n_{pid}$ missing clusters which were not detected, because of their charge being below the threshold. The charge assigned to these clusters is chosen to be equal to the smallest charge in the sample.

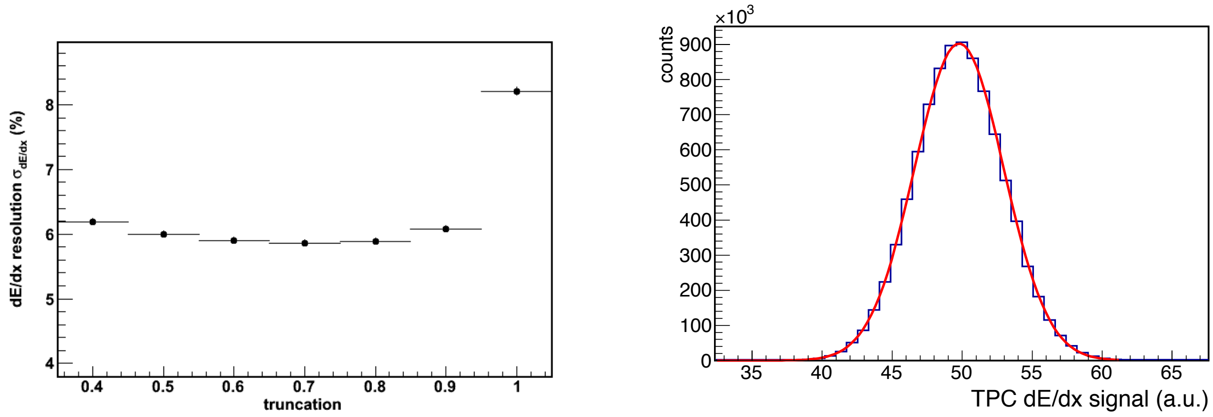

(a)

(b)

Figure 2.8: Dependence of dE/dx-resolution on the truncation α extracted from cosmic tracks (left). Agreement between TPC dE/dx signal from minimum ionizing pions and a Gaussian fit to the data (right). The track sample also contains a small contamination of muons of the order of 2-3% which has to be taken into account for detailed investigations of the tail structure on the per mille level.

The long tail towards higher energy losses in the distribution leads to the problem, that the average energy loss is not a good estimator for the mean energy loss as it would be for a Gaussian distribution. Please note, that the central limit theorem is only of limited applicability in this case as the variance of the Landau distribution is undetermined, because the corresponding integral $\int_0^\infty (x-\mu)^2 f(x)\,\mathrm{d}x$ does not converge. Therefore, the calculation of the so-called truncated mean S^α is the method of choice. It is characterized by a cut-off parameter α between 0 and 1. The truncated mean S^α is then defined as the average over the $m = \alpha n$ lowest values among the $n = n_{pid} + n_{miss}$ samples,

$$S^\alpha = \frac{1}{m} \sum_{i=0}^{m} Q_i\,, \tag{2.10}$$

where $i = 0, \ldots, n_{pid} + n_{miss}$ and $Q_{i-1} \leq Q_i$ for all i. The truncation value is optimized in a dedicated study which investigates the separation power as function of the truncation α. Figure 2.8(a) shows a similar plot illustrating the shallow minimum of the dE/dx-resolution as a function of the truncation α. The separation power shows a very similar behavior except for an even weaker dependence on α and a maximum separation closer to $\alpha = 0.6$ which is therefore chosen for the ALICE TPC. Please note that - despite the weak dependence between $0.5 < \alpha < 0.8$ - the usage of a simple arithmetic mean ($\alpha = 1$) would result in significantly worse performance. $S^{\alpha=0.6}$ is the quantity used for PID purposes and called TPC dE/dx signal. Experimentally one finds that S^α can be very well described by a Gaussian distribution as can be seen in figure 2.8(b). In regions of clear separation, a comparison of the fit integral with the number of bin counts shows typically a difference of less than 0.5% and improves with increasing number of clusters. The dE/dx or energy loss resolution $\sigma_{dE/dx}$ is given by the variance of the Gaussian distribution of S^α.

Please note that the TPC $\mathrm{d}E/\mathrm{d}x$ signal S is often abbreviated as $(\mathrm{d}E/\mathrm{d}x)_{meas.}$ or $(\mathrm{d}E/\mathrm{d}x)_{exp.}$ for the actually measured and the theoretically expected signal, respectively. This notation - which is also used in the third chapter of this thesis - has the clear advantage that it is more understandable. However, it is important to be aware of the fact that the TPC $\mathrm{d}E/\mathrm{d}x$ signal in a strict sense corresponds to a truncated mean of several energy deposit measurements and not to the average or the most probable value of the total energy lost by the particle.

2.5.1 Separation power and dE/dx-resolution $\sigma_{\mathrm{dE/dx}}$

The decisive quantity for particle identification is the so-called separation power. It quantifies the performance of a PID technique by expressing the mean difference between two particle species in multiples of the corresponding standard deviations.

Def. 13 (*Separation power D*)

The separation power D for two particle species i and j at a given momentum p is defined as

$$D = \frac{|S_i(p) - S_j(p)|}{\frac{1}{2}\left(\sigma_{dE/dx,i}(p) + \sigma_{dE/dx,j}(p)\right)} \, , \tag{2.11}$$

where $S_i(p)$ represents the TPC $\mathrm{d}E/\mathrm{d}x$ signal of particle i at the momentum p.

Since the best particle identification performance is required on the relativistic rise, a natural choice for a quantitative estimate of the achieved performance is given by the separation power between minimum ionizing particles and particles on the Fermi plateau:

$$D_{FP \to MIP} = \frac{|S(FP) - S(MIP)|}{\frac{1}{2}\left(\sigma_{dE/dx}(MIP) + \sigma_{dE/dx}(FP)\right)} \, . \tag{2.12}$$

Optimizations of the performance can be either achieved by increasing the distance $|S(FP) - S(MIP)|$ between minimum ionizing particles and the Fermi plateau (threshold effects) or by minimizing the resolution. Assuming a perfect gain calibration $\sigma_{dE/dx}$ depends on the number of samples n_{pid}, the pad size x and the gas pressure P. In a given gas cell, the energy loss distribution depends only on the number of primary interactions in the gap. This implies that the ionization distribution varies with P in the same way as it does with x and therefore the width of the distribution scales anti-proportional to the product xP. As a matter of fact, running a TPC at an overpressure of $P = 9$ bar is roughly equivalent with a nine times larger field cage.

For the remaining dependence on n_{pid} we expect a statistical scaling according to the law $\sigma_{dE/dx} \propto 1/\sqrt{n_{pid}}$. But since the ionization gathered in one cell is not statistically well behaving in the sense that mean and variance are subject to large fluctuations due to the tail in the energy loss distribution, it turns out empirically that the behavior is rather following $n_{pid}^{-0.47}$ or $n_{pid}^{-0.43}$ [23]. The precise value of the exponent seems to depend as well on the gas mixture. For Ne-based gas mixtures Lehrhaus determined a value which is again very close to -0.5 [33]. This is in good agreement with the observed dependence in the ALICE TPC as shown in figure 2.21.

However, even in the case of an infinite number of measurements, the resolution would still be affected by systematic effects. In good approximation, we can therefore assume a dependence of the form

$$\sigma^2_{dE/dx} = \sigma^2_{syst} + \sigma^2_{stat} \, , \tag{2.13}$$

which can be simply parameterized as

$$\sigma_{dE/dx} = \sqrt{c_1 + \frac{c_2}{n_{pid}}} \, . \tag{2.14}$$

The parameters c_1 and c_2 can be determined based on a fit to data: the dE/dx signal for minimum ionizing pions (which is well separated from all other species) is plotted versus n_{pid} and fitted with a Gaussian distribution. The extracted values for $\sigma_{dE/dx}$ are then fitted with the parameterization.

Besides the dominating dependence on n_{pid}, the dE/dx-resolution $\sigma_{dE/dx}$ exhibits further dependencies on several other variables.

- It significantly improves with increasing primary ionization and is therefore anti-proportional to the TPC dE/dx signal itself. The empirically expected scaling of $\sigma_{dE/dx}/S \propto 1/S^{0.25}$ is in addition convoluted with threshold effects. In practice, one finds that the resolution for a highly ionizing proton at $p_t = 400$ MeV is about 15-20% better than for minimum ionizing particles.

- An improvement of similar magnitude can be found when comparing tracks with small inclination angle and long drift length ($\eta \approx 0$) to tracks with large inclination angle and shorter driftlength ($\eta \approx 0.8$). For inclined tracks, the track length sampled per pad row is larger and they are less affected by diffusion, attachment and baseline fluctuations.

- As discussed in detail in section 2.6.5, the dE/dx-resolution also depends on the event multiplicity.

2.6 Calibration of the dE/dx signal

A prerequisite for the particle identification is the precise calibration of the cluster charges and the TPC dE/dx signal. In addition to this, the response function needs to be determined as most particle identification strategies are based on a comparison of a measured with an expected signal. In a large volume TPC, most of the calibration parameters show a strong time-dependence following changes in temperature, pressure, and gas mixture. Another typical feature in the calibration is the interdependency between calibration parameters. For example, a change in the high voltage of the read-out chambers requires not only a re-calibration of the chamber gain, but also of the dependence of the dE/dx signal on driftlength, track topology etc.

2.6.1 Calibration sources

In order to obtain the relevant calibration parameters, four different input sources were used in the calibration of the ALICE TPC: cosmic, laser, krypton, and beam (pp and Pb–Pb) events. Krypton events are only used for the extraction of the gain map. Laser events are taken at the beginning of each run and then every hour during the run. They are used for the online calibration of the drift velocity and for alignment purposes. Cosmic ray events were playing a special role for the commissioning of the detector when beam events were not yet available. They were used for the initial calibration of dE/dx and they provide a unique tool for the measurement of the p_t-resolution at large transverse momenta.

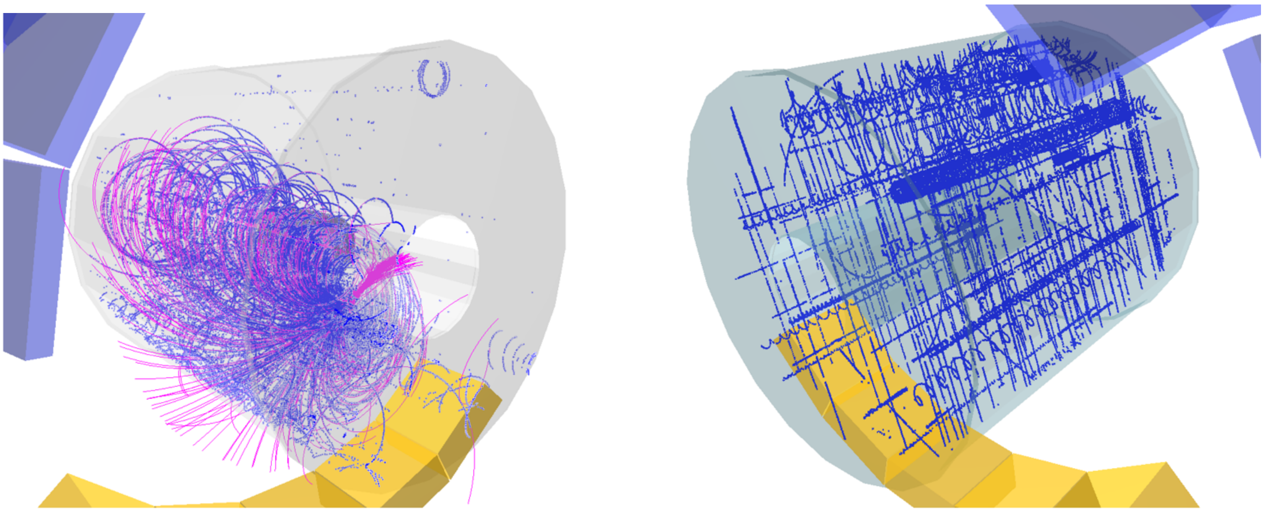

(a) (b)

Figure 2.9: Electromagnetic shower originating from an electron of a cosmic muon decay (left). A muon bundle (right).

Cosmic ray events

The primary particles which hit our atmosphere are of extraterrestrial or even extragalactical origin and consist mainly of high energetic protons. In the upper atmosphere ($\approx$ 15 km above sea level) these particles interact with air molecules and form hadronic showers. Most of the produced secondaries are pions followed by kaons. Neutral pions decay into photons, $\pi^0 \rightarrow \gamma + \gamma$, which initiate electromagnetic showers. This component is easily absorbed and therefore called soft component. The charged pions and kaons produce the hard muon component via their leptonic decay [34]:

$$\pi^+ \rightarrow \mu^+ + \nu_\mu \quad , \quad \pi^- \rightarrow \mu^- + \bar{\nu}_\mu \, , \tag{2.15}$$

$$K^+ \rightarrow \mu^+ + \nu_\mu \quad , \quad K^- \rightarrow \mu^- + \bar{\nu}_\mu \, . \tag{2.16}$$

Muons also contribute to the soft component, $\mu^- \rightarrow e^- + \bar{\nu}_e + \nu_\mu$, but 80% of the charged particles reaching sea level are muons. Their mean energy is approximately 4 GeV. The spectrum is almost flat below 1 GeV and steepens gradually to reflect the primary spectrum ($\propto E^{-2.7}$) in the 10-100 GeV range [1].

Most of the cosmics which can be observed in the ALICE experiment are single track events as they are used for the determination of the p_t-resolution. In rare cases, high multiplicity events occur. We can distinguish between two event classes as shown in figure 2.9. Firstly, electrons from muon decays which create an electromagnetic shower of many soft tracks and secondly, so-called muon bundles which consist of several parallel very high momentum muons.

Tracks from cosmic ray events can also be used for dE/dx-calibration. In this respect, electromagnetic shower events and subsequent interactions are particularly interesting as they enrich the particle spectrum and create protons and deuterons via spallation reactions. Figure 2.10 shows the dE/dx-spectrum from 8.3 million cosmic events triggered with the ACORDE (Alice COsmic Ray DEtector) setup which is an array of plastic scintillator counters placed on the three upper faces of the magnet.

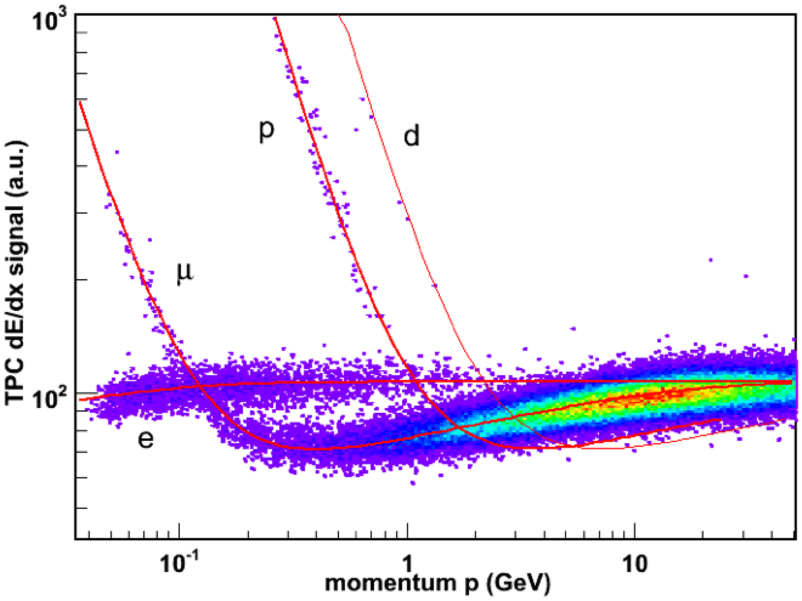

Figure 2.10: dE/dx-spectrum of cosmic ray events.

The advantage of tracks from cosmic rays is that their z-position is not correlated with their dip angle as for tracks from the primary vertex in beam data. They thus provide valuable information for corrections related to the track topology.

2.6.2 Determination of time-independent calibration parameters

In terms of calibration purposes, it is important to distinguish between time-dependent and time-independent calibration parameters. The time-independent calibration parameters are those which remain constant for a given detector configuration, i.e. for a given chamber voltage, fill gas, and capacity. These parameters have to be updated in the calibration database at maximum on a run-by-run basis. In contrast to this, time-dependent calibration parameters show a strong dependence on the gas pressure and gas mixture and have to be updated several times per run on a 5-15 min basis. In the following section, the major time-independent calibrations are introduced.

The gain map

The extraction of the dE/dx signal requires an absolute gain calibration of the 557 568 read-out pads. This is obtained by releasing radioactive ^{83}Kr into the TPC gas. This method was originally developed by the ALEPH [35, 36] and DELPHI [37] collaborations and also successfully applied by the NA49 [38] and STAR collaboration [39]. A Rubidium foil is activated at the ISOLDE Isotope Separator at CERN and mounted in a bypass line of the TPC gas recirculation system. ^{83}Rb decays by electron capture into a meta-stable state ^{83m}Kr which is relevant for the calibration and has a life time of $t_{hl} = 2.64$ h - by far long enough for the noble gas isotopes to reach the drift volume of the TPC. The homogenous occupancy of krypton clusters which is observed in the TPC thus also shows that the gas flow inside the detector works according to specifications. The ^{83m}Kr state decays entirely via photon emission (31.2 keV) to a 9.4 keV level which then decays immediately to the ^{83}Kr ground state again via photon emission. In both cases, almost no low energy photons are produced, because of internal conversion processes which happen with ratios of electron-to-photon emission of $e^-/\gamma \approx 2 \cdot 10^3$ (41.6 keV) and $e^-/\gamma \approx 20$ (9.4 keV). The internal conversion of the 9.4 keV photon can only occur in the loosely bound outer shells where practically the total energy is transferred to the conversion electron. However, the conversion of the 41.6 keV photon occurs in 23% of the cases in one of the sub-levels of the K-shell resulting in a complex decay spectrum. For details see [39].

For each channel the decay spectrum is acquired. Figure 2.11 (left) shows the obtained Krypton-spectrum on OROCs after applying the pad-by-pad equalization of the gain map (right). Calibration constants are obtained by fitting the main (E_{Kr} = 41.6 keV) peak of the spectrum with a Gaussian function. Please note, that gain variations due to pressure changes were not corrected in this spectrum. The resulting 0.2% error on the mean value is well below the required 1.5% on the single pad level [22, 31]. In total, the variations of the gas gain *within one chamber* due to mechanical imperfections and the chamber geometry (wire sag, deformations) can reach up to about 20% (minimum-to-maximum). The variation of the mean gain *chamber-by-chamber* is of similar magnitude (about 30% for IROCs and 15% for OROCs). In order to provide a φ-homogenous performance of the detector the chamber high voltages were adjusted accordingly to reach an equalized gain chamber-by-chamber within 2%.

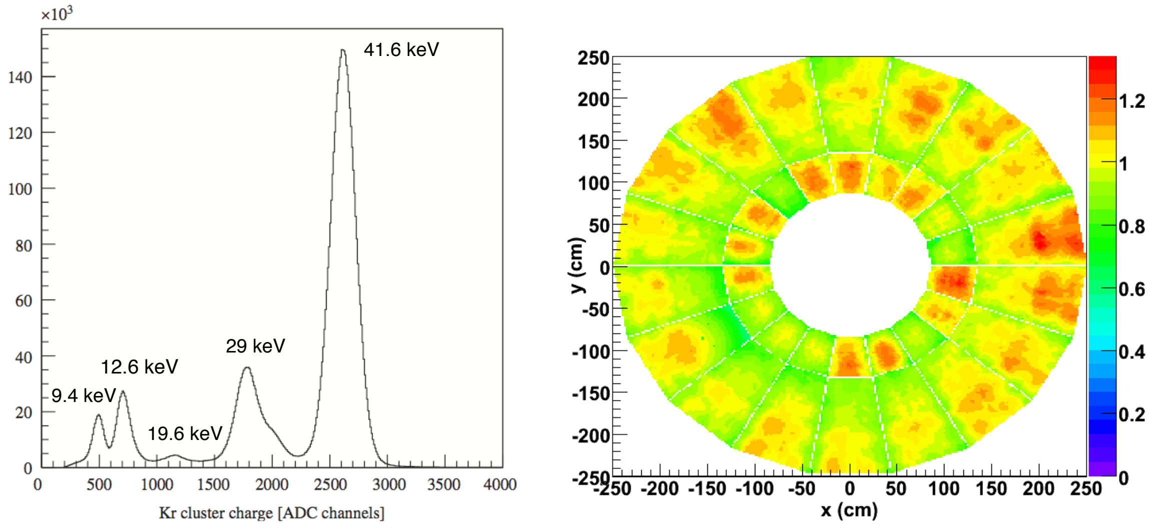

(a)

(b)

Figure 2.11: Krypton spectrum of all OROCs after pad-by-pad gain equalization (left). Resulting gain map of the C side after post-processing (right).

Due to the high granularity of the ALICE TPC, a Krypton cluster typically extends over several readout pads and the charge is associated with the pad with the maximum amplitude within the cluster. In the future, one might consider to do an additional unfolding of the charge. The resulting gain map is then further post-processed to remove a small fraction of outliers from failed fits, floating wires, noisy channels, and dead front-end cards. This is done based on a parabolic fit to the gain distribution of each individual chamber. If the deviation of a pad to this fit is too large, it is replaced with the value from the parabolic fit. The same procedure is applied at the chamber edges where a part of the energy deposit is lost in the dead-zone and the gain of the pads cannot be precisely determined. For the calculation of the dE/dx signal, these pads are removed.

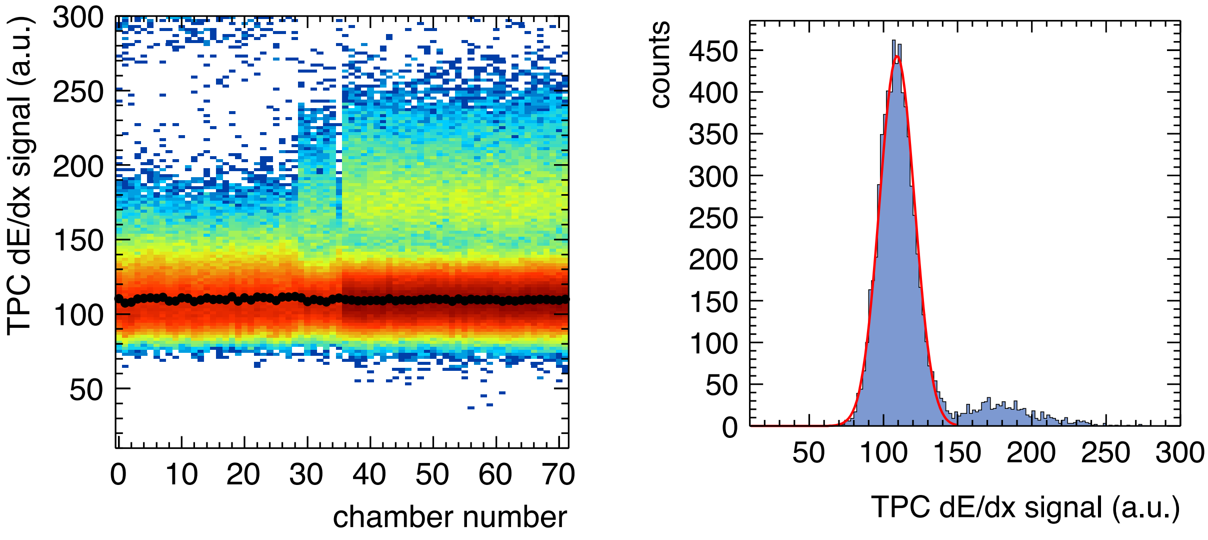

(a) (b)

Figure 2.12: dE/dx distribution for tracks within 450 MeV $< p <$ 500 MeV (minimum ionizing pions) for each individual chamber (left). A single slice from the plot on the left is shown on the right which corresponds to a single OROC (chamber 44). The peaks for minimum ionizing pions and electrons on the Fermi plateau are clearly visible together with the Gaussian fit to determine the peak position. The fitted peak position for each chamber is shown as a black circle on the left.

One of the main advantages is the large dynamic range of the TPC electronics which allows to run the Krypton calibration at the same chamber voltage (gain) as the data taking of the beam events. The Krypton clusters produce a similar signal as ordinary charged particles traversing the TPC fill gas. Typical sizes of Kr-clusters are of the order of $d \approx$ 2-3 cm. Therefore, the induced charge signal corresponds to an energy deposit per unit path length of

$$\frac{\Delta E}{\Delta x}|_{Kr} \approx \frac{E_{Kr}}{d} \approx 13.8\frac{\text{keV}}{\text{cm}} \approx 8 \cdot \frac{dE}{dx}|_{MIP} \,. \tag{2.17}$$

In addition to the pad-by-pad equalization from the Krypton calibration which is repeated once per year, the gain equalization on the chamber-by-chamber level is done more often in order to take into account changes to the hard-ware (power supplies, capacitors, resistors, voltage settings). This is done by determining the dE/dx signal of minimum ionizing pions individually for each chamber. Figure 2.12 shows an example of this calibration. This procedure has the additional advantage that it optimizes the gain map for tracks with an energy loss between minimum ionizing and the Fermi plateau[1] eliminating possible non-linearities from the extrapolation of the Krypton cluster charge which corresponds to highly ionizing particles.

Corrections depending on the track topology

Let us assume a track which deposits a charge $Q^* = 1$ per unit path length in a thin gas cell in front of a certain pad row in a given distance $l = v_D \cdot t$ (driftlength) to the read-out plane. The collected charge

---

[1] In this region, the obtained resolutions have to be optimal for the particle identification on the relativistic rise. In the $\frac{1}{\beta^2}$-region, all particles are largely separated.

on the wire grid and the induced signal on the read-out pads depends on the local track topology as well as on the pad and wire geometry. This effect is amplified, if a considerable fraction of the collected charge might be lost due to the applied threshold cuts. The known pad response function (PRF) describes the pulse height distribution on adjacent pads induced by a point-like avalanche [22, 40]. It can be approximated with a Gaussian distribution with a width of $\sigma_{PRF} = 2$ mm (IROC) and $\sigma_{PRF} = 3$ mm (OROC) respectively. The response in time direction follows in reality the shape of a function of the type $t^4 \exp(-4t)$, but for reasons of simplicity in this correction, it is also approximated with a Gaussian function of the width σ_{z0}. The response function is further smeared by transverse and longitudinal diffusion resulting in a width $\sigma_y = \sqrt{\sigma_{PRF}^2 + \frac{l}{v_D} D_T}$ in pad direction and $\sigma_z = \sqrt{\sigma_{z0}^2 + \frac{l}{v_D} D_L}$ in longitudinal direction where D_T and D_L correspond to the diffusion constants.

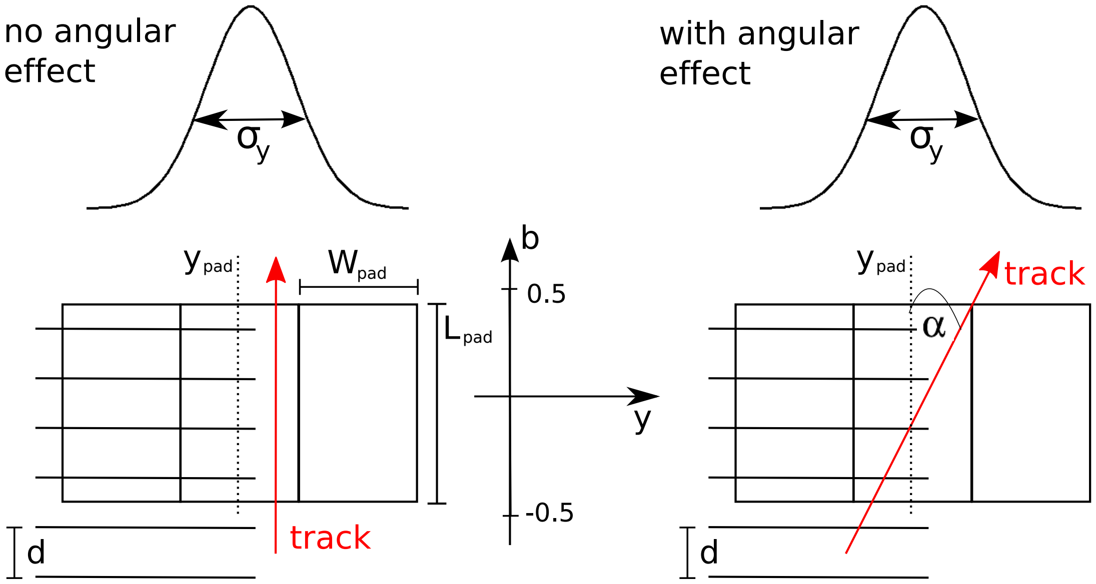

Figure 2.13: Illustration of the angular effect and the response function of the cluster charge.

Not all tracks are crossing the pad row with an angle $\alpha = 0$ as illustrated in figure 2.13. The charge distribution is thus further smeared in the pad direction over a length L_y which can be approximated by $L_y \approx (L_{pad} + 2 \cdot \epsilon \cdot \frac{d}{2}) \tan\alpha$. In a similar way, the charge distribution is smeared along the z-direction over a length $L_z \approx (L_{pad} + 2 \cdot \epsilon \cdot \frac{d}{2}) \tan\beta$ where β corresponds to the dip angle with respect to the pad plane and d to the wire pitch. The Gaussian response function is therefore convoluted with a shift with respect to the center which depends linearly on the distance b relative to the pad center. Please note that also the two neighboring wires still contribute to the signal on the pad row though with only a fraction of the charge produced in the avalanche. In principle, the full 2D pad response function (see e.g. chapter 7 in [22]) should therefore be used. As only a one dimensional response function without dependence on the pad row direction is used in this approximative correction, this effect is taken into account by a shorter charge integration range $\epsilon \cdot \frac{d}{2} \tan\alpha$ (instead of $\frac{d}{2} \tan\alpha$) with an empirically optimized parameter $\epsilon \approx 0.5$.

In order to account for the different pad types, we consider the normalized quantities $l'_y = L_y / W_{pad}$, $\sigma'_y = \sigma_y / W_{pad}$, $l'_z = L_z/(v_d \cdot \Delta t)$, and $\sigma'_z = \sigma_z/(v_d \cdot \Delta t)$ which are normalized to the pad width W_{pad} and the sampling length $v_d \cdot \Delta t$ in time direction corresponding to the sampling time Δt of the read-out electronics. The reconstructed maximum digit Q_{max} for a track crossing at the position $y' = y - y_{pad}$ and $z' = l - l_{bin}$ relative to the center of the y_{pad} and the time bin l_{bin} is then given by

$$Q_{max}(y,l,\alpha,\beta) = \frac{1}{2\pi \cdot \sigma'_y \sigma'_z} \int_{-0.5}^{0.5} \exp\Big(-\frac{(y' - l'_y b)^2}{2\sigma'^2_y} - \frac{(z' - l'_z b)^2}{2\sigma'^2_z}\Big) \mathrm{d}b \cdot L_{pad} \sqrt{1 + \tan^2\alpha + \tan^2\beta}\,, \tag{2.18}$$

where the last term corresponds to the sampled path length over the pad-row. All individual clusters are corrected with this correction factor $C_{max}(y,l,\alpha,\beta) = Q_{max}(y,l,\alpha,\beta)$ before they enter the dE/dx-calculation.

A similar correction factor can be computed for the total charge Q_{tot} in the cluster. In the determination of the correction factor for the total charge, the charge below threshold inside the cluster is also corrected. All digits in the 5 pads x 5 time bins matrix are summed up. If the digit is below the threshold, it is removed from the sum. We thus obtain

$$Q_{tot} = \sum_{pads\ i} \sum_{tbin\ j} \Theta_{thres.} \underbrace{\frac{1}{2\pi \cdot \sigma'_y \sigma'_z} \int_{-0.5}^{0.5} \exp\Big(-\frac{(y - y_{pad,i} - l'_y b)^2}{2\sigma'^2_y} - \frac{(l - l_{bin,j} - l'_z b)^2}{2\sigma'^2_z}\Big) \mathrm{d}b \cdot}_{q^*} L_{pad} \sqrt{1 + \tan^2\alpha + \tan^2\beta}\,, \tag{2.19}$$

with the dependence on the threshold q_{thres}

$$\Theta_{thres.} = \begin{cases} 0, \text{ if } q^* < q_{thres} \\ 1, \text{ if } q^* > q_{thres} \end{cases} . \tag{2.20}$$

So far, the topological correction factor can be computed by analytical means. In practice, it turns out that further 2nd order corrections have to be applied in addition. Overall, this leads to a correction of the form

$$Q' = \frac{1}{c_0 \cdot (1 + c_1 \cdot l) \cdot (1 + c_2 \cdot \tan^2\alpha) \cdot (1 + c_3 \cdot \tan^2\beta)} \cdot \frac{Q_{max/tot}}{C_{max/tot}(y,l,\alpha,\beta)} \tag{2.21}$$

The calibration parameters $c_0 \ldots c_3$ have to be determined individually for each pad region. One of the possibilities is to use very high momenta ($p > 25$ GeV) cosmic tracks whose track ionization corresponds to the Fermi plateau and with only very small curvature. As cosmics cover homogeneously all angles and driftlengths, their dE/dx signal can be binned in the relevant variables and then fitted to extract the corresponding dependence.

2.6.3 Determination of time-dependent calibration parameters

Also the time-dependent variations of the pressure, temperature, and gas composition have to be corrected. The calibration strategy is chosen such that the relevant correction values are calculated from tracks and fully reconstructed events. They are applied on the reconstruction level for each track. The calibration analysis runs on the non-calibrated data from so-called *cpass0* which is only run for a subset of the total number of events. The correction values are automatically extracted from the analysis output of this pass and then stored in the calibration database (OCDB) from where they are taken as input for the following reconstruction passes. The algorithms are structured in such a way, that the time integration interval is dynamically adapted between 5 min and at maximum 15 min in order to obtain the needed statistics to perform the Gaussian fits. The gain and PID calibration is thus completely performed offline. Alternatively, the calibration could run on online reconstructed events within the HLT system. First attempts have been made to perform an online calculation of the dE/dx signal. For the time being, only the online calculation based on Q_{max} is fast enough as the integral in equation 2.19 only has to be evaluated once. Another alternative would be given by simple parameterizations based on the gain dependence on pressure and temperature as presented in the next section. In practice, it turns out that these corrections are not precise and reliable enough over several months and would require a very detailed understanding of gas mixture changes and dependencies on the chamber high voltage. The actual implementation of the calibration algorithms in the *AliRoot* software package is shown in detail in appendix E.

Temperature and pressure dependence of gain

The pressure and temperature dependence of the gain can be best understood with the help of the Diethorn formula [41],

$$\frac{\mathrm{d}G}{G} = -\frac{\lambda \ln 2}{\Delta V \cdot 2\pi\epsilon_0} \frac{\mathrm{d}\rho}{\rho}, \tag{2.22}$$

which describes the dependence of the gain G on the gas density ρ for a given charge density per unit length λ on the wire. The parameter ΔV corresponds to the average potential difference which is needed to produce one more electron in the avalanche. Within reasonable assumptions the fill gas of the ALICE TPC can be treated as an ideal gas and thus $\rho \propto \frac{P}{T}$. Please note, that the relative change $\frac{\mathrm{d}\rho}{\rho}$ is therefore dominated by the changes in the ambient air pressure, because the temperature inside the TPC is carefully controlled and only the relative change above absolute zero is relevant (T is measured in K).

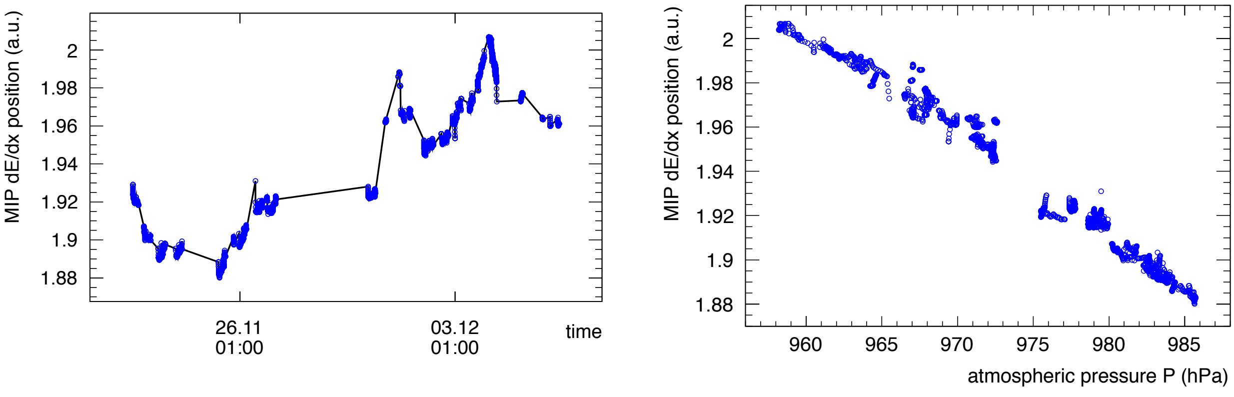

(a)

(b)

Figure 2.14: Variation of gain as a function of time (left) and its dependence on changes of the atmospheric pressure (right) for the time period during the Pb–Pb run in 2011.

The calibration task loops over the tracks, and a histogram is filled with tracks with a momentum corresponding to the velocity of minimum ionizing pions ($\beta\gamma \approx 3.6$ or $p \approx 500$ MeV). In case of cosmic events, muons on the Fermi plateau are used. After the event loop, the histogram is then fitted with a Gaussian function. The mean of the fit as a function of time is then stored in the calibration database as shown in figure 2.14. In order to obtain a smooth function, the obtained points are then converted into a spline. The normalization is arbitrarily chosen to a value of 50 ADC counts because of historical reasons (average TPC $\mathrm{d}E/\mathrm{d}x$ signal of MIPs at the gain envisaged in the TPC-TDR). The required precision of roughly 1% is given by the requirement to be much smaller than the overall $\mathrm{d}E/\mathrm{d}x$ resolution of roughly 5%.

Figure 2.14 also shows that the scaling which can be deduced from the Diethorn formula also holds approximately true for the ALICE TPC. The observed dependence of a change of gain of roughly 6% for a change in pressure of about 2.6% is in a typical range [23]. However, figure 2.14 only corresponds to a time span of about three weeks. For longer time periods, changes in the gas mixture and the chamber high voltages typically lead to a violation of the simple scaling with pressure. In practice, they become visible as different offsets of the linear behavior shown in figure 2.14 (right).

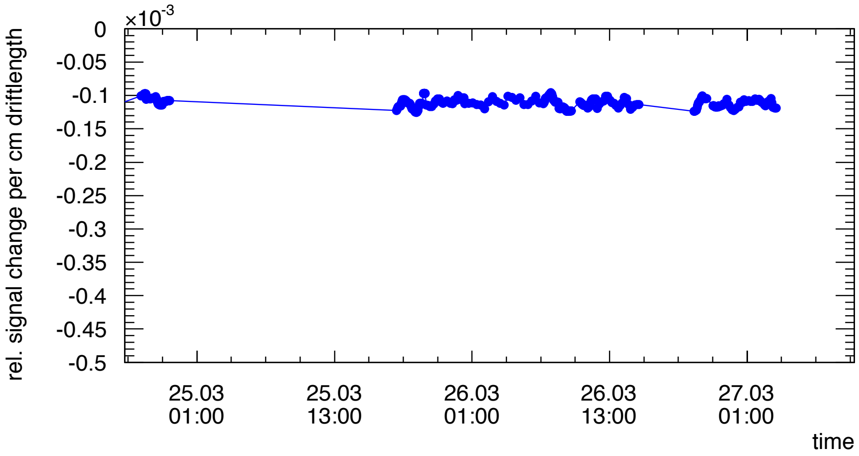

Figure 2.15: Relative signal loss per cm of driftlength as observed during the pp data taking in early 2011 (LHC11a period).

Electron attachment

The dependence of the TPC $\mathrm{d}E/\mathrm{d}x$ signal on the driftlength is strongly determined by the content of electronegative pollutants (mostly oxygen, but also water) in the gas mixture which can also show a time-dependence. This signal attenuation due to attachment during the electron drift time is a two step process requiring an oxygen and CO_2-molecule. A drifting electron is attracted by an electronegative oxygen molecule and interacts with it resulting in an excited O_2^{-*} molecule. The latter would soon decay in the back reaction, but in the presence of CO_2 a de-excitation process can occur leading to a stable O_2^-:

$$e^- + O_2 \longrightarrow O_2^{-*} + CO_2 \longrightarrow O_2^- + CO_2^* \,. \tag{2.23}$$

We therefore expect an exponential behavior of the form

$$S(l) = S_{l=0} \cdot \exp(-l/\lambda_c) \approx S_{l=0} \cdot (1 - l/\lambda_c) \,, \tag{2.24}$$

which can be approximated linearly for large values of the mean free path λ_c for capture [42] with respect to the driftlength l and correspondingly small attachment coefficients. This holds in particular true for the ALICE TPC with its very small oxygen contamination of 1-2 ppm and a signal loss of about 1% per meter of drift per ppm of oxygen [22]. The calibration of this effect is done by fitting the peak position of the dE/dx signal of minimum ionizing pions in several bins of the driftlength. In a second step, λ_c is extracted with the help of a linear fit of the mean position versus the driftlength.

Figure 2.15 shows the thus measured relative signal change per cm of driftlength during a short time period of pp data taking in early 2011. The observed loss of $1/\lambda_c \approx 10^{-4}\text{cm}^{-1}$ corresponds to a signal attenuation of about 2.5% for the full driftlength of 250 cm. Please note, that this value cannot be easily used for precise conclusions about the oxygen content in the TPC as the signal loss as a function of driftlength also depends on diffusion, threshold effects and possible baseline shifts (see following chapters). It nevertheless proves the excellent purity of the TPC fill gas in terms of contamination with electronegative pollutants during this data taking period. It is also important to notice that the effect on the dE/dx-resolution is rather small. Assuming a resolution of 5.2% in case of absence of attachment and a homogenous distribution of tracks along the driftlength, we would thus obtain a resolution of $\sqrt{(5.2\%)^2 + (2.5\%/\sqrt{12})^2} = 5.25\%$ by including the effect of signal loss along the driftlength.

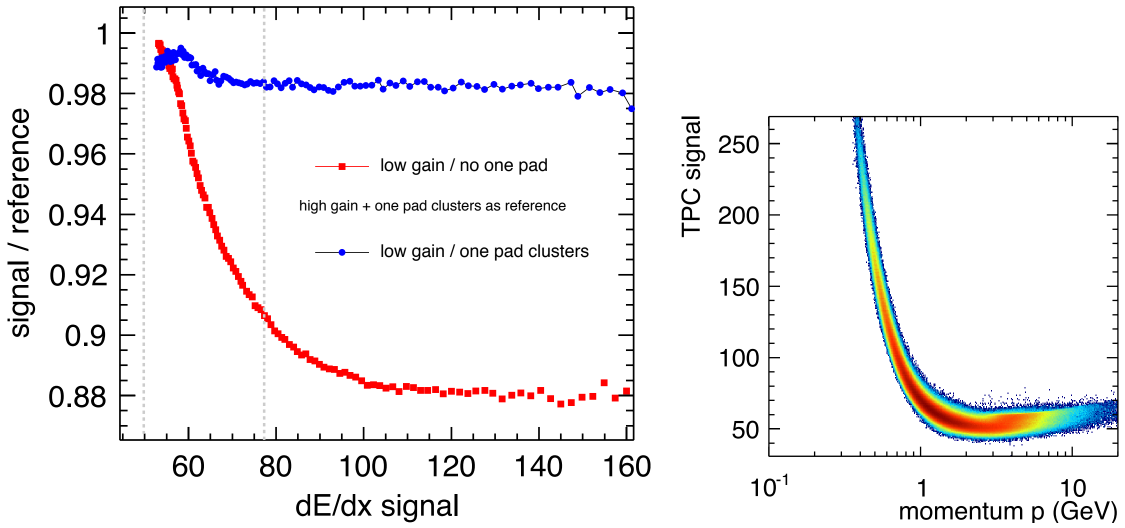

(a)

(b)

Figure 2.16: Influence of gain and ex-/inclusion of one-pad-clusters on the shape of the dE/dx signal vs. momentum curve (left) as obtained from a comparison of the dE/dx signals from a clean sample of protons after identification with the TOF system (right). The different data sets are normalized by calibration in such a way that the position of minimum ionizing particles is at a value of 50.

2.6.4 Threshold effects due to cluster loss

In section 2.6.2, a correction was discussed which reflects the loss of charge inside a reconstructed cluster for the dE/dx-calculation based on the total charge Q_{tot}. The correction becomes more complicated if the entire cluster is lost below the threshold. Besides the adding of sub-threshold clusters, the inclusion of one-pad-clusters plays an important role. An ideal probe is given by a clean sample of protons in the momentum range between 400 MeV $< p <$ 3 GeV which covers the important range of dE/dx signal values.

The effect of lost clusters below the threshold becomes best visible when comparing data from different gain settings with and without inclusion of one-pad-clusters. Figure 2.16 shows the comparison of three different data sets from the 2010 pp data taking. The high and low gain data refers to a change of the OROC high voltage from 1570 V to 1600 V. The data sample which is least influenced by cluster loss is the high gain data sample with included one-pad-clusters. It therefore serves as a reference. All data sets are normalized by calibration such that the value for minimum ionizing particles is at 50. The comparison with the low gain data without one-pad-clusters shows the expected saturation curve. While the behavior of both data sets is identical for energy deposits which are 2-3 times the minimum ionizing value, the MIP position is shifted by about 12% to higher values for the low gain data without one pad clusters. The separation power is thus clearly decreased for low gain data as clusters with low charge do not enter the truncated mean calculation.

2.6.5 Multiplicity dependent effects

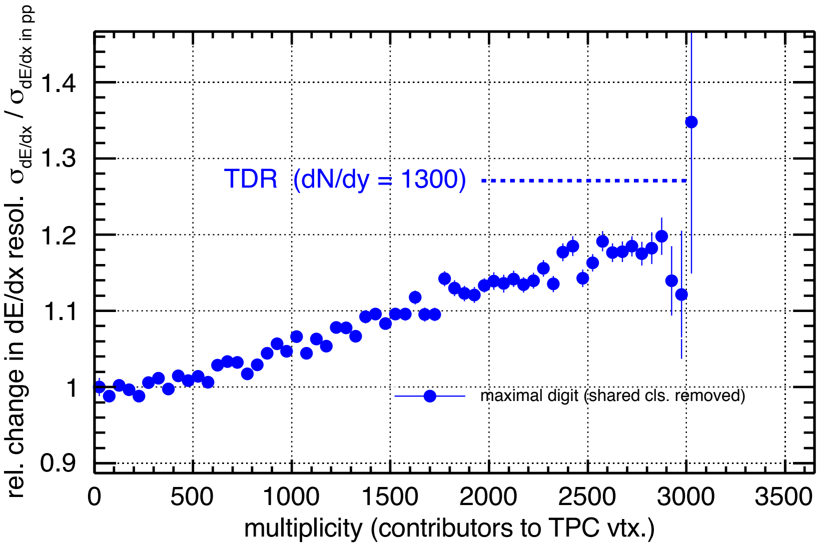

Figure 2.17: dE/dx-resolution $\sigma_{dE/dx}$ as function of the number of TPC tracks relative to the resolution in pp collisions.

In contrast to dE/dx-measurements in other TPCs, the particle identification in the ALICE experiment must also work in a high flux environment. The two most important effects in Pb–Pb compared to pp collisions are:

1. Without moving average filter, the signal is affected by an undershoot which corresponds to roughly 7.5% of the energy loss signal of minimum ionizing particles in most central collisions.
2. Overlapping clusters have to be removed from the dE/dx-calculation.

The two effects are acting in opposite direction as the signal increases due to overlaps and decreases due to charge loss in the undershoot. Overlapping clusters are removed by a simple cut on the measured cluster width σ_{meas} w.r.t. to the expected cluster width σ_{exp} as described in [31]. The cut value was chosen such that $\sigma_{meas}/\sigma_{exp} < 1.5$ and was determined in pp collisions where the small tail due to overlapping clusters is clearly visible in the distribution.

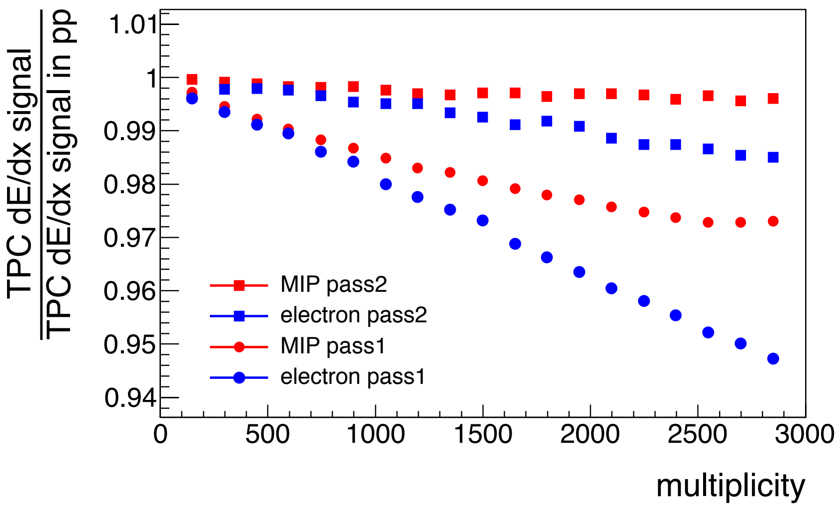

Figure 2.18: Comparison of two reconstruction passes from the Pb–Pb data taking in 2010. The figure shows the dependence of the mean dE/dx signal for minimum ionizing pions and electrons on the Fermi plateau. The pass 1 data is not calibrated for multiplicity dependent effects. In pass 2 data, the scaling is to a large extent restored by adding virtual charge for lost clusters and the shift is removed by applying a linear correction.

Baseline fluctuations - signal undershoot

The ideal response of the TPC MWPC read-out and electronics to a $\delta(t)$-signal corresponds roughly to a shape which can be described by $t^4 \exp(-4t)$ function. In the real environment, the signal is followed by a small undershoot caused by the actual response of the electronics to the ion tail. The exact shape of the signal, e.g. if it is an over- or undershoot, depends on the exact voltage setting of the chamber. In a low flux environment, the individual clusters are usually largely separated and do not influence each other. In the high-flux case, a cluster can sit in the undershoot of the previous signal with significant probability. For large drift-lengths, the effect can be so big that the collected charge of a cluster is below the threshold and the cluster is lost. This is in particular true for minimum ionizing particles. In addition to this, the fluctuations in the charge measurement are increased resulting in a worse dE/dx-resolution. Figure 2.17 shows the dE/dx-resolution as a function of the number of TPC tracks in the event. Even though a worsening of about 20% can be observed, the effect is still smaller than anticipated in the Technical Design Report.

The current version of the calibration cannot remove the worsening of the dE/dx-resolution due to fluctuations of the baseline, but the average attenuation of the signal due to the undershoot can be corrected as a function of the event multiplicity. As the value of the correction does not scale with the value of the dE/dx signal itself, the correction for the average baseline shift is *additive* and not *multiplicative* (in contrast to most of the other corrections presented in this thesis). As can be seen in figure 2.18, the baseline shift amounts to about 5% for electrons on the Fermi plateau which corresponds to about 7.5% for minimum ionizing particles and to about 1% for low-momenta protons with an energy loss of eight times the minimum ionizing value. Figure 2.18 also shows that this scaling is broken for minimum ionizing particles due to the loss of low charge clusters below the

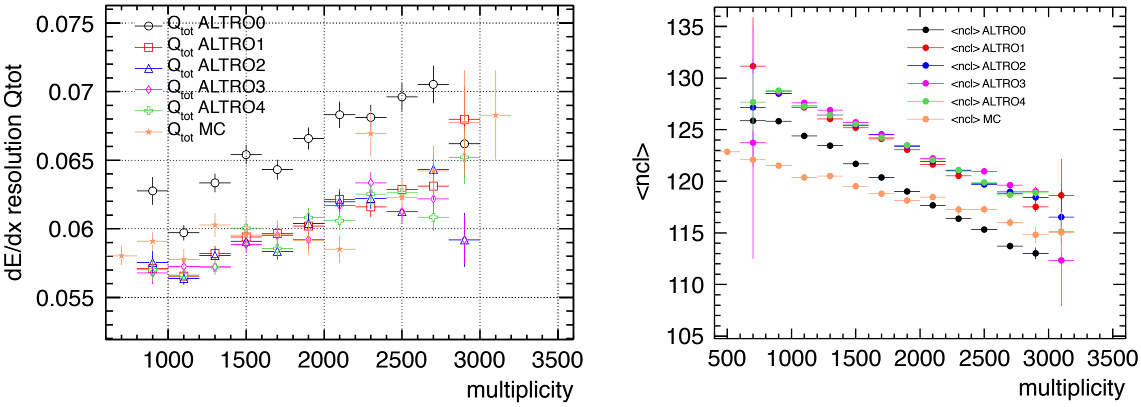

(a) (b)

Figure 2.19: dE/dx-resolution $\sigma_{dE/dx}$ as a function of multiplicity from black event analysis (left). Number of clusters on track as a function of multiplicity from black event analysis (right). The different colors represent different emulations of the read-out electronics configuration: (0.) no Moving average filter and no tail cancellation filter (TCF) / (1.-4.) MAF applied with different TCF settings.

threshold. The signal is thus shifted to higher values as outlined in the previous section. The scaling can be restored to a large extent by adding virtual charge for lost clusters as explained in section 2.5. The mean baseline shift as a function of multiplicity is then fitted with a linear parameterization on a run-by-run basis within the cpass0 and then *added* to the dE/dx signal of each track.

Moving Average Filter and Capacitor

This problem can be solved by the Moving Average Filter (MAF) in the TPC read-out electronics which dynamically adapts the baseline of the read-out electronics during the recording of a single event. Unfortunately, the MAF could not be applied during the 2010 and 2011 Pb–Pb runs because of technical problems. The effect was studied in detail with an analysis of black events which were recorded during the beginning of the 2010 Pb–Pb run. In black events, the zero-suppression is switched off so that fluctuations in the baseline can be cleanly studied. However, this results in a very large data volume which limits the statistics which can be recorded via the Data Acquisition (DAQ). The advantage of the black event analysis is given by the fact that different electronics configurations can be studied offline via the emulation of the electronics in the cluster finding on raw data. As can be seen in figure 2.19 a significant increase in the number of found clusters and an improvement in dE/dx-resolution can be observed when applying the MAF. This effect is rather independent on the settings of the Tail Cancellation Filter (TCF) which cannot be distinguished within the available statistics.

The baseline shift is increased if the capacitor is removed from the chamber and an additional resistor added since the voltage drop on the wire grid cannot be recharged fast enough. Figure 2.20 shows the mean number of clusters on tracks in the medium pad region as a function of event multiplicity for all OROCs during the 2011 Pb–Pb run. The two modified OROCs show a significantly enhanced cluster loss. The effect is stronger in C08, because it was in addition equipped with a 1 MΩ resistor whereas A04 was only equipped with a 270 kΩ resistor.

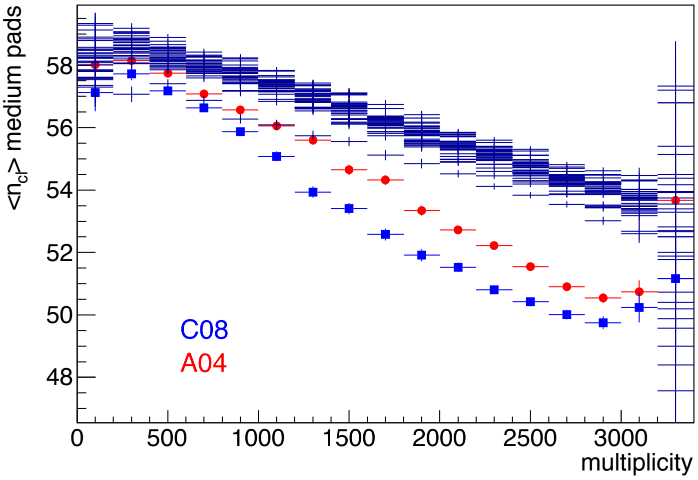

Figure 2.20: Mean number of clusters on tracks in the medium pad region as a function of event multiplicity. The OROCs without capacitor during the 2011 Pb–Pb data taking are highlighted. All other chambers are shown in dark blue.

2.7 Achieved performance and quality assurance

Figure 2.21 shows the achieved dE/dx-resolution for minimum ionizing particles as a function of the number of clusters used for particle identification. As can be seen, the resolution for long isolated tracks is about 5.2%. As already explained, the decisive quantity is given by the separation power D and not by the resolution alone. In particular, it turns out that the corrections for the threshold effects, namely the inclusion of one-pad-clusters and virtual low charge clusters, lead to a slight worsening of the resolution, but an increased separation power. Table 2.2 summarizes the achieved performance for the different reconstruction settings and shows that they are slightly better than the anticipated design value. The achieved resolution is still significantly different from the best theoretically possible resolution for the ALICE TPC layout of about 4.2% [43]. Please note that the theoretical resolution has never been reached by any existing TPC [23]. In addition to this, the number is calculated for Argon based gas mixtures and makes no statement about separation power.

system	cluster charge	corr. for thresh. effects	$\sigma_{dE/dx}$	FP/MIP	Separation Power D
pp	Q_{tot}	no	4.8%	1.44	9.2
pp	Q_{tot}	yes	5.2%	1.6	11.5
Pb–Pb (dN/d$y \approx 1601$)	Q_{max}	yes	6.5%	1.53	8.1
pp (TDR)	Q_{max}	–	5.5%	1.53	9.6
Pb–Pb (TDR dN/d$y = 1300$)	Q_{max}	–	7%	1.53	7.5

Table 2.2: Summary of the PID performance for different reconstruction settings. All numbers correspond to nominal gain and tracks which have at least 90% of all possible clusters assigned.

In order to guarantee a consistent performance for the physics analysis, the reconstruction is permanently monitored by an automatic QA procedure. In particular, the dependence of the MIP position,

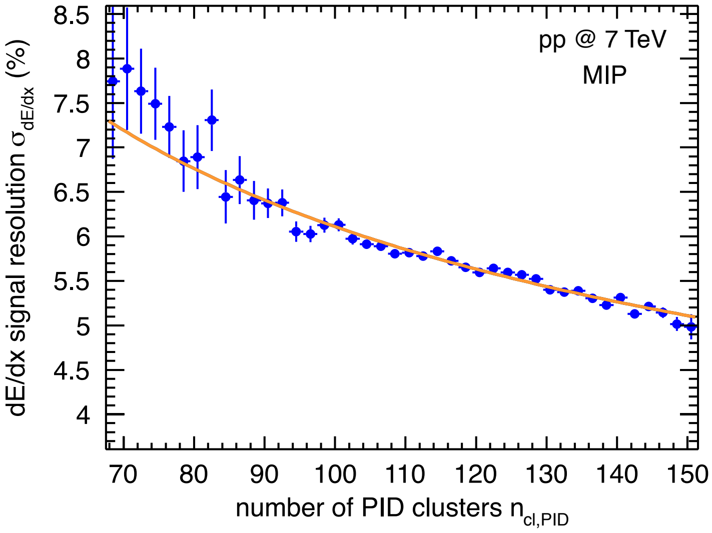

Figure 2.21: dE/dx-resolution $\sigma_{dE/dx}$ as a function of the number of clusters which are used for the calculation of the dE/dx signal. The line represents the parameterization of the resolution from equation 2.14.

the resolution, and the uniformity versus φ play an important role and the corresponding trending plots are publicly available on a web page. Figure 2.22 shows an example QA plot illustrating not only the stability of the detector, but also the functionality of the calibration algorithms.

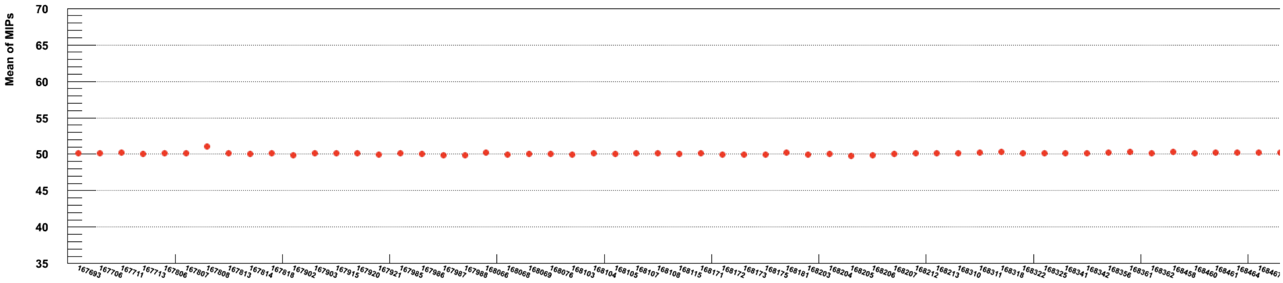

Figure 2.22: Mean dE/dx signal for minimum ionizing pions for the first runs of the 2011 Pb–Pb data taking. Automatically generated plot from the performance analysis which is also available via the web interface [44].

2.8 PID strategies

After a precise calibration of the TPC dE/dx signal, several different strategies can be pursued for the actual particle identification. Except for simple polygon cuts in the dE/dx signal vs. rigidity plane, all of them require a precise description of the expected response. Particle identification via specific energy loss has the advantage, that only a parametrization of the dE/dx signal vs. $\beta\gamma$ needs to be extracted and then the response for all particles can be determined via the simple $p/z = \beta\gamma \cdot m/z$ scaling. The parameterization of the Bethe-Bloch curve which is used in the ALICE experiment was also used in the ALEPH experiment [23] and is given by

$$f(\beta\gamma) = \frac{P_1}{\beta^{P_4}}\Big(P_2 - \beta^{P_4} - \ln(P_3 + \frac{1}{(\beta\gamma)^{P_5}})\Big)\ . \tag{2.25}$$

Details of the relation between the original Bethe-Bloch curve and this parameterization together with the explanation of the meaning of the individual parameters and a discussion of alternative parameterizations can be found in [45]. Please note in addition, that for all particle identification purposes only relative values of dE/dx need to be known and that an absolute gauging is not needed. For completeness, a scale factor can be obtained from the energy loss of minimum ionizing particles in the Ne-CO_2 gas mixture of the ALICE TPC which is about 1.73 keV/cm [42].

Besides the parameterization of the Bethe-Bloch curve, the second important part of the expected response is given by the dE/dx-resolution $\sigma_{dE/dx}$. As outlined in the sections above, it depends on many track and event variables. The two most important dependencies are those on the number of clusters (see figure 2.21) and on the event multiplicity (see figure 2.17). For each data taking period, the corresponding parameterizations are extracted and then taken into account in the offline data analysis.

Extraction of the Bethe-Bloch parameterization

The parameters of the ALEPH parameterization are also extracted for each data taking period. The procedure is based on pions, kaons, protons, and electrons in regions of clear separation after a rough identification with the TPC at lower momenta. Towards higher momenta, the sample is complemented by tracks which can still be cleanly identified with a 3σ-cut in the TOF system. The mean energy loss of the thus identified particles is extracted with a Gaussian fit and plotted vs. $\beta\gamma$. The different particle species cover the different regions of the Bethe-Bloch curve: low momenta kaons and protons the $1/\beta^2$-region, pions the minimum ionizing region with the starting relativistic rise and electrons the Fermi plateau. If needed, the coverage of the relativistic rise can be complemented by adding muons from cosmics ray events (see figure 2.10). The obtained graph is fitted with a least χ^2-minimization to obtain the parameters of the ALEPH parameterization. In practice, it turns out that small deviations of the order of 1-2% between the fit and the data can occur, in particular at very low momenta when the energy loss of the particles inside the TPC fill gas is not negligible anymore. These residuals are removed by adding a polynomial correction to the ALEPH parameterization.

2.8.1 nσ-cuts

A robust and straightforward strategy for particle identification is given by simple $n\sigma$-cuts (see also chapter 3). For each track, the difference $(\frac{dE}{dx})_{meas.} - (\frac{dE}{dx})_{fit}$ between the expected and the measured dE/dx signal is calculated and put in relation with the expected resolution $\sigma_{dE/dx}$ for the given number of assigned clusters n_{pid} on the track and the event multiplicity. If e.g. a 3σ-cut is chosen, particles can be cleanly identified over a wide momentum range without loss of efficiency. The latter being in particular important in cases when PID is used indirectly in order to increase the signal-to-background ratio in invariant mass distributions.

The advantages of the $n\sigma$-cuts are the track-by-track character and the robustness with respect to remaining miscalibration if the cut is chosen wide enough. If we consider e.g. a 3σ-cut, even a shift of the Bethe-Bloch parameterization or an underestimation of the resolution which amounts to 0.5σ results only in a systematic error of 1%. The drawback is that contamination from other particle species is directly biasing the results, in particular in the crossing regions of the Bethe-Bloch curve.

2.8.2 Gaussian unfolding

If a track-by-track particle identification is not needed, the method of choice is the Gaussian unfolding. It can only be used for direct particle identification to measure electrons, pions, kaons and protons. In a given p_t-bin, the dE/dx distribution is fitted with a superposition of several Gaussians and the corresponding yields are extracted. The method is described in detail in chapter 3 for the extraction of low momenta pion, kaon, and proton spectra. In addition to this, the method is in particular used for particle identification on the relativistic rise.

2.8.3 Bayesian PID

The Bayesian approach is based on the probability P of a particle to belong to a certain species i ($i = e, \pi, \mu, K, p$) which can be easily calculated. If $(\frac{dE}{dx})_{meas.}$ and p are the measured TPC dE/dx signal and momentum, we simply find for the probability for the species i:

$$P(i) = \frac{1}{\sqrt{2\pi}\sigma_{dE/dx}} \cdot \exp\left(-\frac{\left((\frac{dE}{dx})_{meas.} - (\frac{dE}{dx})_{fit}\right)^2}{2\sigma^2_{dE/dx}}\right) . \tag{2.26}$$

The obtained probabilities $P(i)$ can contribute to a combined Bayesian approach of PID. In this context, the $P(i)$s are referred to as *detector response probabilities*. In the Bayesian context, these probabilities are weighted with the so-called priors $C(i)$ which describe the relative concentrations of particle species. They have to be determined for each analysis individually as they are dependent on the applied cuts. Then the probability $w(i)$ of a particle to be of type i is given by:

$$w(i) = \frac{C(i) \cdot P(i)}{\sum\limits_{k=e,\pi,\mu,K,p} P(k) \cdot w(k)} . \tag{2.27}$$

This ansatz also allows combinations of the PID information from several detectors. The overall detector response probability $P_{tot}(i)$ is – under the assumption of independent measurements – the product of several single detector response probabilities:

$$P_{tot}(i) = P_{TPC}(i) \cdot P_{ITS}(i) \cdot P_{TRD}(i) \cdot \ldots \cdot P_{TOF}(i) . \tag{2.28}$$

The Bayesian PID has the drawback that the efficiency of the PID selection often cannot be easily determined and that the determined probabilities are very sensitive to eventual imperfections of the calibration.

3 Transverse momentum spectra of charged pions, kaons, and protons

The physics goal of the analysis is to measure the transverse momentum p_t spectra of primary charged pions, kaons, and protons. In order to allow for a consistent comparison to particle production models, the ALICE experiment defines primary particles as follows:

Def. 14 (*Primary particle*)

> A primary particle is a particle produced in the collision including products of strong and electromagnetic decays, but excluding feed-down from weak decays of strange particles.

Please note that decay products of particles with charm and bottom valence quarks (e.g. D^0, Λ_c, Λ_b etc.) are counted as primaries within this definition as their mother particles are not *strange* hadrons. The same holds true for particles with charm and strangeness content, e.g. the D_s, which is regarded as a particle with charm and not as a strange particle.

The analyses which are subject of this thesis only cover a certain region of the total transverse momentum spectrum as they are based on TPC particle identification. The ITS analysis extends the momentum reach to lower transverse momenta and the TOF analysis towards higher momenta. Even higher momenta are then again accessible via particle identification on the relativistic rise of the TPC $\mathrm{d}E/\mathrm{d}x$ signal. In the overlapping regions, the individual analyses are combined using the assigned systematic and statistical error as a weight (see section 3.4 for details). In the work presented in this thesis, two complementary approaches were chosen as discussed later in detail. First, a pure TPC particle identification via Gaussian unfolding of the $\mathrm{d}E/\mathrm{d}x$ signal was used in the analysis of the 900 GeV pp data, because detector calibration of all subsystems were still constantly changing directly after the start of data taking. Second, a particle identification based on nσ-cuts in the TPC $\mathrm{d}E/\mathrm{d}x$ signal at lower momenta which is then *combined* with an nσ-cut in the TOF signal towards higher momenta where the bands of the Bethe-Bloch curve start overlapping. The latter approach is often referred to as *combined TPC-TOF* analysis within the ALICE collaboration.

The continuously adapted, but largely identical analysis package was used for pp data at $\sqrt{s} = 900$ GeV and $\sqrt{s} = 7$ TeV as well as for Pb–Pb data at $\sqrt{s_{NN}} = 2.76$ TeV. The systematic errors were estimated individually for each energy and collision system, but are practically identical for pp collisions at 900 GeV and 7 TeV. The same holds true for some contributions to the systematic error in Pb-Pb data with respect to pp data. In this context, systematic effects which are significantly multiplicity dependent are explicitly mentioned in the text.

The variety of different analysis approaches and detectors involved in the extraction of ordinary transverse momentum spectra of charged pions, kaons, and protons might be confusing for the reader in the beginning. However, it only reflects the experimental challenge of particle identification which can only be done over a broad momentum range by a combination of several different techniques.

3.1 Relativistic kinematics and detector acceptance

In relativistic heavy-ion physics, the phase-space of the produced particles is commonly described using transverse momentum p_t and rapidity

$$y = \frac{1}{2} \ln \frac{E + p_z}{E - p_z} \,. \tag{3.1}$$

For the measurement of particle spectra, the triple differential yield can be expressed with the help of the variables (y, p_t, φ) in the form

$$E\frac{\mathrm{d}^3N}{\mathrm{d}p^3} = \frac{\mathrm{d}^3N}{\mathrm{d}\varphi\,\mathrm{d}y\;p_t\mathrm{d}p_t} = \frac{1}{2\pi p_t}\frac{\mathrm{d}^2N}{\mathrm{d}y\;\mathrm{d}p_t} \tag{3.2}$$

where N corresponds to the number of produced or generated (in the case of MC) particles. Experimentally, the transverse momentum is measured via the track curvature, but the rapidity is not directly accessible since it depends on the rest mass of the measured particle. In practice, the dip angle λ or the pseudo-rapidity η are determined with

$$\eta = -\ln\left(\tan\left(\frac{\lambda}{2}\right)\right) = \frac{1}{2}\ln\frac{|\vec{p}|+p_z}{|\vec{p}|-p_z}\,. \tag{3.3}$$

For the measurement of *unidentified* particles, the results are mostly presented in the form of $\frac{dN}{d\eta dp_t}$. In the case of *identified* particle spectra, the difference between η and y has to be taken into account carefully. The geometrical acceptance of the TPC for full tracking is limited to $|\eta| < 0.9$ (with a slight dependence on the z-position of the primary vertex). As a consequence, the accepted rapidity region is depending on the transverse momentum of the particle. This dependence is different for different particle masses as illustrated in figure 3.1.

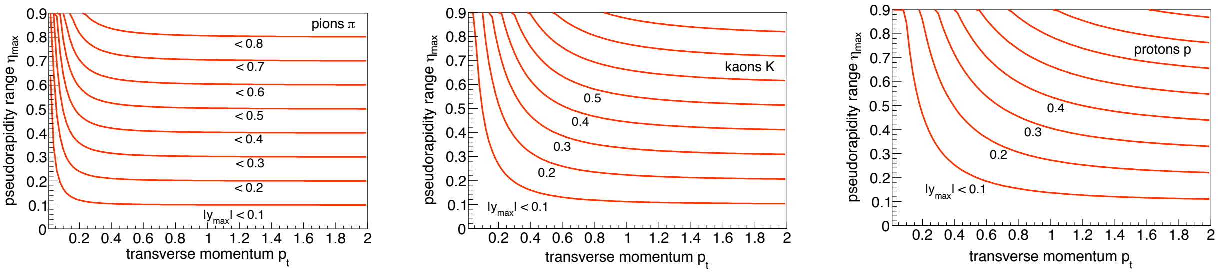

Figure 3.1: Pseudorapidity range η as a function of transverse momentum p_t for different rapidity ranges and particle masses.

For the choice of the rapidity range of the measured spectrum, there are two commonly applied approaches:

1. To limit the rapidity range in such a way that it is well contained in $|\eta| < 0.9$ for all particles. It has the drawback that the in principle available statistics is reduced.
2. To choose a rapidity range which is larger than the one covered by the detector, e.g. $|y| < 0.9$. The extrapolation to regions outside of the acceptance is usually done via the efficiency correction which is based on generated particles in $|y| < 0.9$ and on reconstructed particles in $|\eta| < 0.9$. In this case, the disadvantage is given by the fact that it relies on how well the rapidity distribution of the generator matches the real data in the extrapolated region.

While most analyses which are based on track pairs (e.g. J/ψ, Λ, etc.) choose the second option, the analysis of charged pion, kaon, and proton spectra choose a limit of $|y| < 0.5$ in order to minimize the extrapolation to the unmeasured rapidity region. It is defined by the minimum momentum of $p_t \approx 450$ MeV which is needed for primary protons to reach the TPC. In order to avoid edge effects, the efficiency correction is nevertheless done as outlined for the second approach.

An alternative choice of phase space variables is given by the transverse mass $m_t = \sqrt{m_0^2 + p_t^2}$ which can be used instead of the transverse momentum p_t. It has the advantage that effects of transverse flow and m_t-scaling become immediately visible, but also has the clear disadvantage that detector efficiencies are more difficult to interpret.

3.2 The analysis: step-by-step

In the following section, the individual steps of the analysis are presented and discussed in detail. Several steps are similar in most of the physics analyses, in particular the event and track selection.

3.2.1 Event selection

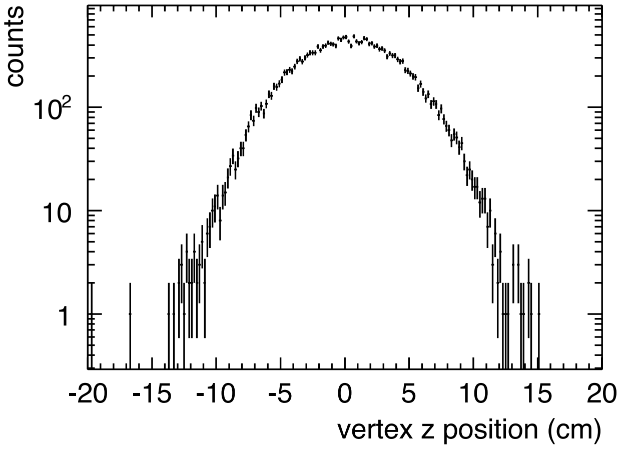

Figure 3.2: Distribution of the z-position of the primary vertex in pp collisions at 7 TeV.

The first step in the analysis is the event selection. In order to select events from pp and Pb–Pb collisions, the presence of two colliding bunches is required via the BPTX (Beam Pickup for Timing for the eXperiments) signals. The selected events are further required to contain a reconstructed primary vertex whose z-position v_z has to be within $v_z < 10$ cm. This reduces the contamination from beam-gas events and acceptance effects. The vertex reconstruction efficiency calculated via Monte-Carlo simulations is 96.5% for events with one reconstructed track. The primary vertex distribution is shown in figure 3.2 exemplarily for pp collisions at 7 TeV. For the analyses presented in this thesis, the data samples were chosen such that the fraction of pile-up events is negligible (average collision probability per bunch crossing $\mu < 0.1$). The latter is in particular important for the studies which investigate the evolution of particle ratios as a function of event multiplicity in pp collisions.

Event selection in pp collisions

In pp collisions, the results presented in this thesis are normalized and corrected to the number of inelastic pp collisions including diffractive events (see table 3.1). The minimum bias online trigger selection requires a signal in either of the VZERO counters or at least one hit in either of the SPD layers. The event selection is further improved based on an offline trigger using the timing information of the VZERO and by cutting on the correlation between the number of clusters and track segments[1] [46, 47]. The analyzed events still contain a small contribution from beam-induced background or accidentals of the order of 4% which is subtracted with the help of control triggers (bunch-empty and empty-empty). The number of selected events is then converted to the number of inelastic collisions

---

[1] Within the ALICE experiment this is often referred to as *events after AliPhysicsSelection*.

after correcting for the vertex reconstruction and trigger efficiency based on the Monte-Carlo simulation. For this, the cross-section for diffractive processes in the Monte-Carlo Generator was scaled to the measurements of UA5 [48] in the case of $\sqrt{s} = 900$ GeV data.

The subtraction of beam-gas events and the corrections for trigger and vertex reconstruction efficiency partially compensate each other resulting in an overall correction of about 5% with a systematic uncertainty of about 2% due to uncertainties in the modeling of diffraction in the event generators. For the 7 TeV data this uncertainty is of the order of 10%, because a measurement of the percentage of diffractive events is not yet available.

event class	fraction of generated events	trigger efficiency
single diffractive	22.5 %	69.89 %
double diffractive	12.2 %	90.88 %
non-diffractive	65.3 %	99.98 %

Table 3.1: Fraction of non-diffractive and diffractive events in Pythia 6.4 (tune D6T) and the trigger efficiency for this event class.

For comparisons with results from other experiments which are published for the non-single-diffractive class (NSD), the spectra can be scaled with a p_t-independent factor of $k = \frac{\mathrm{d}N_{ch}/\mathrm{d}\eta|_{NSD}}{\mathrm{d}N_{ch}/\mathrm{d}\eta|_{INEL}} \approx 1.185$ [46]. Monte-Carlo studies indicate that the spectral shape changes by less than 5% from all inelastic to non-single diffractive events. Figure 3.3 shows the difference of the spectral shape for Pythia (tune D6T) events between all inelastic collisions and the mix of event classes selected by the trigger conditions.

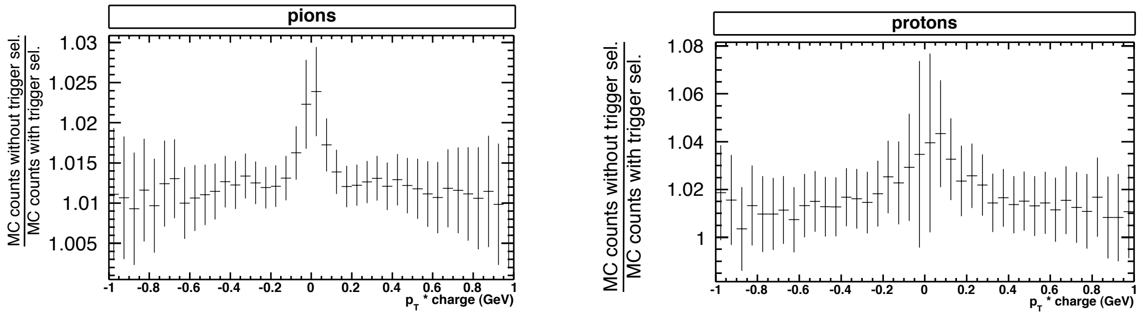

(a) (b)

Figure 3.3: Trigger bias on the spectral shape for pions (left) and protons (right) in pp collisions.

For the analysis of $\sqrt{s} = 900$ GeV data from 2009, about 300k inelastic events are analyzed whereas the analysis of $\sqrt{s} = 7$ TeV data is based on about 8 million events from 2010 data. At this level, the statistical uncertainties of the minimum bias spectrum are already negligible with respect to the systematic uncertainties. The same holds true for the Pb–Pb spectra except for the very peripheral bins. For reasons of better readability, statistical errors are therefore often not explicitly shown in the final plots, but added in quadrature to the systematic errors.

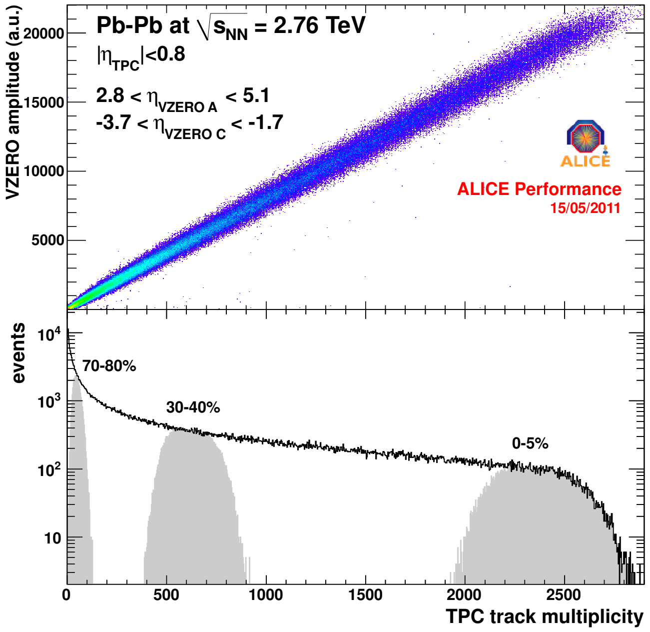

Figure 3.4: Correlation between V0 amplitude and the number of reconstructed TPC tracks. The different centrality classes are also indicated.

Event selection in Pb–Pb collisions

In contrast to pp collisions, the trigger efficiencies and the normalization to the number of events is trivial as trigger and vertex reconstruction efficiencies are equal to one for all practical purposes. For the analyses presented here, the definition of the event centrality is based on the sum of the amplitudes measured in the two VZERO detectors [12]. The percentage intervals of the hadronic cross section are obtained from a fit using a MC Glauber model assuming $\sigma^N_{INEL} = 64$ mb and a Woods-Saxon nuclear density with radius $R = 6.62 \pm 0.06$ fm and a surface diffuseness $d = 0.546 \pm 0.01$ fm. An introduction to the Glauber model is given in the appendix. Table 3.2 shows the measured $\mathrm{d}N_{ch}/\mathrm{d}\eta$ for unidentified particles for the centrality classes which are relevant for this analysis. Figure 3.4 shows the correlation between the number of reconstructed TPC tracks and the amplitude in the VZERO detectors.

3.2.2 Track selection

In an analysis based on the TPC, several track cuts have to be applied to guarantee an optimal track quality and $\mathrm{d}E/\mathrm{d}x$- and momentum resolution:

- At least 80 clusters assigned to the track in the TPC.
- $\chi^2/n_{cl} < 4$.
- The rapidity (calculated under the mass hypothesis of the measured spectrum) within $|y| < 0.5$.
- At least two clusters in the ITS and at least one of them from the SPD.
- Rejection of kink daughters.

centrality	dN_{ch}/dη
0%-5%	1601 ± 60
5%-10%	1294 ± 49
10%-20%	966 ± 37
20%-30%	649 ± 23
30%-40%	426 ± 15
40%-50%	261 ± 9
50%-60%	149 ± 6
60%-70%	76 ± 4
70%-80%	35 ± 2

Table 3.2: dN_{ch}/dη for the relevant centrality classes for this analysis. From [12].

- Track must still be present in ITS and TPC refit.

Whether a cut on the distance of closest approach (dca) to the reconstructed primary vertex is applied depends on the PID strategy (see section 3.2.3). In case of the $n\sigma$-approach, the raw yield is directly taken from a fit of MC templates to the dca_{xy} distribution. If the particle identification is done via Gaussian unfolding, primaries are selected based on a cut in dca_{xy} and dca_z taking into account the p_t-dependence of the impact parameter resolution. Thus, tracks are required to fulfill the conditions

$$dca_{xy} < 0.035\text{mm} + \frac{0.042\text{mm}}{p_t^{0.9}} \tag{3.4}$$

$$dca_z < 0.073\text{mm} + \frac{0.035\text{mm}}{p_t^{1.11}} \tag{3.5}$$

corresponding to about seven standard deviations of the resolution for primary protons. In principle, the cut could be hardened for pions and kaons where the resolution in dca_{xy} and dca_z is better, because of the smaller energy loss in the detector material. A detailed investigation shows that this is an unnecessary complication as the feed-down correction for pions is already small and for kaons it is negligible.

3.2.3 Particle identification, feed-down correction and raw spectrum

The extraction of the raw spectrum depends on the choice of the PID strategy. In the case of Gaussian unfolding, for each p_t-bin three histograms corresponding to the three mass hypotheses are filled with the normalized difference between the expected and measured dE/dx signal,

$$\frac{(dE/dx)_{meas.} - (dE/dx)_{exp.}}{(dE/dx)_{exp.}}, \tag{3.6}$$

where the expected dE/dx signal is calculated from the parameterization of the Bethe-Bloch curve. The obtained distribution is then fitted with multiple Gaussians as shown in figure 3.5. The starting values of the fit for the mean and the width are taken from the parameterization of the Bethe-Bloch curve and from the expected dE/dx-resolution. In order to allow for possible deviations due to residual miscalibration, the fit values for the mean and the width are not allowed to deviate by more

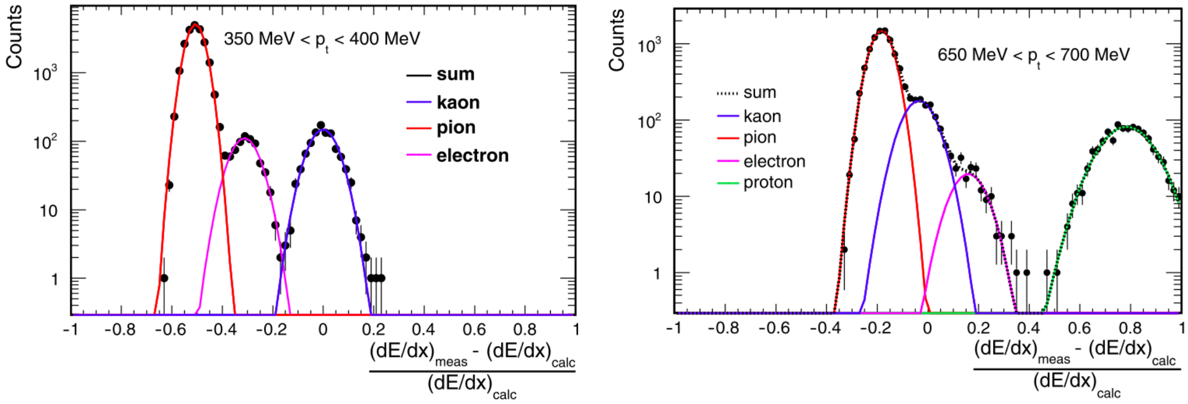

Figure 3.5: Distribution of $\frac{(dE/dx)_{meas}-(dE/dx)_{exp.,kaon}}{(dE/dx)_{exp.,kaon}}$ measured with the TPC for two p_t-bins showing the separation power in pp collisions. The dotted line represents the result of the multi-Gaussian fit to the distribution. The colored lines show the individual Gaussian functions with the parameters obtained from the multi-Gaussian fit.

than 5% and 15%, respectively. The integrals of the central Gaussians in the three histograms then give the raw yields.

The unfolding of the dE/dx signal distribution with multiple Gaussians has the drawback that the raw yield still needs to be corrected for feed-down from weak decays of strange particles in a second step. It is impossible to rely on the MC generators as most of them underestimate the production of Λs by a factor 2-3 at low transverse momenta [49]. In the 900 GeV pp analysis, the correction was done by scaling the feed-down correction obtained from plain PYTHIA with a p_t-dependent factor which is given by the ratio of the measured Λ-spectrum from real data to the generated Λ-spectrum.

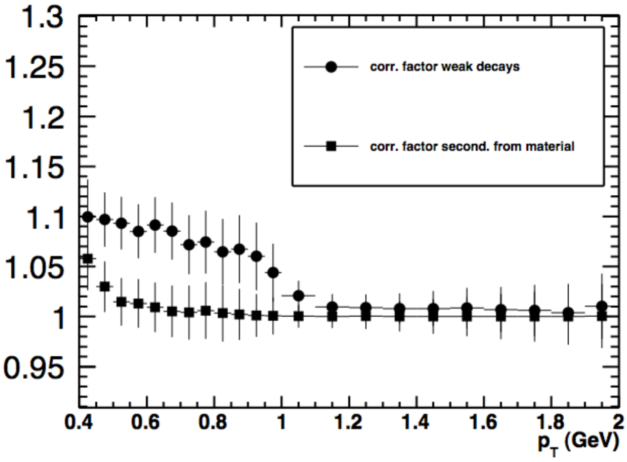

Figure 3.6: Contamination from secondary protons from weak decays (circle) and from material (box) obtained from MC pp events at $\sqrt{s} = 900$ GeV (Pythia D6T).

A similar correction has to be applied for secondary protons originating from spallation reactions with the detector material. The difference is not related to the relatively small uncertainty in the knowledge of the material budget, but to the underestimation of the cross-sections of such reactions in the GEANT3 transport code. Figure 3.6 shows the unscaled contamination from protons from weak decays and from material as a function of transverse momentum for pp collisions in MC events. As one can see, the specific decay topology of the Λ-particle (where the proton takes away most of the mother momentum and is likely to follow the mother direction) leads to a significant contamination of the spectrum. Above a certain momentum of approximately 800 MeV most of the secondaries are rejected by the requirement of at least one hit in one of the SPD layers, because the secondary vertex of the Λ-decay is Lorentz-boosted behind the SPD layers. In central Pb–Pb collisions this effect is significantly reduced as the daughter tracks can pick up fake hits from other tracks in the SPD.

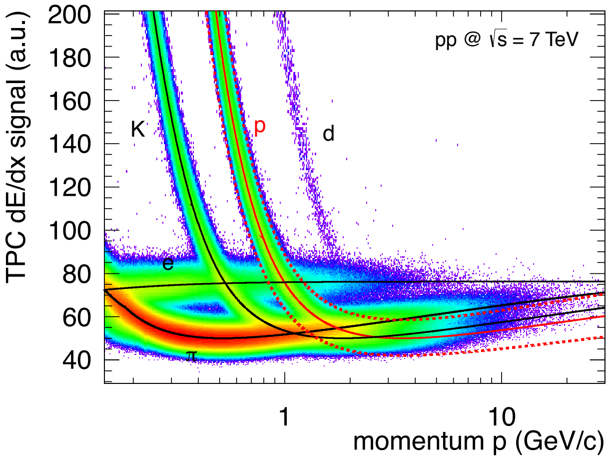

Figure 3.7: Schematic illustration of the 3σ-cut for particle identification in the TPC.

The more elegant alternative to the particle identification via Gaussian unfolding is given by the nσ-approach. After applying the track cuts with the rapidity calculated under a given mass hypothesis, the tracks are simply identified as e.g. protons if their measured dE/dx signal is within 3σ of the expected signal. The cut is schematically illustrated in figure 3.7. The natural drawback of this method compared to unfolding methods is the contamination from other particle species when the bands of the Bethe-Bloch curve start to overlap towards higher momenta. This method is therefore limited to a smaller p_t-range whereas unfolding methods can also be safely applied on the relativistic rise. It is therefore extended with a similar 3σ-cut in the TOF towards higher p_t where the separation of the different particle species in the TOF is still large. One of the main advantages of this combined approach is that the TOF information is not used towards lower momenta where uncertainties due to matching efficiencies in the track extrapolation to the TOF are large. In addition to this, the combination of the 3σ-cut in TPC and TOF reduces significantly the background due to mismatch in the TOF spectrum. Table 3.3 shows the relevant p_t-ranges for the three different particle species in this so-called *combined TPC-TOF approach*. If the contamination from other particle species is too high in the boundary bins, a 2σ-cut is used for the extraction of the raw yield.

In contrast to Gaussian unfolding, the nσ-approach is a direct track-by-track particle identification. Therefore, the raw yield of primary particles can be directly determined from the dca_{xy}-distribution. The dca_{xy} of all tracks passing the quality and PID cuts is filled into a histogram as shown in figure 3.8 for each p_t-bin. The distribution is then fitted with a combination of Monte-Carlo templates in order to determine the raw yield. In the case of pions and anti-protons, two templates are used: one for primary particles and one for all particles originating from weak decays. It must be noted that in this approach, the feed-down correction depends in second order on the composition of secondaries in the

particle	lowest p_t	TOF information required	highest p_t
π	≈ 0.20 GeV	> 0.65 GeV	≈ 1.2 GeV
K	≈ 0.25 GeV	> 0.60 GeV	≈ 1.2 GeV
p	≈ 0.45 GeV	> 0.80 GeV	≈ 2.0 GeV

Table 3.3: Lower and upper momentum cut-offs of the TPC-TOF analysis.

MC generator as different species decay with different lifetimes and can thus influence the shape of the template. However, as can be seen in figure 3.8, the combination of templates can well reproduce the data. For protons a third template is added describing the secondary contamination from material interactions. For other particles, this contamination is negligible.

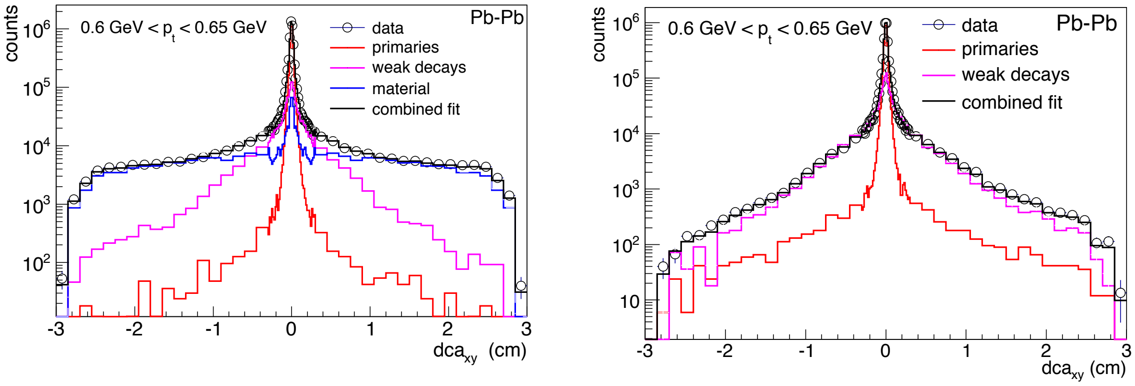

Figure 3.8: dca_{xy} of protons (left) and anti-protons (right) in the p_t-range between 600 MeV and 650 MeV together with the MC templates which are fitted to the data. The plot shows data from Pb–Pb collisions from 0%-5% central collisions.

The actual implementation of the template fit is done via the procedure described in [50] which is available in the ROOT software package as *TFractionFitter*. In this method, the uncertainties of both data and the Monte Carlo template are taken into account. The template prediction is allowed to vary in each bin within the statistical error. Therefore, the combined fit in figure 3.8 does not agree exactly with the sum of the shown scaled MC templates, but only within the statistical uncertainties of the templates.

A close look on the MC template for the proton contamination from secondaries shows a small unexpected peak at the center similar to primary particles which is absent in pp events. A detailed investigation shows that this effect is increasing with the multiplicity in the event. It can be shown that it is due to the association of fake clusters in one of the two pixel layers. In a high multiplicity event, secondary protons originating from material interactions behind the first two pixel layers and with a primary-like track topology can find a corresponding hit from another true primary particle (e.g. with very low momentum). A similar behavior is observed for electrons from γ-conversions which can also appear as fake primaries in a high multiplicity environment.

3.2.4 Efficiency correction

Not all primary particles produced in the collision reach the tracking detectors or pass the applied track quality cuts, because of hadronic interactions, energy loss in the detector material, dead zones (acceptance), decay etc. Therefore the obtained raw spectra are corrected for the reconstruction efficiency ϵ. The efficiency is obtained by running the same analysis on Monte Carlo generated events. The relevant generators and tunes for the analyses presented in this thesis are: PYTHIA D6T (pp), PYHTHIA PERUGIA-0 (pp), PHOJET (pp), HIJING (Pb–Pb).

The particles were propagated through the detector with a full simulation based on the GEANT3 code [51]. Dead channels (e.g. missing ITS layers) and changing beam conditions (primary vertex spread) were taken into account on a run-by-run basis in the MC events using so-called anchor runs.

Def. 15 (*Reconstruction efficiency ϵ*)

In this analysis, the reconstruction efficiency is defined as

$$\epsilon = \frac{\text{number of true reconstructed primary tracks } N_{\text{rec.prim}}}{\text{number of generated particles } N_{\text{gen}}}, \qquad (3.7)$$

where the particle type and origin of the reconstructed tracks are checked with MC truth information.

Figure 3.9 show the obtained efficiencies for Pb–Pb events in different centrality classes. Please note that - within this definition of efficiency - a direct comparison to similar plots is not straightforward as they might correspond to different data taking periods and thus to a different amount of dead channels (in particular in the SPD).

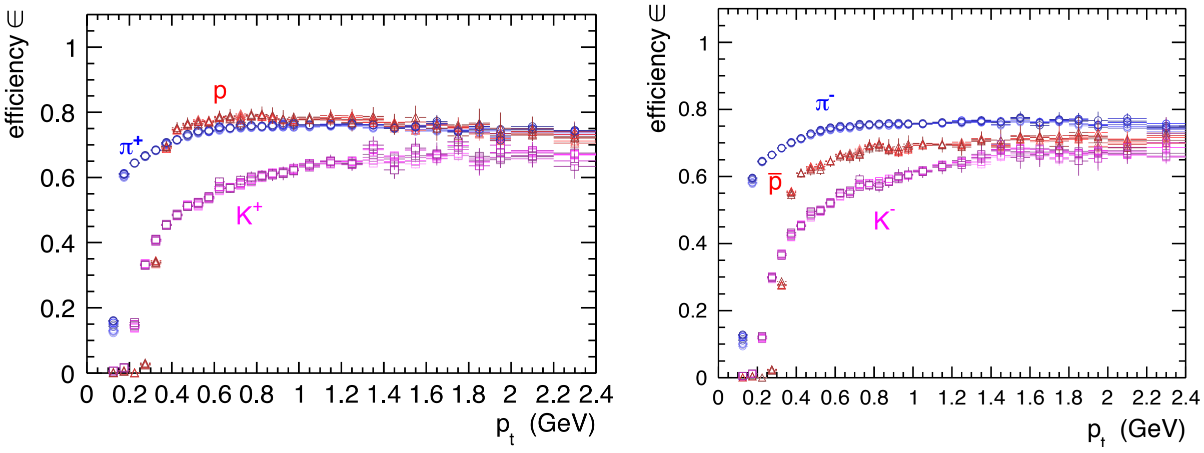

Figure 3.9: Reconstruction efficiency for positive and negative particles. The different color gradients correspond to specific centrality classes.

For kaons, the reduction of efficiency due to decays ($c\tau \approx 3.7$ m) is clearly visible as it reduces the efficiency by about 30% at 0.25 GeV and about 12% at 1.5 GeV. A similar effect can be observed for pions but on a much smaller level – in particular in comparison to protons – as the lifetime is significantly larger ($c\tau \approx 7.8$ m). One can also clearly observe a lower efficiency for anti-protons compared to protons at low momenta due to hadronic interactions. The falling edge of the efficiency curves towards lower momenta leads to a natural cut-off of the spectra at 200 MeV for pions, 250

MeV for kaons, and 400 MeV for protons. Please note, that the kinetic energy E_{kin} of a 400 MeV proton is only 80 MeV.

3.2.5 Additional corrections

In the case of the $n\sigma$-approach, the analysis with a certain PID technique in one of the detectors is stopped when the contamination from other particle species becomes too large whereas the unfolding naturally removes contamination from other particle species. However, muons must be treated exceptionally as they cannot be separated from pions based on time-of-flight methods and in the TPC only at very low momenta ($p < 180$ MeV). The muon contamination of the pion spectrum presented in this analysis is corrected based on the observed particle composition in the reconstructed tracks from MC events and is of the order of 2%-3% with only a small dependence on transverse momentum. Most of these tracks stem from decays of charged pions and kaons into muons out of which a small fraction passes the cut on the dca to the primary vertex.

Absorption correction

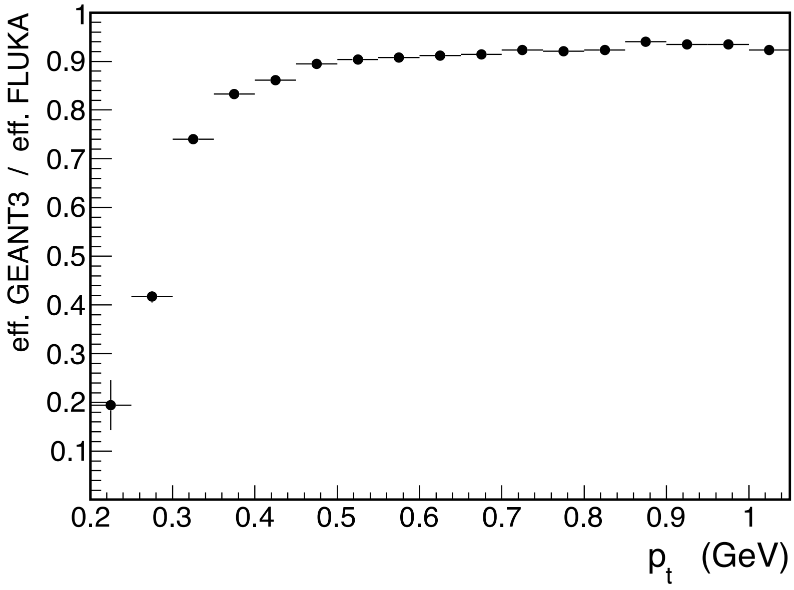

Figure 3.10: Difference between the anti-proton reconstruction efficiency from GEANT3 and FLUKA due to the overestimation of the absorption cross-section in GEANT3.

It turns out that the absorption cross-sections for anti-protons which are implemented in GEANT3 are significantly larger than those observed in measurements [52]. This effect is taken into account by multiplying the resulting anti-proton spectrum with a p_t-dependent correction factor which is obtained from a comparison with the anti-proton efficiency which is extracted with the FLUKA [53] transport code. The correction factor is shown in figure 3.10. A similar correction is applied for kaons, but it is of much smaller magnitude ($< 3\%$). This effect is also important for future fluctuation studies of the net baryon production and the measurement of anti-nuclei.

3.3 Systematic error of the measurements

The systematic errors of the measurement have to be estimated individually for pions, kaons, and protons since different effects are dominating for the different species. Some of the effects mentioned below show a strong dependence on the event multiplicity and are thus different in pp and Pb-Pb collisions. In addition to this, most of the systematic effects show a significant p_t-dependence.

3.3.1 Energy loss in material (material budget)

Several systematic effects are related to the material in front of the TPC which consists mainly of the beam pipe and the structures of the Inner Tracking System. This affects in particular

1. the amount of secondary protons which are produced in the material,
2. absorption of anti-matter due to hadronic interactions, and
3. corrections for energy loss through electromagnetic interactions (Bethe-Bloch) in the material.

The knowledge of the material budget in ALICE is quite precise as it is well measured via γ-conversions to an accuracy of -3.9% and +4.2% [54]. Consequently, the systematic errors related to (1.) and (2.) are completely dominated by the imprecise representation of the corresponding cross-sections in the transport code and are discussed in the following sections.

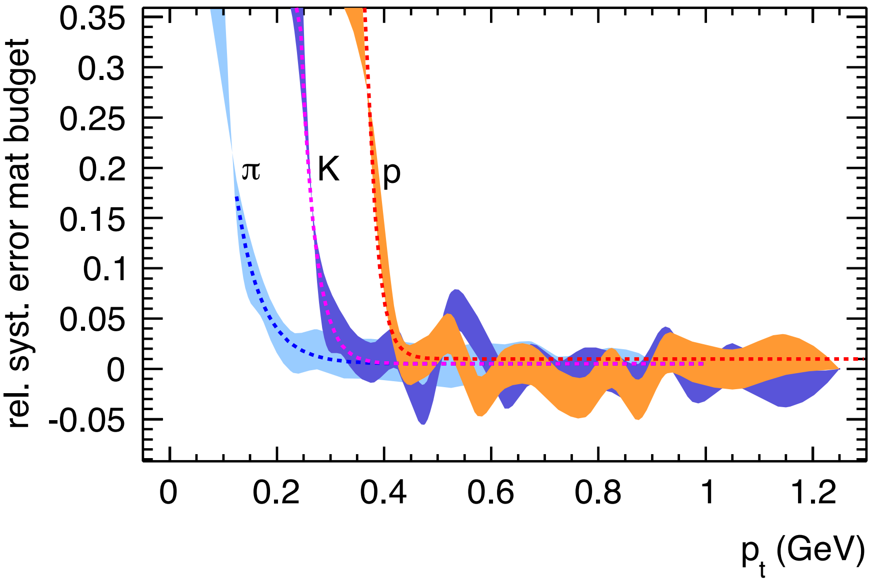

Figure 3.11: Systematic error related to uncertainties in the knowledge of the material budget and the corresponding energy loss corrections for the different particle species. The bands correspond to the uncertainty in the determination of this systematic error caused by the limited statistics of the MC samples with de- and increased material budget.

On the other hand, effects of multiple scattering and energy loss through ionization are reasonably well described by the transport code and their uncertainty is dominated by the knowledge of the material budget of the detector. The effect has been assessed by a comparison of the obtained efficiency

systematic effect	estimation procedure	$\pi^{\pm}$	$K^{\pm}$	$p, \bar{p}$	$\frac{K}{\pi}$	$\frac{p}{\pi}$	$\frac{\pi^-}{\pi^+}$	$\frac{K^-}{K^+}$	$\frac{\bar{p}}{p}$
material budget	compute efficiency based on MC production with increased and decreased mat. budget	3%..1%	3%..1%	5%..1%	does not cancel	does not cancel	cancels	cancels	cancels
secondaries material	variation of fit templates, dca_z-cut	$< 1\%$	$< 1\%$	2%..1% (5%..2%)	does not cancel	does not cancel	$< 1\%$	$< 1\%$	2%..1% (5%..2%)
weak decays	variation of fit templates, dca_z-cut, strict sum of templates instead of TFractionFitter	3%..1% (4%..2%)	$< 1\%$	5%..1% (10%..3%)	does not cancel	does not cancel	$< 1\%$	$< 1\%$	2%..1%
hadronic interaction	20%-30% of the percentage of particles lost due to hadr. interaction in GEANT3	3%..1%	3%..1%	6%..2% (smaller for p compared to $\bar{p}$)	does not cancel	does not cancel	4%..2%	4%..2%	6%..2%
PID	comparison with 2σ and 4σ cuts	3%..1.5% (4%..2%)	3.5%..2% (4.5%..2.5%)	1%..2% (1.5%..2.5%)	does not cancel	does not cancel	cancels	cancels	cancels
tracking	variation of track quality cuts	3%-4%	3%-4%	4%-5%	1%-2%	2%-3%	$< 1\%$	$< 1\%$	$< 1\%$

Table 3.4: List of the different contributions to the systematic error. The systematics for the ratios in the last columns have been evaluated individually as some effects (partly) cancel. Values in brackets indicate increased systematics in most central collisions (Pb–Pb 0%-5%).

from two MC samples with an increased and decreased material budget. The variation was chosen to be ± 20% as a conservative approach since not all modifications to the detector material configuration were already implemented in the used MC samples. As one can see from the comparison of the extracted efficiencies from the different MC samples, this uncertainty is strongly reflecting the $\frac{1}{\beta^2}$-dependence of the energy loss for the different particle types. It shows a strong p_t-dependence which can be roughly described by an exponential. In the range relevant for the individual spectra, the errors are of the order of 3%, 3%, and 5%, for pions, kaons, and, protons at the respectively lowest p_t-bin and then quickly decrease further as shown in figure 3.11. This error is assumed to be independent of the event multiplicity. For all other particle species, the contamination from secondaries from material is negligible.

3.3.2 Secondaries from material

As already stated above, the relevant cross-sections for the creation of secondary particles from interactions with detector material are largely underestimated by the GEANT3 propagation code. However, the corrections are only relevant for protons at very low momenta (400 MeV $< p_t <$ 500 MeV) and are mainly important for an investigation of the proton to anti-proton ratio as a function of transverse momentum. The template fits of the dca-distribution take this effects properly into account, but a closer analysis with different MC templates (e.g. with and without dca_z-cut, shorter fit ranges) show that there are systematic differences of the order of 1-2% in the relevant p_t-range.

3.3.3 Secondaries from weak decays

The systematic error of the feed-down correction is mainly determined in a similar fashion by a variation of fit ranges and template shapes (with and without dca_z-cut etc.). In addition to this, the fit method of the templates was changed from the *TFractionFitter* to a strict sum of the templates. The resulting systematic effects remain small for pions ($\approx$ 3% at 200 MeV and $\approx$ 1.5% above 1 GeV). For kaons, no correction for feed-down is applied as the only particles with macroscopic lifetimes decaying into kaons are produced with much smaller abundance, e.g. the Ω and D^0.

In the case of protons, the systematic error related to the feed-down correction is dominant. Secondary protons originate mainly from Λ-decays, but also from the decays of $\Sigma^+ \rightarrow p\pi^0$. As there are no measurements of the Σ-yield available, it is difficult to constrain this contribution. In future, the measurement of the complete collection of strange particles will be completed including a possible measurement of $\Sigma^0 \rightarrow \Lambda\gamma$ and allow for a more detailed understanding.

The error is quickly decreasing with increasing p_t, but increasing with multiplicity as the rejection of secondaries via the requirement of hits in the SPD layers is less effective in central collisions due to the association of fake clusters.

3.3.4 Absorption effects

Besides the already discussed problems with anti-protons, a detailed comparison of π-A and K-A data with the cross-sections for hadronic interaction of low momentum kaons and pions in GEANT3 also shows differences of about 20-30%. After folding with the relevant percentage of particles which are lost by hadronic interaction before entering the TPC, the resulting error is of the order of 2-3% for K^- and pions and below 1% for K^+.

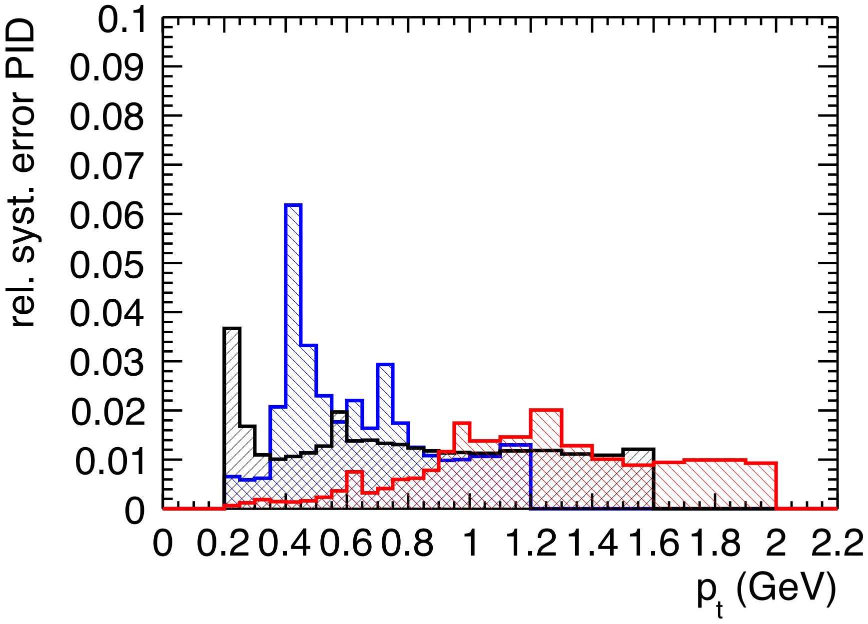

Figure 3.12: Relative systematic error due to particle identification obtained from comparison of different nσ-cuts (pions in black, kaons in blue, protons in red), please note that the kaon-electron crossing at $p_t \approx 450$ MeV is removed from the spectrum. Results shown are for Pb-Pb 0-5% central collisions. In lower multiplicity environments the errors are smaller.

3.3.5 PID contamination

In the $n\sigma$-approach, the systematics related to the contamination from other particle species can be conservatively evaluated by a comparison of the corrected spectra obtained with 2σ- and 4σ-cuts. The p_t-dependence of these errors is non-trivial as it is negligible in regions of clear separation whereas it becomes large in the overlapping regions of the Bethe-Bloch curve. The same holds true even after requiring the corresponding 3σ-cut in TOF as mismatch cannot be as effectively reduced. As pions are the most abundant particles, their corresponding systematic error does not exceed 2%-3% in the crossings whereas it can reach up to 4-5% for kaons. In terms of particle identification, protons are the easiest and the related systematics are typically below 1.5%. As the $\mathrm{d}E/\mathrm{d}x$-resolution becomes slightly worse with increasing multiplicity, the systematic error shows a similar slight increase. The values quoted here correspond to the 0-5% most central collisions.

In the case of Gaussian unfolding, the systematic error related to the PID contamination can be directly obtained from the fit parameter errors of the multiple Gaussians.

3.3.6 Tracking and matching (track quality cut variation)

The systematic effects related to the track quality cuts and the matching between Inner Tracking System and Time Projection Chamber were mainly investigated by a variation of the track cuts. E.g. the cut on the number of clusters was varied between 65 and 100, the χ^2/n_{cl}-cut between 3.5 and 7, the requirement on the number of ITS clusters between at least one in SPD and four hits etc. At low momenta, the largest variations are observed in the case of pions and kaons, because of their possible

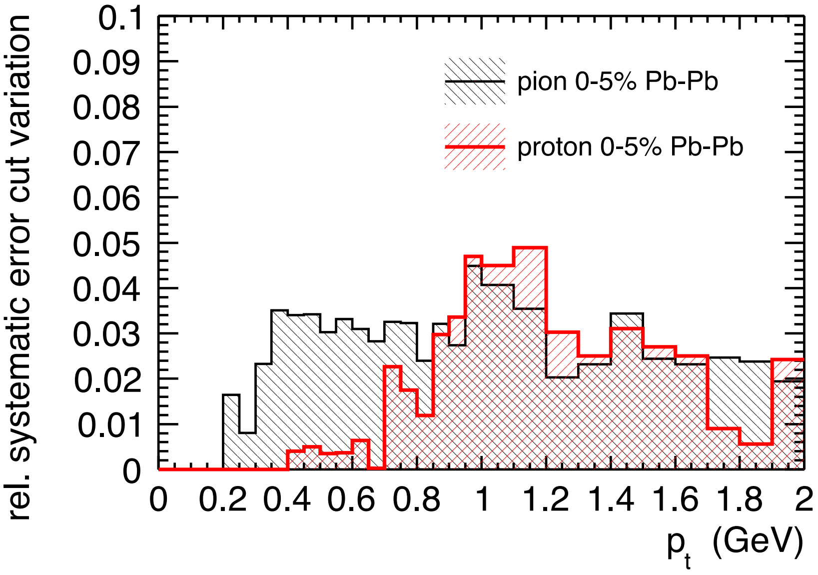

Figure 3.13: Relative systematic changes due to cut variations obtained from comparison of a soft with a hard cut set. Results are shown for Pb-Pb 0-5% central collisions. In lower multiplicity environments the errors are smaller.

decays inside of the detector with the related uncertainties of kink reconstruction. For protons, the observed effects are of the order of 2-3% and for kaons and pions of the order of 3-4% for most central Pb–Pb collisions and decreasing towards more peripheral or pp collisions.

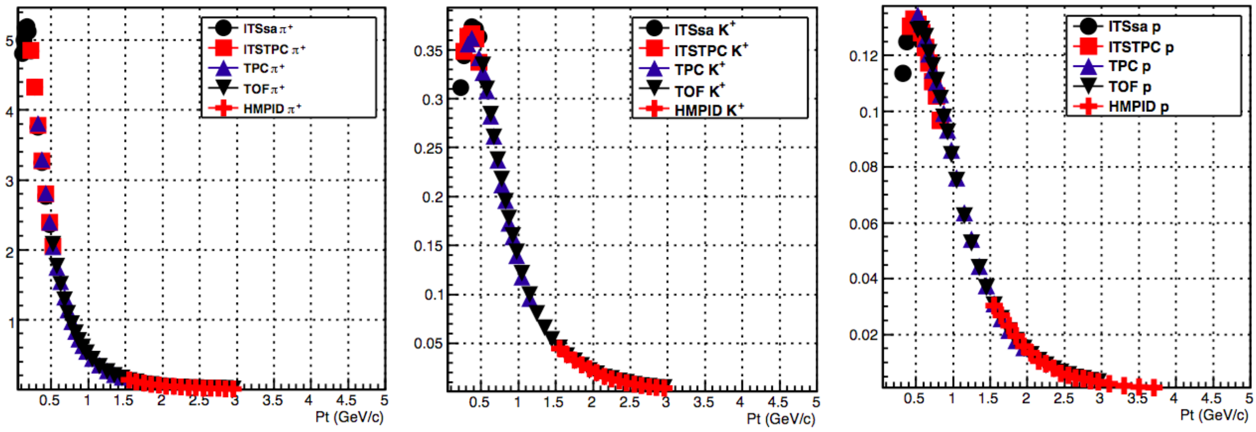

Figure 3.14: Pion (left), kaon (middle), and proton spectra (right) of the individual analyses from pp collisions at 7 TeV. The analysis presented in this thesis corresponds to the blue triangles.

3.4 Combined spectra

Analysis with particle identification only in the TPC or with the combined $n\sigma$-cut in the *TPC-TOF*-approach can cover a large and important part of the p_t-spectrum, but errors due to extrapolation can be significantly reduced by combining with other analyses. At low momenta, ITS stand-alone tracks can be used and unfolding procedures in the TOF at high momenta. In addition to this, in the spectra analysis of 7 TeV pp collisions two more analyses are contributing. Firstly, the HMPID spectra contribute at higher momenta and are extracted based on an unfolding procedure slightly extending the covered momentum region. Secondly, the *ITS-TPC*-analysis serves as a further cross-check. It uses the particle identification from the ITS, but global tracks from the combined TPC and ITS tracking.

As there are significant overlap regions between the different detectors/analyses, they can also serve as a cross-check of the results. Details of the other analyses and the combination of the individual spectra can be found in [55]. As can be seen in figure 3.14, the overall agreement between the different detectors/analyses is better than 5% in pp collisions. In Pb–Pb collisions, the agreement is slightly worse towards central events, but always better than 10%. The individual spectra can be combined bin-by-bin where the assigned systematic and statistical error serves as a weight. Figures 3.17(a), 3.17(b), and 3.17(c) show the preliminary spectra from Pb–Pb collisions at $\sqrt{s_{NN}}$ = 2.76 TeV in several centrality bins. The preliminary spectra from pp collisions at $\sqrt{s}$= 7 TeV and the final spectra from 900 GeV are shown in figures 3.15 and 3.16.

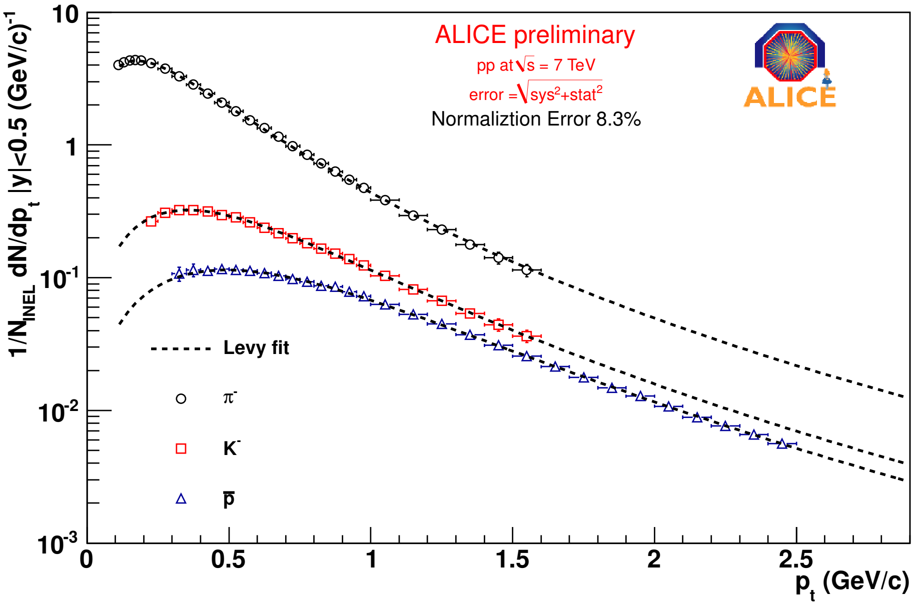

Figure 3.15: Combined pion, kaon, and proton spectra from pp collisions at 7 TeV. The lines represent the fits with the Levy/Tsallis functions.

The combined spectra are fitted with different functions in order to obtain the yield dN/dy and the mean transverse momentum $< p_t >$. The spectra from pp collisions are fitted with the Levy/Tsallis function [56]

$$\frac{\mathrm{d}^2N}{\mathrm{d}p_t\mathrm{d}y} = p_t\frac{\mathrm{d}N}{\mathrm{d}y}\frac{(n-1)(n-2)}{nC(nC+m_0(n-2))}\left(1+\frac{m_t-m_0}{nC}\right)^{-n}. \tag{3.8}$$

The yield dN/dy and the function parameters C and n are determined from the fit which gives a good description of the spectra. The parameter C is often interpreted as a temperature as it is related to the slope of the spectrum at low momenta. The extrapolated region amounts to about 10% for pions, 13% for kaons, and 21% for protons. In order to asses the systematics of the extraction of the yield and mean transverse momentum due to the extrapolated region at low momenta, the spectra is also fitted with similar functions. The modified Hagedorn function [57]

$$\frac{1}{2\pi p_t}\frac{\mathrm{d}^2N}{\mathrm{d}p_t\mathrm{d}y} \propto \frac{p_t}{m_t}\left(1+\frac{p_t}{p_0}\right)^{-b} \tag{3.9}$$

with the parameters (b,p_0) or the UA1 parametrization [58]

$$\frac{1}{2\pi p_t}\frac{\mathrm{d}^2N}{\mathrm{d}p_t\mathrm{d}y} = \begin{cases} B\cdot\exp(-bm_t)\ , & \text{if } p_t < p_t^* \\ A\cdot(1+p_t/p_0)^{-b}\ , & \text{if } p_t > p_t^* \end{cases} \tag{3.10}$$

are commonly used for this purpose. In general, these functions show the common behavior that they are similar to an exponential at low momenta and to a power law towards higher momenta.

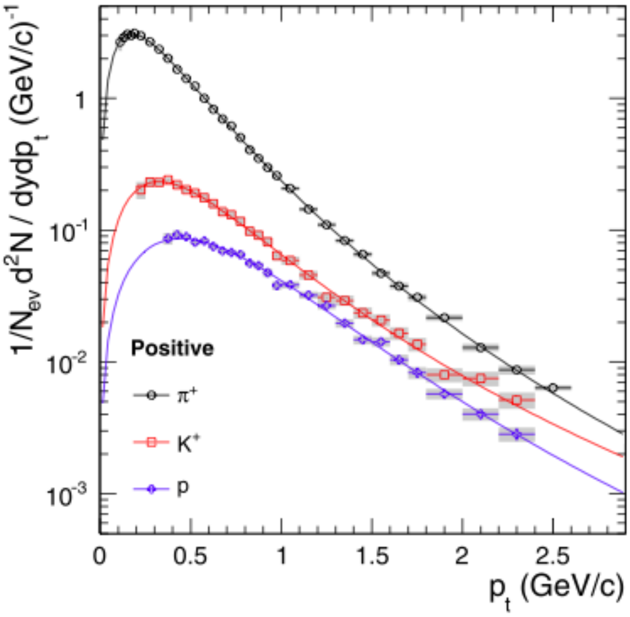

Figure 3.16: Combined pion, kaon, and proton spectra from pp collisions at 900 GeV. The lines represent the fits with the Tsallis functions.

In Pb–Pb collisions, the spectra are fitted with blast-wave fits (see also chapter 6.1) with individual parameter sets for each spectrum. The functional form is given by [59]

$$\frac{1}{m_t}\frac{\mathrm{d}N}{\mathrm{d}m_t} \propto \int_0^R I_0\left(\frac{p_t\sinh\rho}{T_{fo}}\right)\cdot K_1\left(\frac{m_t\cosh\rho}{T_{fo}}\right)\cdot r\mathrm{d}r \tag{3.11}$$

where $I_0(x)$ and $K_0(x)$ represent the modified Bessel functions. The dependence on the velocity profile is given by $\rho = \tanh^{-1}\beta_r$ with $\beta_r = (\frac{r}{R})^n\beta_t$. Except for the yield, the only free parameters are the freeze-out parameters kinetic temperature T_{fo}, velocity β_t, and n. A fit with individual parameters for each particle type gives the best precision for the extraction of yields and mean transverse momenta. A fit with a single parameter set for all three species in the different centrality bins is presented in chapter 6.1.

Radial flow effects are boosting the spectra towards higher momenta with increasing centrality in Pb–Pb collisions. This slightly reduces the extrapolated region at lower momenta to about 5% for pions, 6% for kaons, and 7% for protons, respectively. The related systematic errors amount to 2.5%, 3.5%, and 3.5%. In order to obtain the error on the integrated yield, this contribution is added in quadrature to the linear sum of the bin-by-bin errors (6% / 7% / 7.2%), which then amounts to a total error of $\sqrt{(6\%)^2 + (2.5\%)^2} \approx 6.5\%$ for pions, $\sqrt{(7\%)^2 + (3.5\%)^2} \approx 7.8\%$ for kaons, and $\sqrt{(7.2\%)^2 + (3.5\%)^2} \approx 8\%$ for protons.

The resulting yields and values for $< p_t >$ are discussed in the following chapter together with a general assessment of strange particle production at LHC energies.

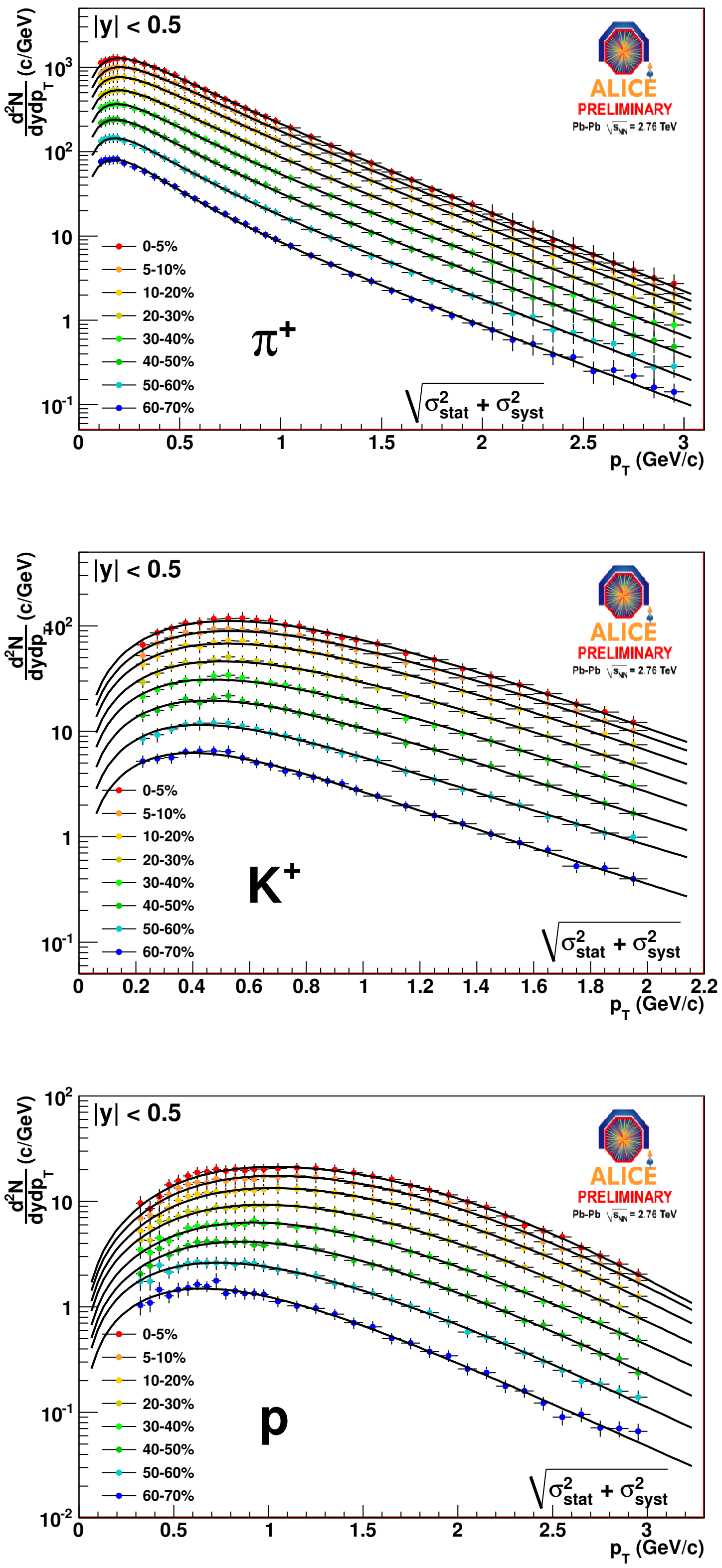

Figure 3.17: Combined pion (top), kaon (middle), and proton spectra (bottom) from Pb–Pb collisions at 2.76 TeV. The lines represent the blast-wave fits with individual parameters for each particle type.

4 Measurement of strange particle production

The measurement of charged pions, kaons, and protons provides only a starting point for the complete characterization of the light flavor production in relativistic heavy-ion collisions. For a consistent picture, a measurement of the production yields of Λs, Ξs, and Ωs is needed in addition. This is of importance not only for the comparison with models, but also because weak decays of strange particles feed into the states with lower mass, i.e.

$$\begin{aligned}\Lambda &\longrightarrow \mathrm{p}\pi\ (63.9\%)\\ \Xi &\longrightarrow \Lambda\pi\ (99.87\%)\\ \Omega &\longrightarrow \Lambda K\ (67.8\%)\,.\end{aligned}$$

The following section tries to give an overview over the existing results of strange particle production together with the results for pions and protons. Thus the results obtained in the previous chapter are put into the context of complementary results from the experiment.

4.1 Topological particle identification

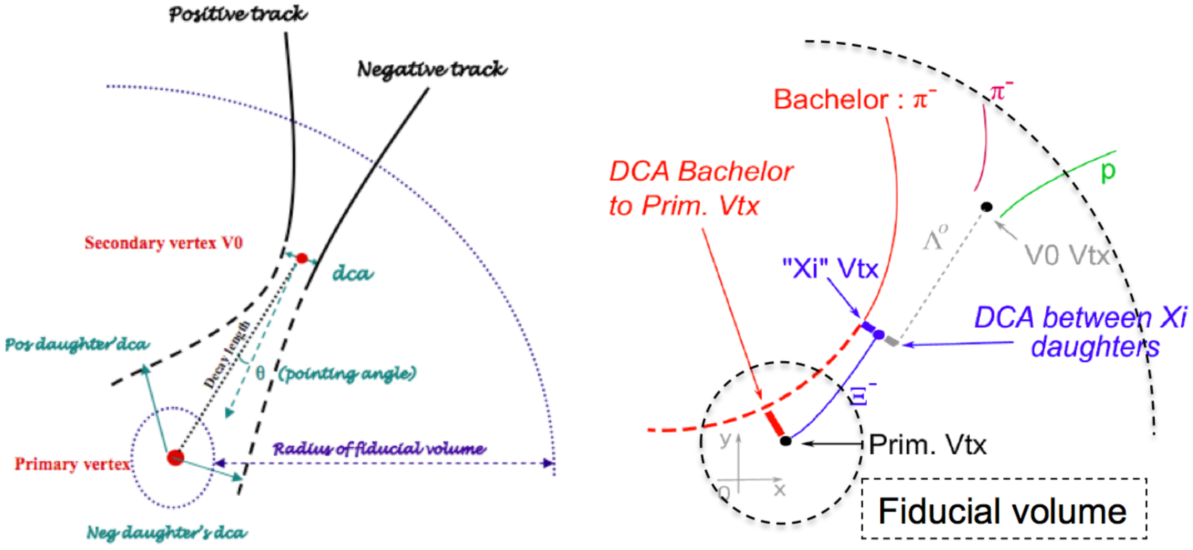

(a) (b)

Figure 4.1: Particle identification via the V^0-topology (left) and the cascade topology (right).

As it was shown in the previous chapter, charged pions, kaons, and protons are directly identified based on their specific energy loss $\mathrm{d}E/\mathrm{d}x$ in the ITS and TPC as well as time-of-flight measurements in the TOF detector. In contrast to this, the decays of K^0_Ss, Λs, Ξs, and Ωs are reconstructed as secondary vertices and the particles are identified on topological basis. The neutral particle decays $\mathrm{K}^0_s \rightarrow \pi^+\pi^-$ and $\Lambda \rightarrow \mathrm{p}\pi$ result in two opposite charge daughter tracks. Therefore, they are often referred to as V^0-decays. The first step of the V^0-finding is the selection of all opposite charge track pairs with a small distance of closest approach $DCA < 0.5$ cm. The decay vertex is associated to the connecting line between the two points of closest approach between the two daughters. The combinatorics are drastically increasing with decreasing radial distance R of the secondary vertex to the primary vertex. Therefore a minimal distance of $R > 0.2$ cm is typically required. In addition to this, the reconstructed momentum vector of the mother particle must point back to the primary vertex. This is ensured by a cut on the corresponding pointing angle $\cos(\theta_p) > 0.99$. Especially at low momenta and in the high multiplicity environment, the combinatorics can be significantly reduced with the help of *indirect* particle identification, e.g. 3σ-cuts in the TPC largely reduce the background without loss of efficiency.

The Ξ^- and Ω^- particles show a cascade topology. Reconstructed lambdas without a cut on the pointing angle are combined with possible secondary tracks (bachelor candidates). Only those bachelor tracks are selected which exhibit a small distance to the reconstructed V^0 flight line. The topological identification of the Ω^- is slightly more difficult than for the Ξ^-, because of its shorter lifetime ($c\tau = 4.91$ cm compared to 2.5 cm). However, the background rejection via particle identification is more powerful as the bachelor track is a kaon. Further details of the topological particle identification and the relevant selection criteria can be found in [49, 60, 61]. Figure 4.1 illustrates schematically the V^0 and cascade topology.

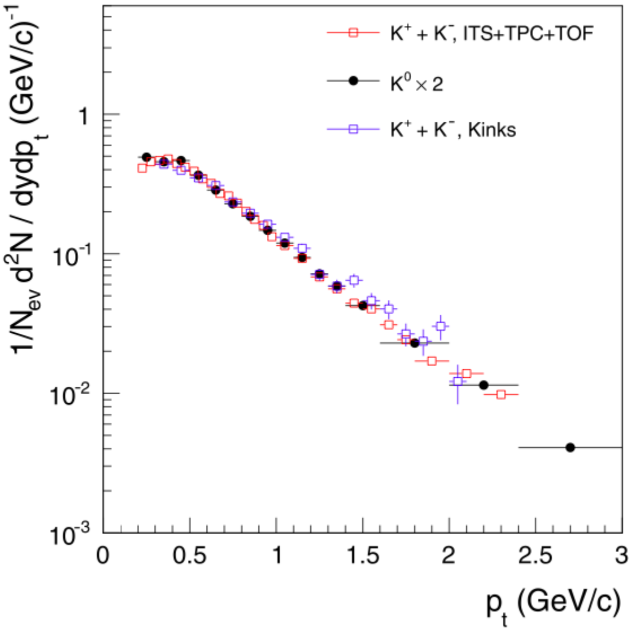

Figure 4.2: Comparison of charged kaon spectra from pp collisions at $\sqrt{s} = 900$ GeV obtained with the direct identification from ITS, TPC, and TOF together with the spectra from the kink and K^0_S analysis. Only statistical errors are shown in the plot. From [62].

The spectra of kaons can actually serve as an important cross-check as they can be measured with five independent techniques: via the measurement of dE/dx, time-of-flight, Cherenkov radiation, as well as the V^0-type decay $K^0_s \rightarrow \pi^+\pi^-$, and the kink topology $K^+ \rightarrow \mu^+\nu_\mu$. Figure 4.2 shows the excellent agreement which was found in pp collisions at a center of mass energy of 900 GeV. Please note, that one expects small differences between the two particle species from ϕ-decays which occur with different probability into K^+K^- (48.9%) and $K^0_S K^0_L$ (34.2%) pairs. Please note, that decays of K^0_L are not detected within the ALICE experiment due to their long lifetime ($c\tau = 15.34$ m). Estimates from thermal model calculations show a 4% higher yield of charged with respect to neutral kaons. Similar comparisons with charged and neutral pions are currently under study.

4.2 Dependence of strangeness production on $\sqrt{s}$ and collision system

With the comprehensive ALICE data in pp and Pb–Pb collisions [62, 49, 61, 63, 60], the production of strange particles can be interpreted over a broad range of energies in these collision systems. A comparison with lower energy data from other accelerators allows to identify trends in particle production. The comparison with RHIC data is of particular interest in this context.

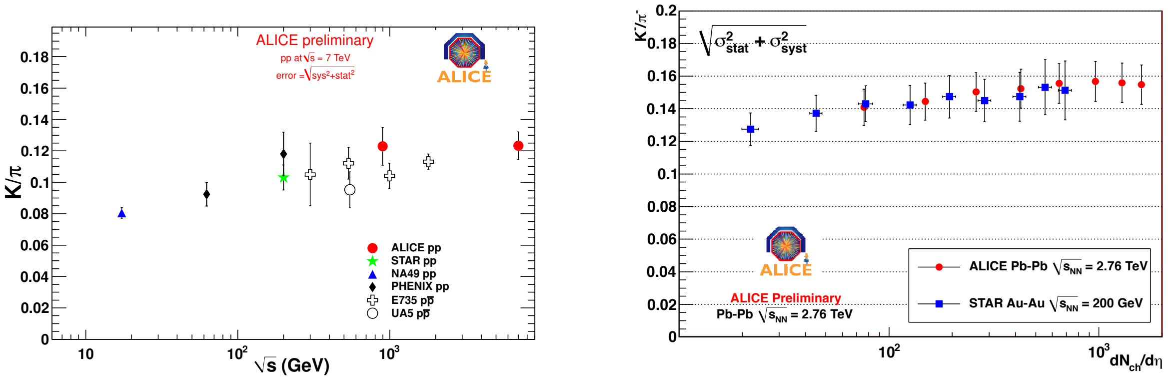

(a)

(b)

Figure 4.3: Production yields of kaons as a function of $\sqrt{s}$ in pp collisions (left) and as a function of centrality in Pb–Pb collisions (right) compared with data from other experiments.

4.2.1 Kaon production

The production of kaons normalized to the number of pions shows only a weak increase from SPS to LHC energies in pp collisions (see figure 4.3(a)). Future measurements at the top LHC energy of 14 TeV will show whether similar values of this ratio as in Pb–Pb collisions can be reached also in elementary reactions. Similar to RHIC energies, the kaon production relative to pions increases moderately with centrality in Pb–Pb collisions and reaches a value of about 0.16 in most central collisions. In total, this leads to a roughly 30% higher production yield of kaons with respect to pions in central Pb–Pb compared to pp collisions.

Another interesting result is the often poor description of strangeness production in pp collisions by event generators like PYTHIA which underestimate the kaon production by up to a factor of three depending on the specific tune and the examined p_t-range [62, 49]. This deviations are typically increasing with increasing strangeness content and can amount to a maximum of a factor of 10 when comparing the measured omega yields with e.g. the Perugia-0 tune of PYTHIA [64]. This also implies that these generators cannot be used for feed-down corrections.

4.2.2 Proton production

In pp collisions, the proton yield relative to the pion yield remains basically constant from RHIC to LHC energies whereas the anti-proton yield shows a slight increase until it reaches the same value as the proton yield in the LHC energy regime (see figure 4.4(a)). In contrast to strange particles, the p/π-ratio shows no dependence on centrality in Pb–Pb collisions (see figure 4.4(b)). Please note, that comparisons with lower energy data are not unambiguous since feed-down corrections are implemented differently in the experiments. The PHENIX collaboration publishes (anti-)proton

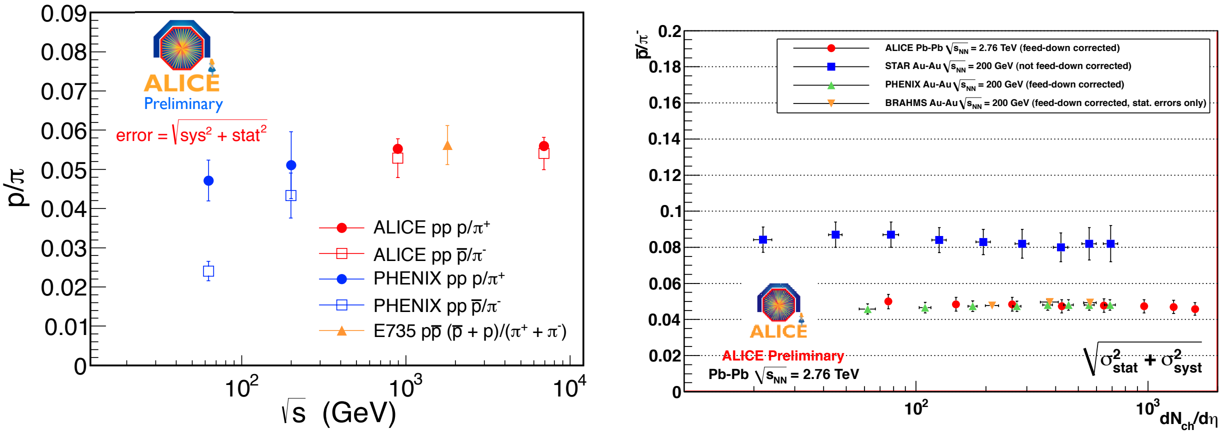

(a)

(b)

Figure 4.4: Production yields of protons as a function of $\sqrt{s}$ in pp collisions (left) and as a function of centrality in Pb–Pb collisions (right).

yields which are corrected for all protons from weak decays except for protons from Σ^+-decays [65]. Even though not specified in the publication, probably no feed-down correction was applied for pions [66]. Nevertheless, the observed pion yield is significantly smaller than the value published by the STAR collaboration which was corrected for feed-down based on MC events [67]. In contrast to this, the STAR proton spectra are either corrected to an inclusive spectrum [68] or correspond to a fiducial volume given by a primary track selection of a maximum distance of closest approach to the primary vertex of 3 cm [67]. Precise conclusions on the evolvement of the p/π-ratio between RHIC and LHC energies are therefore difficult to constitute.

double ratio	ALICE (LHC 2.76 TeV)	STAR (RHIC 200 GeV)
$\frac{K/\pi\|_{PbPb}^{0-20\%}}{K/\pi\|_{pp}}$	1.27 ± 0.17	1.55 ± 0.27
$\frac{\Xi/\pi\|_{PbPb}^{0-20\%}}{\Xi/\pi\|_{pp}}$	1.49 ± 0.35	3.8 ± 1.1
$\frac{\Omega/\pi\|_{PbPb}^{0-20\%}}{\Omega/\pi\|_{pp}}$	3.3 ± 1.1	6.8 ± 2.7

Table 4.1: Strange particle production in Pb–Pb collisions relative to the one in pp for different energy regimes. For the ALICE data, the 7 TeV data was chosen as pp reference as there is only a weak dependence on $\sqrt{s}$ betwenn 2.76 TeV and 7 TeV in pp. All ratios are the sum of positive and negative particles. The double ratio of Ωs in Pb–Pb from the STAR collaboration corresponds to 0-5%. The STAR data is taken from [67].

4.2.3 Multi-strange particle production

Also the yields of the multi-strange particles Ξ and Ω in Pb–Pb collisions do not change from RHIC to LHC energies if they are normalized to pions as shown in figure 4.5(b). An interesting feature of strange particle production is the enhanced production in Pb–Pb relative to pp collisions. The double ratios of the K/π, Ξ/π, and Ω/π ratio show a significant increase proportional to the strangeness content. The preliminary values are summarized in table 4.1. A comparison with similar variables at RHIC and SPS energies shows that this effect is decreasing with increasing $\sqrt{s_{\mathrm{NN}}}$. This observation is in disagreement with the argument that strangeness enhancement can serve as a signature of the QGP [69]. Since the lifetime and initial temperature of the QGP produced at the LHC are significantly larger than at RHIC or SPS, an increase of this effect would have been expected, but a further decrease is measured.

4.2.4 Particles and anti-particles

In contrast to RHIC energies, at the LHC energy regime the particle to anti-particle ratios are consistent with unity within the uncertainties of the measurement (see fig. 4.5(a)). The same observation holds true for pp collisions at 7 TeV. In a thermal view, the $\bar{p}/p$-ratio is of particular interest, because it shows a strong sensitivity on the baryo-chemical potential μ_B [70, 71]. As a consequence, the obtained values for μ_B are consistent with zero within the systematic uncertainties of the measurement (see also chapter 6). Since the systematic error on the $\bar{p}/p$-ratio cannot be easily reduced to a level in which the deviation from unity is significant, this implies a missing constraint on the baryo-chemical potential μ_B.

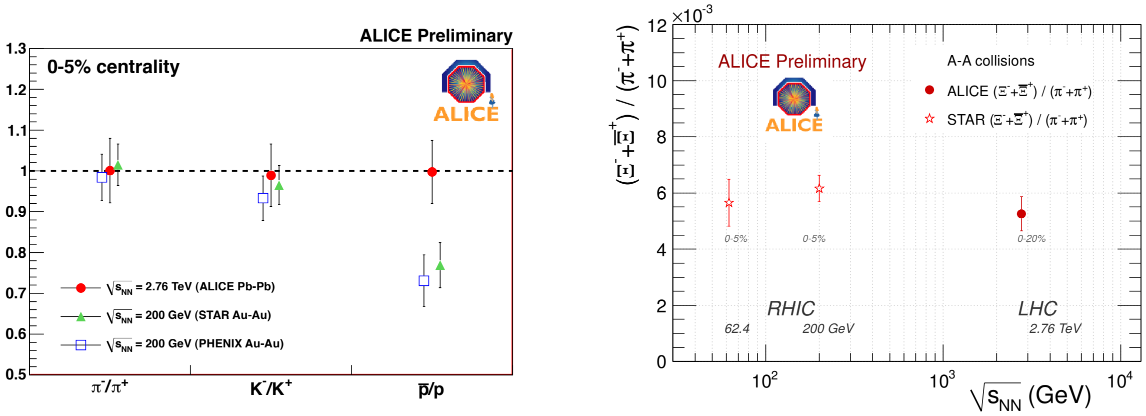

(a)

(b)

Figure 4.5: Particle to anti-particle ratios at RHIC and LHC energies (left). Ξ/π-ratio as a function of $\sqrt{s_{NN}}$ in Pb–Pb collisions (right).

4.3 Multiplicity dependence of pion, kaon, and proton production in pp collisions

The observed strangeness yields in pp collisions at 7 TeV relative to the production of non-strange particles are significantly lower than in A–A collisions at RHIC energies. Despite a 35 times larger center-of-mass energy, the chemical composition between the two collision systems is still dramatically different. As no resemblance between pp and Pb–Pb collisions can be observed in minimum bias spectra, a natural next step is the investigation of high multiplicity pp collisions.

The analysis for charged pions, kaons, and protons was therefore repeated in several multiplicity bins. The five multiplicity bins were chosen in such a way, that they contain an equal number of primary reconstructed tracks passing the standard cuts in $|\eta| < 0.8$. As illustrated in figure 4.6, bin number 1 contains all events with 0 to 5 tracks, bin number 2 all events with 6 to 9 tracks, bin number 3 all events with 10 to 14 tracks, bin number 4 all events with 15 to 22 tracks and bin number 5 all events with more than 23 tracks. The average multiplicity in bin 5 corresponds approximately to four times the average multiplicity in minimum bias collisions. Figure 4.6 shows the multiplicity distribution with the corresponding bins and the observed particle ratios in these bins relative to the results of the minimum bias spectrum. Within the errors, no dependence of the particle ratios on event multiplicity can be observed. This is in particular interesting, as the mean transverse momenta are significantly different with respect to the minimum bias spectrum. It rises by a factor of about 1.8 for pions, 1.7 for kaons, and 1.75 for protons between the first and last multiplicity bin.

The presented results are still in a very preliminary state. In particular, the influence of the multiplicity dependence of the particle composition in the event generator used for the now multiplicity dependent efficiency correction is not yet finally understood. Future measurements with improved statistics, in particular including high-multiplicity triggers, will clearly improve the multiplicity reach of the analysis. Then a direct comparison with peripheral Cu-Cu collisions at RHIC will be possible.

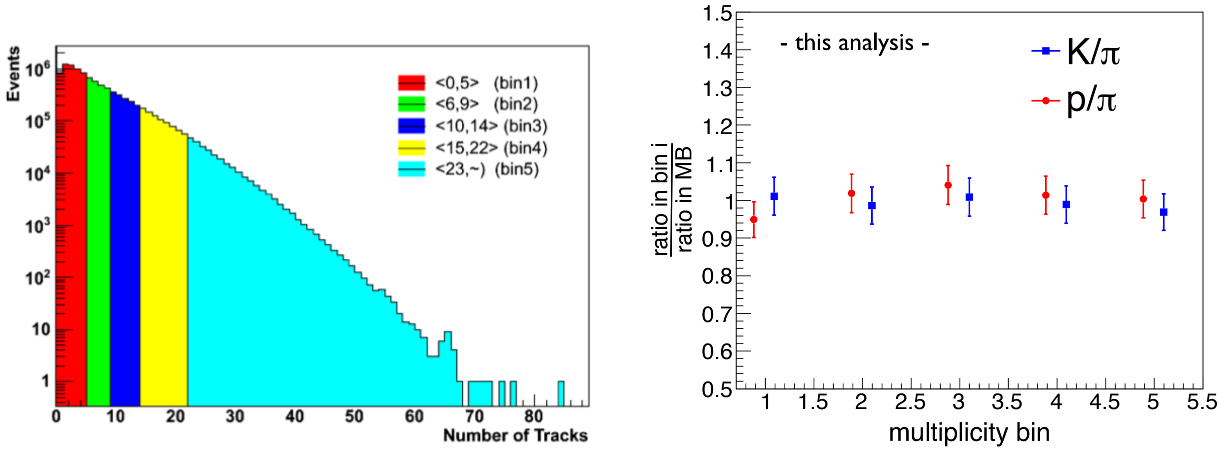

(a) (b)

Figure 4.6: Multiplicity distribution of reconstructed primary tracks in pp collisions at 7 TeV together with the corresponding multiplicity bins (left). Measured K/π and p/π ratios in these bins normalized to the ratio in minimum bias collisions (right).

4.4 Summary of the most important observations

With the results presented in this chapter, it is possible to make a first summary of the basic observations concerning the strangeness production in the new energy regime of the LHC.

Observation 1 (*Light flavor particle yields as a function of $\sqrt{s}$ in pp collisions*)

> The measured particle yields of kaons and protons relative to the pion production are rather independent of $\sqrt{s}$ and follow the trend from lower energies showing only a weak increase. In particular,

the strange to non-strange particle production remains significantly smaller than in A–A collisions even in the LHC energy regime.

Observation 2 (*Strangeness production in Pb–Pb collisions*)

Strange particle production is clearly less suppressed in Pb–Pb collisions compared to pp collisions due to canonical effects also at the LHC energy regime. Yet, the observed strangeness enhancement factors decrease from SPS to RHIC to LHC.

Observation 3 (*Multiplicity dependence in pp collisions*)

The very preliminary results indicate that the spectra become significantly harder towards higher multiplicities in pp collisions. Nevertheless, the average chemical composition seems to be not affected.

Observation 4 (*Particle to anti-particle ratios*)

Within the achievable systematics of the measurement, all particle to anti-particle ratios are consistent with unity in pp collisions at 7 TeV and Pb–Pb collisions at 2.76 TeV.

5 Anti- and Hyper-Matter production at the Large Hadron Collider

During the last 100 years, researchers in nuclear physics have explored the table of nuclides from the valley of stability to its boundaries on the neutron- and proton-rich side and up to the heaviest possible elements. High energy nuclear physics experiments like ALICE offer the unique possibility to study also the production of the corresponding anti-nuclei.

One of the main experimental challenges is given by the fact that these particles are only extremely rarely produced in comparison with abundant particles such as pions, kaons, and protons. Thermal model calculations and lower energy data indicate roughly an additional suppression of the order of $3 \cdot 10^{-3}$ for each additional nucleon [72, 73]. Figure 5.1 shows the zoomed region of the table of nuclides with the already observed anti-nuclei. The precise measurement of the transverse momentum spectra of these nuclei can shed further light into their production mechanisms. As no stable nuclei with five nucleons exist, the next undiscovered anti-nuclei would be $^6\overline{\text{Li}}$ (stable) and $^6\overline{\text{He}}$ ($\tau = 0.8$s).

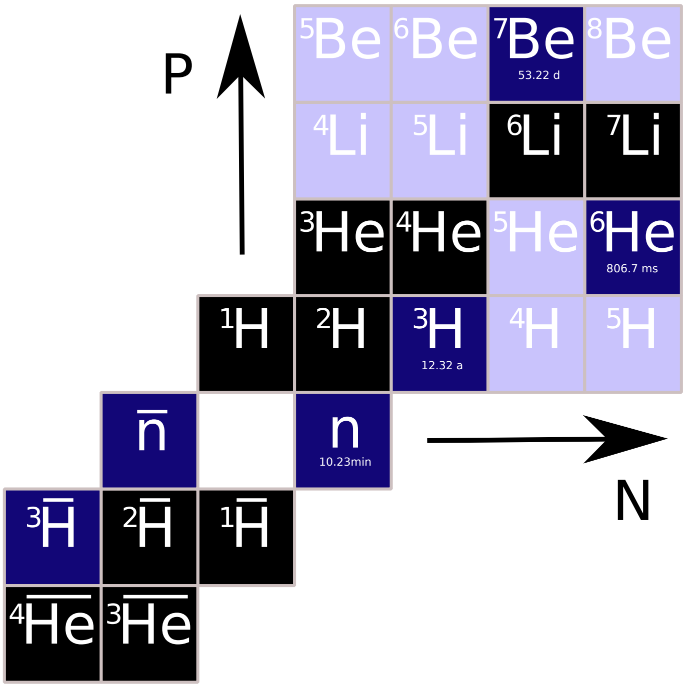

Figure 5.1: Table of nuclides with already observed anti-nuclei. Stable and meta-stable nuclei whose lifetimes are long enough to be detected are shown in black and dark blue, respectively.

5.1 Identification of light (anti-)nuclei

The identification of these rare particles in the large background of charged pions, kaons, and protons is mainly based on the specific energy loss in the TPC. As can be seen in figure 5.2, light nuclei can be clearly separated over a broad momentum range. In the case of light nuclei, the usage of the TPC $\mathrm{d}E/\mathrm{d}x$ signal is mandatory, not only to remove the mismatch in the TOF system, but also because it is the only way to separate charges via the $\mathrm{d}E/\mathrm{d}x \propto z^2$ dependence of the energy loss. The energy loss of $z > 1$ particles is therefore at least four times larger than for minimum ionizing particles with $z = 1$.

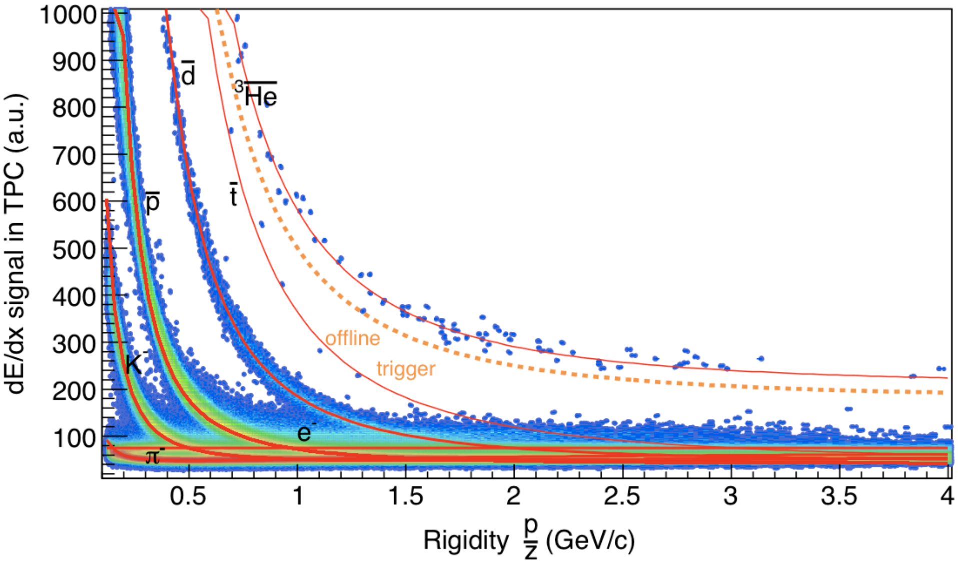

Figure 5.2: dE/dx spectrum of the ALICE TPC of 2.2 million Pb–Pb events.

In contrast to anti-nuclei, the raw spectra of light nuclei suffer from a serious contamination of knock-out particles from detector material. A similar problem is faced in the extraction of proton spectra, but the signal-to-background is worse the heavier the investigated nuclei. Figure 5.3 shows the dca-to-vertex distributions for deuterons integrated over the whole momentum range where clean identification of deuterons is possible. The flat plateau from knock-out nuclei is clearly visible. The contamination from material in the deuteron spectrum amounts to about 4-6% at $p_t = 700$ MeV in pp collisions. At a similar $m_t - m_0$ the contamination for protons is only 1-2%. In Pb–Pb collisions, the contamination is significantly increased due to the wrong association of fake ITS clusters which leads to a similar peak in the dca-distribution of knock-out nuclei from material as shown in figure 3.8. Further details of light nuclei identification and analysis can be found in [74].

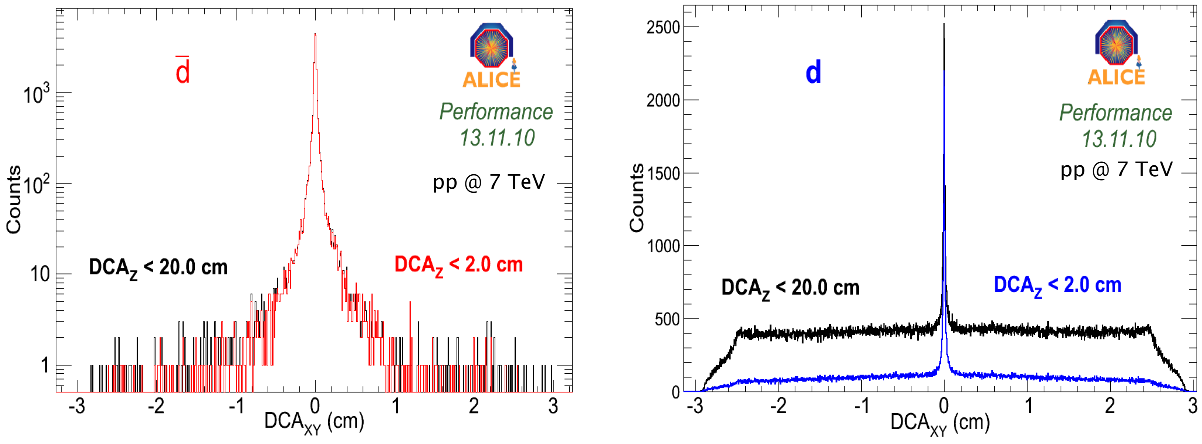

(a) (b)

Figure 5.3: dca$_{xy}$ to primary vertex distribution of anti-deuterons (left) and deuterons (right). The plateau from knock-out nuclei in the deuteron distribution is clearly visible.

Knock-out nuclei from material can also present a problem for the identification of anti-nuclei because of back-scattering. If the light nucleus is produced in a spallation reaction in the material behind the TPC and its flight path is directed back to the TPC, it will be reconstructed as a negative particle. As can be seen from typical dca-to-vertex distributions, the probability of these processes is very small, but a standard cut to select primary particles (see equation 3.4) also has to be applied for anti-nuclei. Alternatively, this contribution can be removed with the help of the time-of-flight information.

5.2 Observation of $^4\overline{\mathrm{He}}$-nucleus candidates

The ALICE experiment also observed four candidates of the $^4\overline{\mathrm{He}}$-nucleus, the measurement of which was recently published by the STAR collaboration [75]. In total, 17.8 million nuclear collisions recorded in the heavy-ion run of November 2010 were analyzed with an offline trigger selecting all $^3\overline{\mathrm{He}}$-nuclei or heavier. Figure 5.4 shows the $\mathrm{d}E/\mathrm{d}x$ versus rigidity distribution for negative particles in the region where the bands of $^3\overline{\mathrm{He}}$ and $^4\overline{\mathrm{He}}$ are clearly visible. Below a rigidity of $p/z \approx 2.2$ GeV two candidates are clearly identified only based on the $\mathrm{d}E/\mathrm{d}x$ information. Above, the mass determination of the candidate tracks must be combined with the particle identification based on the TOF system following

$$m^2/z^2 = R^2/(\gamma^2 - 1)\,. \tag{5.1}$$

The inset in figure 5.4 shows the $\frac{m^2}{z^2}$ distribution for all tracks within a 2σ-band around the expected $\mathrm{d}E/\mathrm{d}x$ for $^4\overline{\mathrm{He}}$. The four anti-alpha candidates are highlighted in red in both the $\frac{m^2}{z^2}$ and the $\mathrm{d}E/\mathrm{d}x$ versus rigidity plot. The $\mathrm{d}E/\mathrm{d}x$ cut selects particles such that only tracks with $z = 2$ are contained in the sample which removes the ambiguity with deuterons (see eq. 5.1). The observed raw ratio of approximately 1000 $^3\overline{\mathrm{He}}$ nuclei with respect to four $^4\overline{\mathrm{He}}$ candidates is in rough agreement with thermal model expectations [73].

5.3 Transverse momentum spectra of light (anti-)nuclei

After the identification with appropriate 3σ-cuts based on the TPC particle identification and similar track quality cuts as presented in chapter 3, the raw p_t-spectra of anti-deuterons, anti-tritons, and $^3\overline{\mathrm{He}}$ can be directly extracted. The raw spectra for deuterons, tritons, and ^{3}He are obtained from a fit to the dca_{xy}-distribution for each individual p_t-bin. In contrast to the extraction of the proton spectrum, the material contamination is removed with a flat fit to the tails of the dca_{xy}-distribution outside the signal region [74]. This procedure is only precise enough for pp events where the wrong association of ITS clusters due to combinatorics is negligible. The usage of template fits similar to the procedure outlined in chapter 3 is currently under study and is mandatory for the extraction of final spectra in Pb–Pb collisions at low transverse momenta. Towards higher momenta the contamination becomes smaller and is negligible above 2.5-3 GeV for ^{3}He.

5.3.1 Efficiency correction

In contrast to other analyses, the efficiency correction can not be obtained from standard MC productions based on e.g. particle generation with PHOJET and propagation with GEANT3. As neither primary (anti-)nuclei nor (anti-)hyper-nuclei are produced by standard generators like HIJUNG, PHOJET, Pythia, AMPT, and others, these particles have to be injected on top of ordinary events. This can

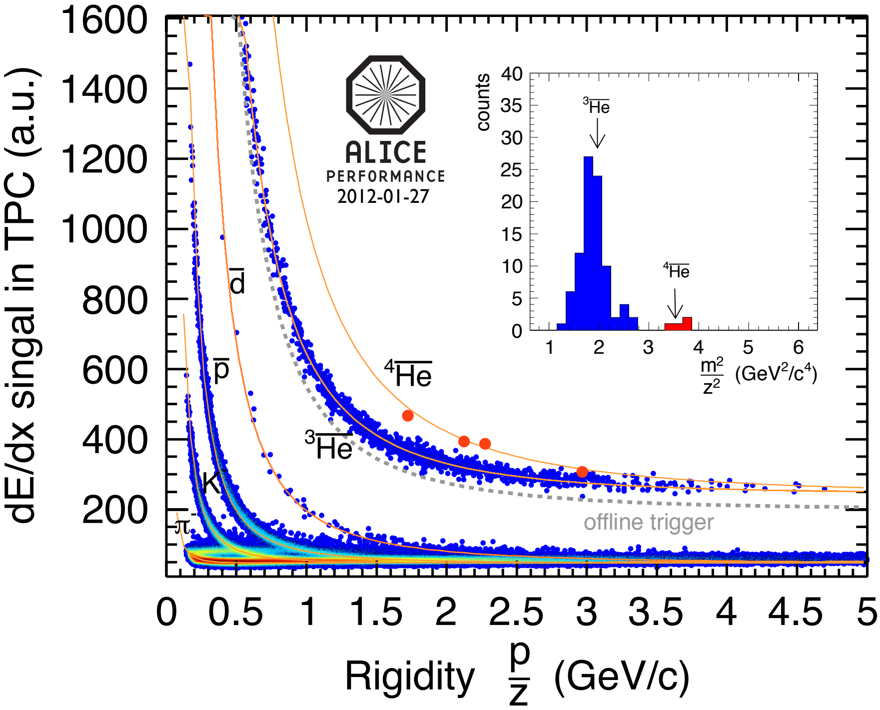

Figure 5.4: dE/dx spectrum of the pre-selected events (by the offline trigger) in the full statistics of 2010 Pb–Pb data (18 million nuclear interactions).

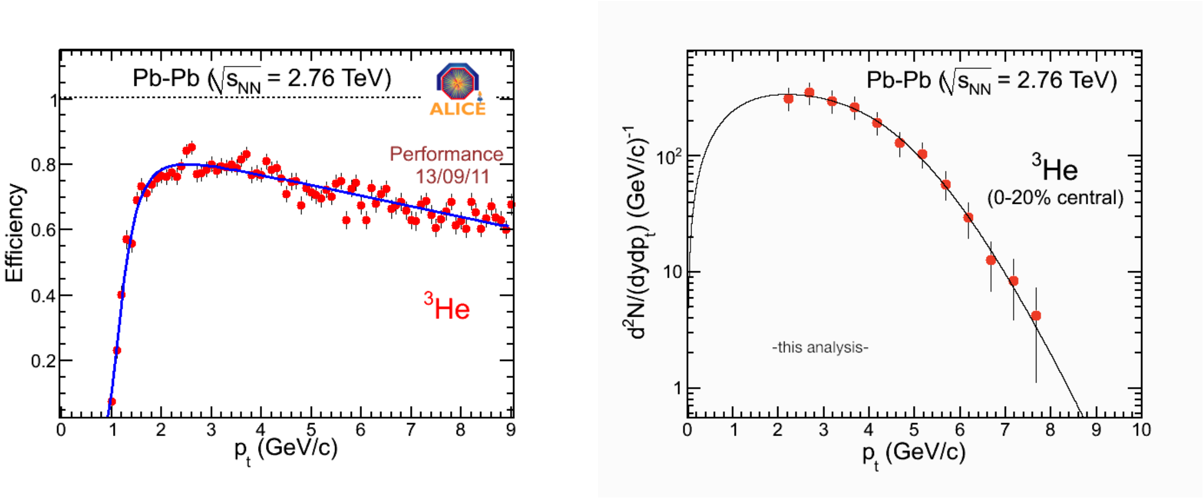

(a)

(b)

Figure 5.5: Efficiency for ^{3}He-nuclei in Pb–Pb collisions (left). Corrected transverse momentum of ^{3}He in the 0-20% centrality bin and exponential fit function (right).

either be done with a flat p_t and rapidity distribution or based on a blast-wave approximation of the spectrum (see chapter 6).

An additional complication is given by the hadronic cross sections for light (anti-)nuclei which are implemented in GEANT3. The description for nuclei is already reasonable in the standard configuration. The reliability can be cross-checked with a model which builds the hadronic cross sections for (He,A) by combining measured (p,A) and (n,A) cross-sections [76]. The differences in the final efficiency remain below the 5% level for the total efficiency and can be taken into account in the systematics for nuclei propagation [77]. The situation is more complicated for anti-nuclei, as no data exists on e.g. ($^3\overline{\mathrm{He}}$,A) interactions. The standard implementation of GEANT3 does therefore not include this effect. There are several possible attempts to model this interaction and to patch GEANT3, e.g. again by combining ($\bar{p}$,A) cross-sections as in [76]. However, it is not clear how reliable these approximations are. In future, it might be possible to test the precision of transport codes for anti-nuclei by measuring the absorption of anti-nuclei due to hadronic interaction in the known material budget of the TRD.

5.3.2 Corrected spectra

Figure 5.5(a) shows exemplarily the obtained efficiency for ^{3}He. The definition of the efficiency is the same as in chapter 3. A preliminary version of the corrected spectrum for ^{3}He in the 0-20% centrality bin is shown in figure 5.5(b). Please note, that no-feed down correction was applied in order to account for feed-down from $^3_\Lambda$H decays. The contamination shows similar characteristics as the lambda feed-down into protons, but it is of smaller magnitude because of the smaller branching ratio (see section 5.5). The spectrum can also be fitted with a blast-wave parameterization in order to extract yields and mean transverse momenta.

5.4 A trigger for light nuclei

Like any investigation of rarely produced particles, the available statistics of (anti-)nuclei could be drastically enhanced by the usage of high or low level triggers. While low level triggers increase the number of actually inspected events, high level triggers only reduce the data sample which has to be processed by the offline reconstruction and data analysis.

5.4.1 Low level – nuclei triggered with the TRD

The Transition Radiation Detector is designed to provide a trigger on high-p_t electrons, in particular to enhance the data sample for quarkonia such as J/ψ and Υ [78]. While the online tracklet reconstruction provides basic information about the rigidity of the inspected tracks, the different particle species can be distinguished with the amplitude of the signal. Due to the presence of transition radiation in the electron signal, it is significantly enhanced with respect to the signal expected from energy loss as illustrated in figure 5.6. The trigger thresholds can thus be adjusted to select electrons and reject the other hadrons. Therefore, a trigger with slightly higher thresholds will also select particles with $z > 1$ whose energy loss is at least a factor four larger than for minimum ionizing particles. A preliminary version of trigger was already flagging events during the 2011 Pb–Pb data taking and its performance is currently evaluated [79].

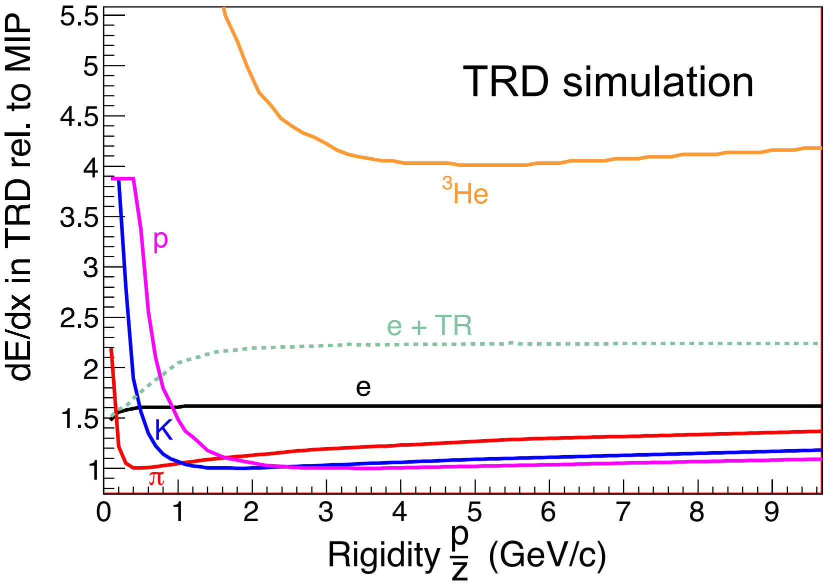

Figure 5.6: Expected energy loss signal of different particle species in the TRD based on GEANT3 calculations.

5.4.2 High level – TPC dE/dx in the HLT

The offline trigger which is also illustrated in figures 5.2 and 5.4 can also be run in the High Level Trigger system to select events with at least one $z > 1$ particle already online. This can drastically reduce the amount events to be stored and processed by the offline reconstruction. In order to achieve this, the calculation of the TPC $\mathrm{d}E/\mathrm{d}x$ signal has to be fast enough to be run online with the data taking on the HLT computer farm. As it turns out, the computation of the 25 integrals in equation 2.19 is too slow as it evolves a corresponding number of evaluations of error functions. A further speed-up of the error function evaluation based on look-up tables in the *ROOT* software package might be implemented in future. As a consequence, the $\mathrm{d}E/\mathrm{d}x$-calculation based on Q_{max} is currently used in the online track reconstruction. It was proven to be fast enough in pp collisions during several test-runs in the 2011 pp data taking.

In general, the online $\mathrm{d}E/\mathrm{d}x$-calculation will have to rely on calibration parameters which are available online. The triggering or flagging of light nuclei has the clear advantage that it does not require an optimal calibration due to the large separation of $z > 1$ nuclei from the rest of all other particles. More sophisticated triggers as for example a selection of low momenta electrons for the reconstruction of low mass di-leptons will require an as precise as possible calibration. Simple corrections like the pressure dependence shown in figure 2.14 should therefore be applied online.

5.5 Hyper-nuclei

The table of nuclides can also be extended in the third dimension by the inclusion of hyper-nuclei in which at least one hyperon is bound in addition to ordinary nucleons. In high energy heavy-ion collisions, their production rates are similar to those of the corresponding nuclei with the same number of nucleons. As a consequence, only the lightest (anti-)hyper-nuclei can be observed within the ALICE experiment. Therefore, the following hyper-nuclei and the corresponding anti-hyper-nuclei and decay channels are of particular interest:

$$\Lambda\mathrm{n} \longrightarrow \mathrm{d} + \pi^- \tag{5.2}$$

$$\Lambda\Lambda \longrightarrow \Lambda + \mathrm{p} + \pi^- \tag{5.3}$$

$${}^{3}_{\Lambda}\mathrm{H} \longrightarrow {}^{3}\mathrm{He} + \pi^- \tag{5.4}$$

$${}^{3}_{\Lambda}\mathrm{H} \longrightarrow \mathrm{d} + \mathrm{p} + \pi^- \tag{5.5}$$

$${}^{4}_{\Lambda}\mathrm{H} \longrightarrow {}^{4}\mathrm{He} + \pi^- \tag{5.6}$$

$${}^{4}_{\Lambda}\mathrm{He} \longrightarrow {}^{3}\mathrm{He} + p + \pi^- \tag{5.7}$$

$${}^{5}_{\Lambda}\mathrm{He} \longrightarrow {}^{4}\mathrm{He} + p + \pi^- \,. \tag{5.8}$$

The measurement of the relevant branching ratios provides in itself an interesting research topic as the currently available values are mostly based on theoretical calculations. The two lightest objects, Λn and $\Lambda\Lambda$, have not been observed so far, but the search for these objects within the ALICE experiment is presented in section 5.5.2. In addition to this, it might be possible to study double (anti-)hyper-nuclei such as:

$${}^{4}_{\Lambda\Lambda}\mathrm{H} \longrightarrow {}^{4}_{\Lambda}\mathrm{He} + \pi^- \tag{5.9}$$

$${}^{5}_{\Lambda\Lambda}\mathrm{H} \longrightarrow {}^{5}_{\Lambda}\mathrm{He} + \pi^- \tag{5.10}$$

$${}^{6}_{\Lambda\Lambda}\mathrm{He} \longrightarrow {}^{5}_{\Lambda}\mathrm{He} + p + \pi^- \,. \tag{5.11}$$

Please note that – in contrast to ordinary nucleons – (anti-)hyper-nuclei with five nucleons are existing. Most of the decay channels contain a ^{3}He or ^{4}He daughter which can be cleanly identified in the TPC as shown in the previous section. The available statistics for (anti-)hyper-nuclei studies would thus also be significantly increased by triggering on light (anti-)nuclei as presented in the previous section. In contrast to lower energy experiments such as FINUDA, FOPI, HYPHI etc., the observation of anti-hyper-nuclei has the advantage that the track sample is not contaminated by knock-out nuclei from material.

5.5.1 (Anti-)Hyper-triton

The anti-hyper-triton ${}^{3}_{\Lambda}\overline{\mathrm{H}}$ is the lightest anti-hyper-nucleus. It was first observed by the STAR experiment [80]. Details of the analysis within the ALICE experiment can be found in [81]. The analysis is based on techniques which are also used for the Λ-reconstruction as outlined in the previous chapter. In order to reduce combinatorics in the investigated Pb–Pb events, track pairs with a minimum distance of closest approach of $DCA < 0.3$ cm are selected. A minimum distance of $R > 0.2$ cm and a maximum distance of $R < 80$ cm is required. Besides standard track cuts, the ^{3}He and π-daughter tracks are selected by 3σ-cuts based on the TPC $\mathrm{d}E/\mathrm{d}x$ signal. Figure 5.7(a) shows the obtained invariant mass distribution.

In addition to the observation of the peak in the invariant mass distribution, the reconstruction efficiency was estimated based on a Monte Carlo simulation of a pure sample of ${}^{3}_{\Lambda}\overline{\mathrm{H}}$ and ${}^{3}_{\Lambda}\mathrm{H}$ decays. The daughter tracks were transported through the detector material with GEANT3. The preliminary result is shown in figure 5.7. Please note, that this estimate of the efficiency can be substantially improved by using GEANT4 for the hadronic interaction of anti-matter with the detector material and

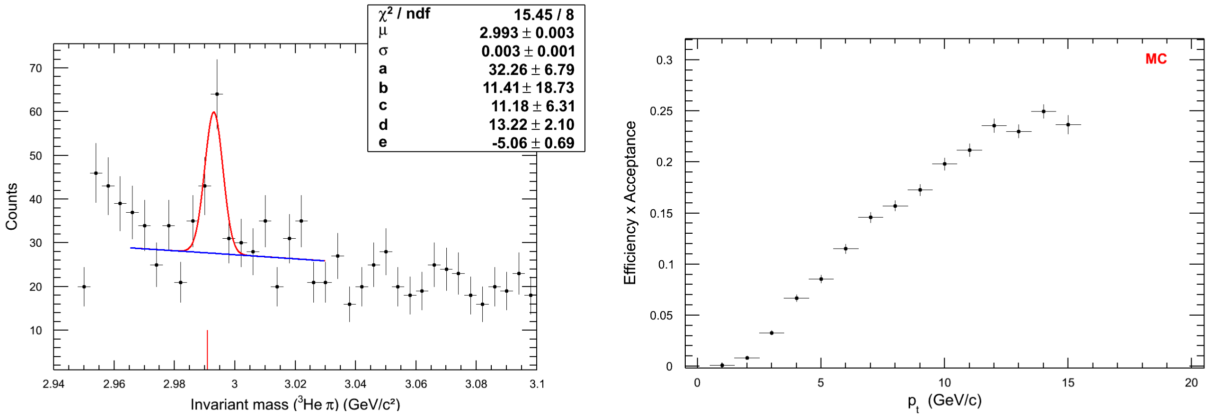

(a) (b)

Figure 5.7: Combined invariant mass distribution of $^{3}_{\Lambda}\overline{\mathrm{H}}$ and $^{3}_{\Lambda}\mathrm{H}$ candidates (left). Estimated efficiency of $^{3}_{\Lambda}\mathrm{H}$ reconstruction in ALICE (right). From [81].

by embedding the $^{3}_{\Lambda}\mathrm{H}$ decays into underlying Pb–Pb events. As not enough statistics for the extraction of a raw p_t-spectrum is available from the statistics of the 2010 Pb–Pb run, the production yield can only be estimated with an assumed p_t-spectrum which is folded with the reconstruction efficiency. One of the possibilities is given by a blast-wave spectrum based on the fit to the pion, kaon, and proton spectra as shown in the following chapter.

5.5.2 Search for unknown states: lambda-neutron bound state and the H^0-dibaryon

The (anti-)hyper-matter studies in the ALICE experiment can be complemented by a search for unknown states. Dibaryon states are of particular interest in this context. Similar to the hyper-triton and the deuteron, one can imagine the existence of a bound state consisting of a neutron and a lambda which decays into a deuteron and a pion with a lifetime that is similar to the lambda and the hyper-triton. A possible bound state of two lambdas is referred to as the H^0-dibaryon. It was first predicted by Jaffe [82] in a bag model calculation and recent lattice QCD calculations also show an evidence [83] with a predicted mass in the 2.2 GeV region.

Lambda-neutron bound state

If we consider the existence of a (anti-)lambda-neutron bound state decaying into a (anti-)deuteron and pion pair, its mass can be restricted between the kinematical limit $m_{min} = m_d + m_\pi = 2.0155$ GeV and the maximum mass of $m_{max} = m_n + m_\Lambda = 2.055$ GeV. Reasonable assumptions for the lifetime of such a particle are given by the lifetime of the hypertriton ($c\tau \approx 5.5$ cm) and the lambda ($c\tau \approx 7.8$ cm). The deuteron tracks originating from the displaced decay vertex can be cleanly identified with the TPC dE/dx signal up to a momentum of $p \approx 1.8$ GeV.

A dedicated MC production with injected lambda-neutron particles is currently planned, but not yet available. Nevertheless, the reconstruction efficiency for such a a particle can be estimated by a comparison of the already determined lambda and hyper-triton reconstruction efficiency. The requirement of a clean particle identification limits the acceptance at high transverse momenta. In the relevant p_t-range, it is thus expected to be at least about 5% and at maximum 20% for particles produced in the rapidity range $|y| < 1$. As not the entire transverse momentum range of the produced

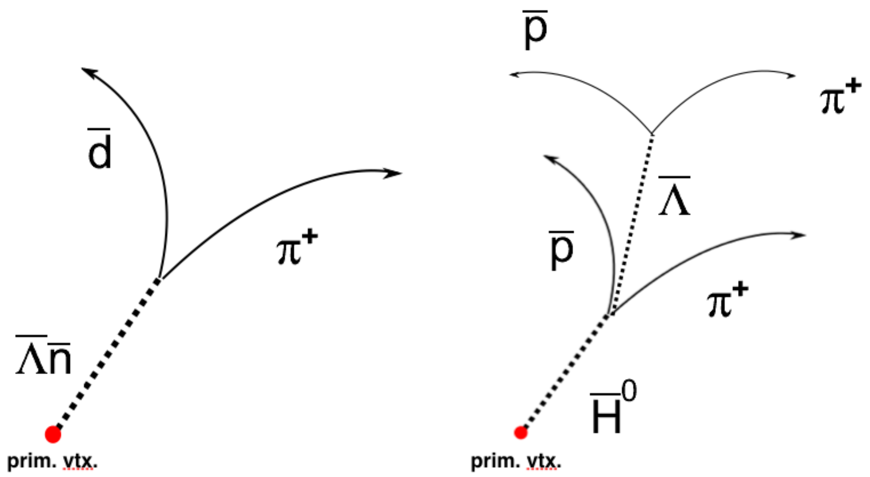

Figure 5.8: Decay topology of the hypothetical lambda-neutron bound state (left) and the H^0-dibaryon (right).

particles is covered, an assumption on the spectral shape has to be made. This can be done with the help of a blast-wave spectrum based on the fit parameters for pions, kaons, and protons resulting in a fraction of about 30% to 40%. Figure 5.9(b) shows the assumed spectral shapes [84]. The production yield of the particle can be approximated based on thermal model calculations as presented in [72, 73]. Assuming a ratio of the lambda-neutron bound state to deuteron production which is similar to the lambda to proton and the hyper-triton to ^{3}He ratio, one deduces a production yield of about $\mathrm{d}N/\mathrm{d}y \approx 2 \cdot 10^{-2}$ per event for a centrality of 0-80%. In an analysis of 14 millions events in this centrality class from the 2010 Pb–Pb run, one should thus be able to reconstruct about 5000 to 20000 decays of lambda-neutron bound states. As the branching ratio for this decay channel is unknown, the branching ratio of the lambda decay into a proton and a charged pion daughter was assumed:

$$N_{\Lambda n,\,rec} = \underbrace{1.4 \cdot 10^7}_{events} \cdot \underbrace{0.05}_{eff.} \cdot \underbrace{0.3}_{mom.\,bin} \cdot \underbrace{0.64}_{BR} \cdot \underbrace{0.02}_{\frac{dN}{dy}} \cdot \underbrace{2}_{dy} = 5376\,. \tag{5.12}$$

Figure 5.9(a) shows the obtained invariant mass distribution for $\bar{d}\pi^+$-pairs. No signal has been observed so far. In order to illustrate the expected signal, a peak from a random generator assuming a Gaussian shape is added. The mass resolution of the invariant mass peak is assumed to be the same as the for the lambda. In future, the analysis will be repeated based on a full MC simulation. A classification of the decay topology in the Armenteros-Podolanski space can be found in appendix D.

H^0-dibaryon

The search for a possible bound state of two lambdas is slightly more complicated than the reconstruction of lambda-neutron bound state due to the different decay topology. Details of the analysis which is currently performed within the ALICE experiment can be found in [85]. Figure 5.8 shows the decay topologies for the lambda-neutron and the H^0-dibaryon. The final state of the H^0 decay chain is given by two proton-pion pairs. In essence, a reconstructed lambda based on V^0 finding techniques has to be combined with a displaced proton and pion. While the calculated lambda flight path is not required to point back to the primary vertex, the reconstructed H^0 momentum vector should. Once

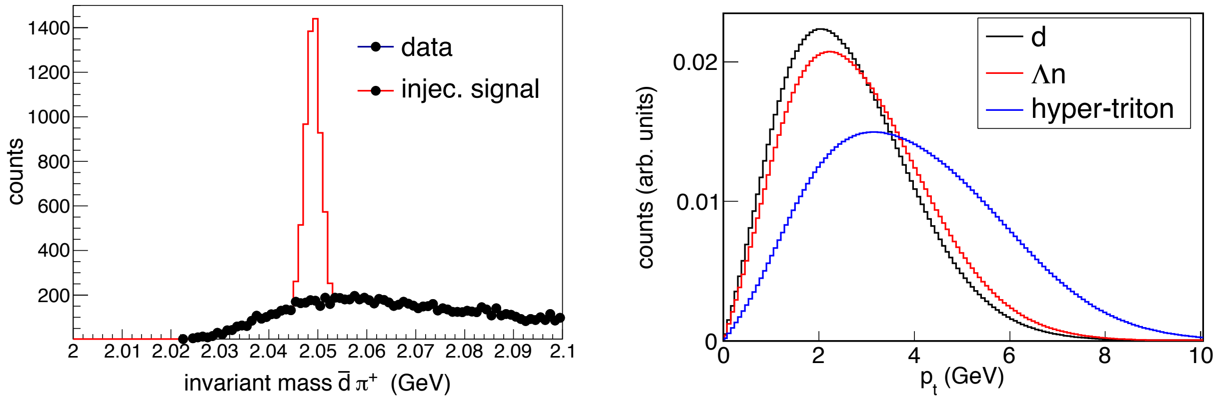

(a) (b)

Figure 5.9: Invariant mass distribution for anti-deuteron and pion track pairs from data (black circles) and with an injected signal of 5000 counts on top of the data (red line). Blast-wave spectra for different particle types based on the common freeze-out parameters for pions, kaons, and protons. From [84] (right).

the thus more complicated reconstruction efficiency can be constrained based on MC simulations, similar estimates as for the lambda-neutron dibaryon can be made for the expected signal.

6 Interpretation of results: hydrodynamical concepts and thermal models

In contrast to other observables, e.g. charm production and high-p_t particles, the bulk of the emitted particles in hadronic collisions consists of soft hadrons from the light quark flavors u, d, and s. Thus their understanding is crucial for the characterization of the global behavior of the collision system. They characterize the chemical and kinetic freeze-out conditions of the collision. In fact, a coherent understanding of the system is impossible without the presented measurements, e.g. the interpretation of $v_2(p_t)$- or HBT-results depends crucially on the φ-averaged spectra of identified hadrons. With the help of the thermal model, the obtained particle production yields can be used to interpret the chemical freeze-out conditions of the fireball. The kinetic properties are extracted from hydrodynamical models and blast-wave fits.

6.1 Hydrodynamical interpretation and blast-wave fits

The general framework of relativistic hydrodynamics was first developed by Landau and is textbook knowledge since then [86]. As already outlined in the introduction, the application of thermal and hydrodynamical to high energy heavy-ion collisions seems natural as many particles of different sorts are produced and form a medium which exhibits a collective behavior. The only requirement for the usage of hydrodynamical tools is given by the assumption of local thermal equilibrium. A comprehensive introduction to relativistic hydrodynamics for heavy-ion collisions can be found in [87].

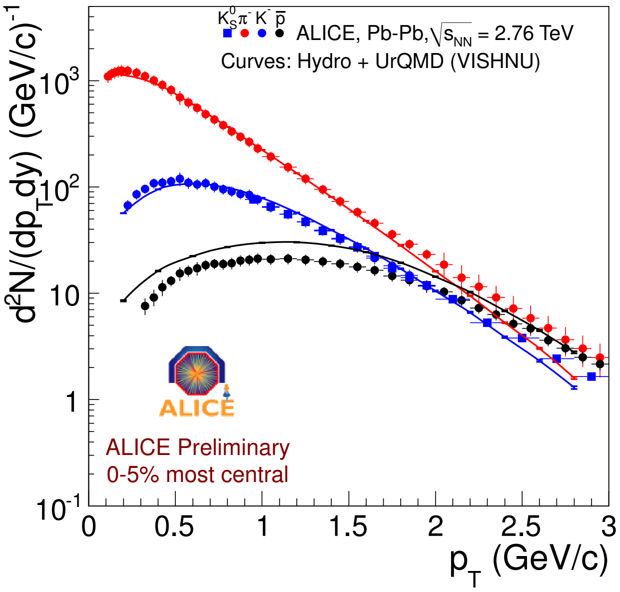

Figure 6.1: Comparison of pion, kaon, and proton spectra with hydrodynamical calculations from [88].

6.1.1 Hydrodynamical calculations

In the ideal fluid scenario, the conservation of energy and momentum,

$$\partial_\mu T^{\mu\nu} = 0\,, \tag{6.1}$$

with the energy momentum tensor $T^{\mu\nu}$ and the conservation of the baryon number current

$$\partial_\mu j_B^\mu(x) = 0\,, \tag{6.2}$$

give five independent equations for the six thermodynamic variables: the energy density $\epsilon(x)$, the momentum density $P(x)$, the baryon number density $n_B(x)$, and the fluid velocity $\vec{v}(x)$. The equation of state - a functional relation between ϵ, P, and n_B- is therefore required to solve the system of equations. In state-of-the-art hydrodynamical calculations, the equation of state is based on lattice QCD calculations [89]. In practice, it turns out that the ideal fluid scenario is only approximate and that dissipative processes play an important role. They lead to correction terms on the right hand side of the equations above in which the shear viscosity η, the bulk viscosity ζ, and the thermal conductivity κ appear. As a matter of fact, the determination of these so-called transport coefficients for the characterization of the QGP is one of the very interesting modern research topics.

The evolution of the partonic phase of the system is described after an thermalization time τ_0 (typically around $\tau_0 \approx 0.6$ fm/c). The transition to particle spectra of hadrons is achieved by an integration of the current density from the hydrodynamic output following a Cooper-Frye prescription [90]. In a second step, the obtained hadrons can be further evolved based on hadronic cascade models, e.g the UrQMD model [91]. Figure 6.1 shows comparison of the hydrodynamical calculation from [88] which shows a good description of the spectral shapes. Please note that the agreement between the shape of the proton spectrum and the model considerably improved after the implementation of the UrQMD model to describe the hadronic phase. Similar observations hold true for the description of the elliptic flow within the same calculation. As the particle yields in this model are based on thermal model calculations, the proton yield is presently slightly underestimated as will be discussed in section 6.2.

6.1.2 Blast-wave fits

A strongly simplified version of the hydrodynamical approach is given by a fit of blast-wave spectra with a single parameter set of (T_{fo}, β, n). A detailed description of the model with a derivation of equation 6.4 can be found in [59]. The model starts from the spectrum of purely thermal sources which are then boosted in transverse direction. The velocity profile in the region $0 < r < R$ is assumed to be of the form

$$\beta_r = \left(\frac{r}{R}\right)^n \beta_t\,, \tag{6.3}$$

where β_t corresponds to the surface velocity and acts as a free parameter of the fit. In many applications, a linear profile is assumed and n is fixed equal to one. In practice, it turns out that the quality of the fit can be improved if n acts as a free parameter, but the resulting values for the kinetic freeze-out temperature T_{fo} and β_t are only slightly affected [59, 84]. The resulting spectrum is a superposition of the individual thermal elements and is given by

$$\frac{1}{m_t}\frac{\mathrm{d}N}{\mathrm{d}m_t} \propto \int_0^R I_0\left(\frac{p_t \sinh\rho}{T_{fo}}\right)\cdot K_1\left(\frac{m_t \cosh\rho}{T_{fo}}\right)\cdot r\mathrm{d}r \tag{6.4}$$

where $I_0(x)$ and $K_1(x)$ represent the modified Bessel functions and $\rho = \tanh^{-1}\beta_r$. Figure 6.2 shows exemplarily the fit with a common parameter set in the 0-5% centrality percentile and the resulting fit parameters in all other centrality bins. The small excess of the data over the fit in the low momenta region of pions is due to feed-down from resonance decays, as e.g. $\rho \to \pi^+\pi^-$.

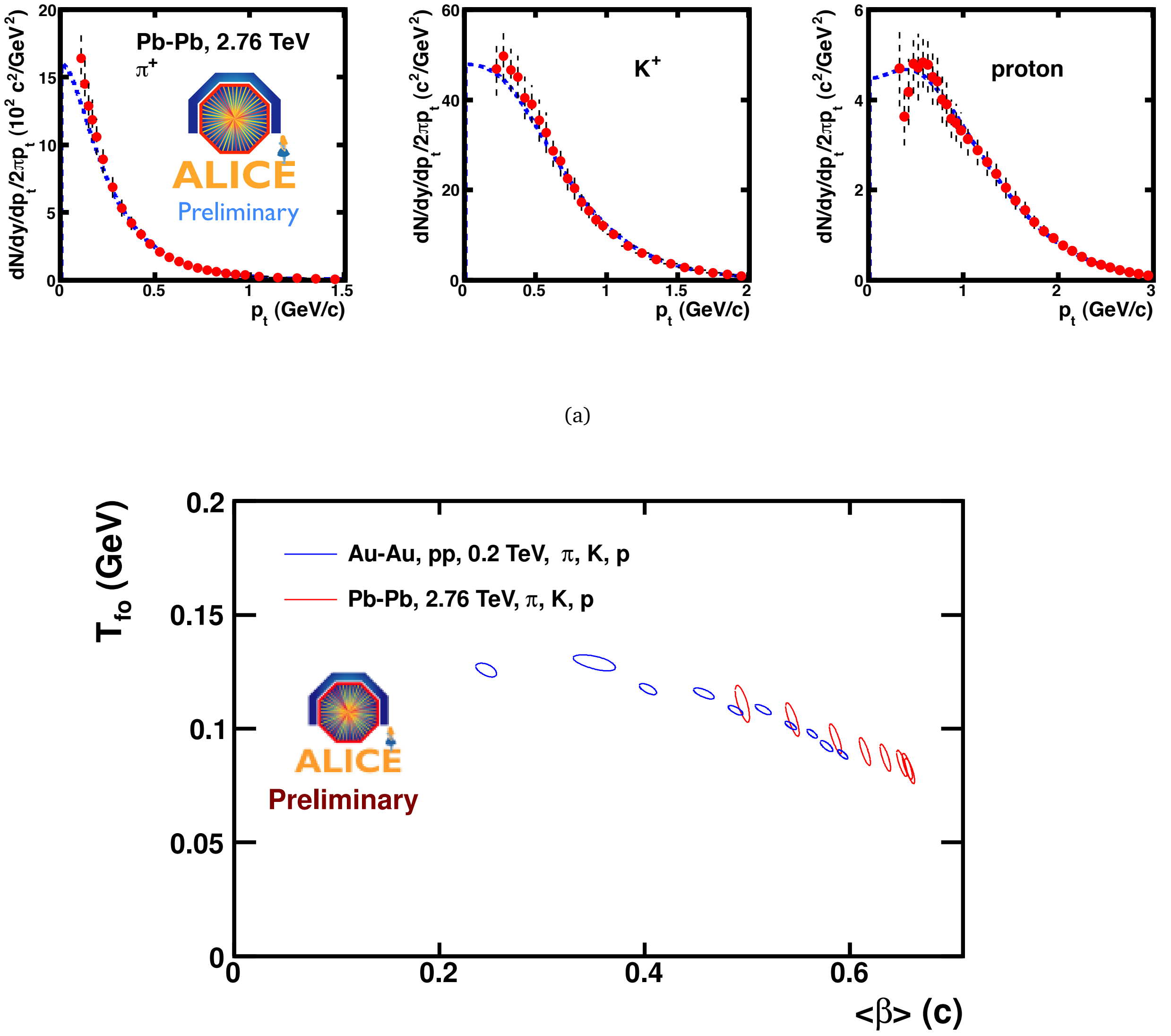

(a)

(b)

Figure 6.2: Blast-wave fit with a common parameter set to pion, kaon, and proton spectra simultaneously in the 0-5% centrality percentile (top). Resulting fit contours (1σ) for the kinetic freeze-out temperature and velocity for different centrality bins compared with the results of a similar analysis of RHIC data (bottom). From [84].

In contrast to full hydrodynamical calculations, blast-wave fits only offer a phenomenological description of identified particle spectra as the model parameters are fit to the data. In addition to this, they do not aim at a simultaneous description of several observables (e.g. v_2 and p_t-spectra). At the same time, they offer the possibility to study systematically the evolution of particle spectra with only three parameters. With a closer look on the functional form in equation 6.4, one finds that the presence of transverse flow effectively leads to a characteristic modification of the spectral shape [92]. Flow increases the particle energies proportional to their rest mass m_i. The spectrum at low momenta ($p_t \ll m_i$) can be described with a correspondingly higher effective temperature T_{eff}. In the non-relativistic limit, one directly obtains the expected scaling $T_{eff} \approx T_{fo} + \frac{1}{2} m_i \langle \beta_s \rangle^2$ [93].

This mass dependent momentum shift with increasing centrality is also clearly visible by looking at the position of the maximum of the spectra in figure 3.17. Another advantage of the blast-wave fits is given by the fact that the obtained parameters can also be used to approximate the spectral shape for any particle i with a given mass m_i. This was extensively used in the previous chapter.

6.2 The thermal model

The observed yields of identified particles in heavy-ion collisions can be correctly described within hadro-chemical equilibrium models over a wide range of beam energies and collision systems [94, 95]. Similar to hydrodynamical calculations, thermal models rely on the fact that the system produced in relativistic heavy-ion collisions behaves like a medium and that concepts from statistical physics can be applied. The starting point of the model is therefore given by the grand-canonical partition function for an ideal relativistic quantum gas of the particle species i

$$\ln Z_{GK_i} = \pm g_i \frac{V}{2\pi^2} \int_0^\infty p^2 \ln\left(1 \pm \exp\left\{-\frac{E_i - \mu_i}{T_{chem}}\right\}\right) \mathrm{d}p \,, \tag{6.5}$$

where g_i corresponds to the spin degeneracy factor, V to the volume of the system, T_{chem} to the chemical freeze-out temperature of the system, μ_i to the chemical potential and E_i to the energy of the particle. The positive sign is valid for fermions and the negative for bosons. For an ideal relativistic gas, the energy for a particle with rest mass m_i is given by $E_i = \sqrt{p^2 + m_i^2}$. The chemical potential $\mu_i = \mu_B B_i + \mu_S S_i + \mu_{I_3} I_3 + \mu_C C_i$ consists of several components corresponding to the conserved quantum numbers in QCD namely the baryon number B_i, the strangeness number S_i, the isospin I_3, and the charm number C_i. With the help of the partition function, all relevant thermodynamic quantities can be calculated, in particular

- the pressure $P = \frac{\partial (T \ln Z_{GK})}{\partial V}$,
- the entropy $S = \frac{\partial (T \ln Z_{GK})}{\partial T}$,
- the energy $E = T^2 \frac{\partial \ln Z_{GK}}{\partial T}$,
- and the particle yield $N = \frac{\partial (T \ln Z_{GK})}{\partial \mu}$.

The chemical potentials μ_S, μ_{I_3}, and μ_C are a priori unknown, but can be determined by conservation laws based on the initial conditions. As the colliding nuclei do not contain any charm or strange quarks, the net strangeness $\sum_i N_i(\mu_S) S_i = 0$ and charm content $\sum_i N_i(\mu_C) S_i = 0$ of the final system must also be equal to zero. For the isospin we obtain correspondingly $\sum_i N_i(\mu_{I_3}) I_{3_i} = \frac{Z-N}{2}$. The only undetermined parameters in this set of equations are the temperature T, the baryo-chemical potential

μ_B, and the volume V of the system. The set of equations can be solved in an iterative calculation. Please note that the yields of all known particle states i from the PDG have to be calculated in each step and then decayed into the states which are defined as stable, e.g. according to Definition 14. In a thermal fit to experimental data, the input values for (T,μ_B,V) are then varied in a minimization procedure in order to reproduce the measured yields. If only particle ratios are of interest or available, the volume is not needed as it cancels in the calculations.

The details of the model implementation can slightly differ between different theory groups. While the authors of [71] use canonical suppression in sub-volumes of the fireball (see next section) to describe the suppression of strangeness in smaller systems, the authors of [96] use a non-equilibrium parameter γ_S^N. The model [70] also applies a correction for the eigen-volume of the particles (similar to a Van-der-Waals gas compared to an ideal gas). In addition to this, it accesses the most complete particle particle set including a larger number of resonances which increases the amount of pions in the final state compared to the kaon yield. This behavior also seems to be favored by the preliminary ALICE data.

Remarkably the chemical freeze-out line extracted via thermal fits to the experimental data from different accelerators coincides with lattice QCD predictions of the phase boundary above top SPS energies. The hadron yields are thus frozen at the phase boundary. A possible explanation could be that many body collisions due to the rapid change in density near the phase transition drive the system to equilibrium [15]. Normal collision rates in the hadronic phase below the critical temperature T_c cannot explain this.

6.2.1 The thermal model in heavy-ion collisions

The chemical freeze-out temperature $T_{chem.}$ and the baryo-chemical potential μ_B are usually determined with a fit to experimental data. However, based on empirical parameterizations of the obtained values for $(T_{chem.}, \mu_B)$ at lower energies, it was possible to predict the particle ratios at LHC energies based on the thermal model [70, 97, 98]. Figure 6.3(a) shows a comparison of the ALICE data in Pb–Pb collisions to the model described in [70] for a temperature of $T = 164$ MeV and a baryo-chemical potential of $\mu_B = 1$ MeV. A perfect agreement between data and model within the systematics uncertainties of the measurement is observed for all particles containing at least one strange valence quark, i.e. K, Ξ, and Ω. The only differences between model and data are found in the preliminary proton yields being approximately 30-40% below the expected value. In future, a very detailed discussion on the uncertainties of the measurement and on the precision of the model will be required to asses the precise magnitude of the deviation.

In this context, it is important to exclude effects related to the specific implementation of the thermal model. Figure 6.3(b) shows a fit with the THERMUS software [99] to the ALICE data where similar trends are observed. Since the baryo-chemical potential is constrained to very small values in the LHC energy regime, a difference in the observed yields can only be compensated by a change in temperature. This would require temperatures of the order of $T \approx 149$ MeV. In this case, the production yields of Ξ and Ω can not be described anymore (see figure 6.3(b)).

From the experimental point of view, further investigations on the applied feed-down corrections - which are substantially larger for protons than for kaons and pions - will help to clarify the discrepancy. Please note, that the proton spectra cannot be as effectively cross-checked as the kaon spectrum which can be compared to K^0_S and the pions which are constrained by a comparison to a spectrum of all charged hadrons. The thermal model calculations will also be more conclusive once more mea-

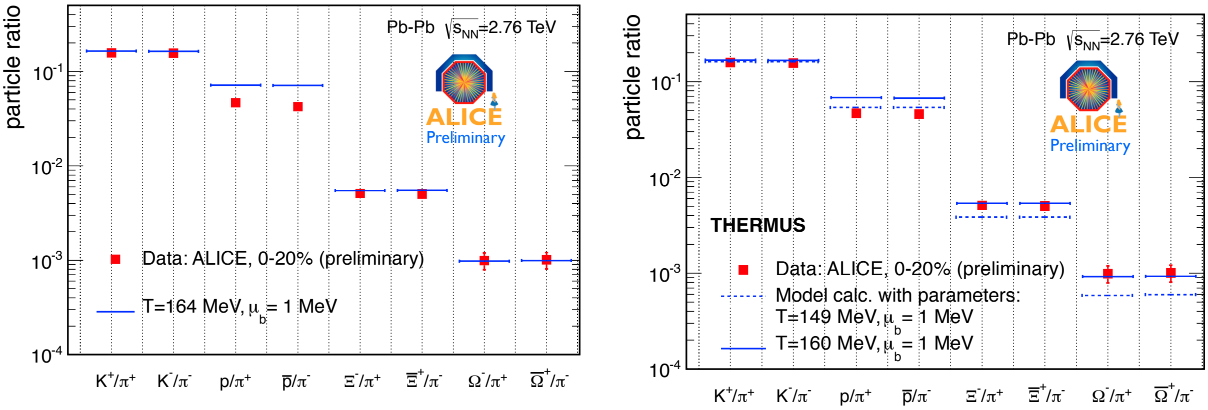

(a) (b)

Figure 6.3: ALICE Pb–Pb data and a calculation with the model from [70] (left). ALICE Pb–Pb data with calculations from the THERMUS code (right).

sured particle yields become available, in particular the measurement of Λs and deuterons in Pb–Pb collisions.

6.2.2 The thermal model in elementary reactions

The thermal concept has been extended to pp collisions requiring a canonical description with additional degrees of freedom which describe a suppression of strangeness beyond the canonical suppression. The strangeness correlation radius R_C can serve as such an additional degree of freedom assuming that strangeness is conserved exactly in correlation volumes which can be smaller than the entire fireball with radius R. The obtained results show similar features as those which are observed in Pb–Pb collisions. Figure 6.4 shows the observed particle yields in pp collisions together with the predictions from THERMUS for two values of R_C [100].

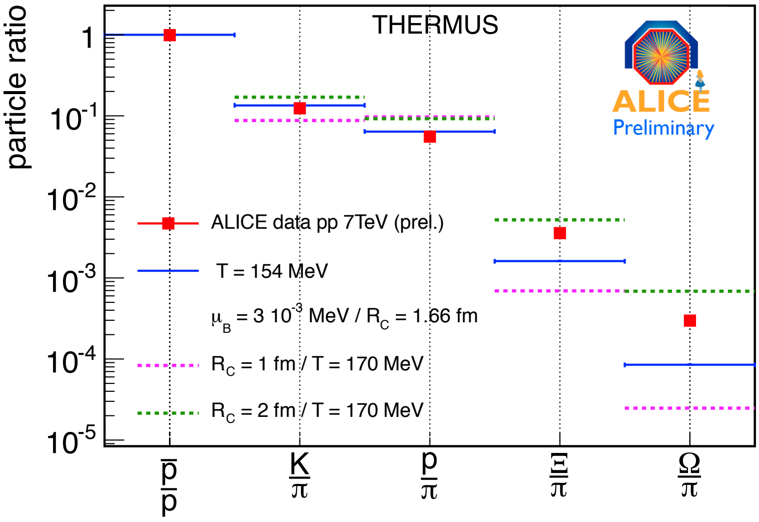

Figure 6.4: Comparison of ALICE pp data at 7 TeV with thermal model calculations from THERMUS.

In particular, the measured proton yield differs in the same way from the model prediction as in Pb–Pb collisions. However, a variation of R_C only influences the strange particle yields and not the p/π-ratio. Despite the absolute value of the p/π-ratio being difficult to describe within a thermal model, the information of the double ratios still remains valid and interesting information can be deduced in the near future with more particle ratios available. In that sense, the p/π-ratio being the same in both collision systems is consistent with model expectations.

6.3 Conclusion and outlook

Thanks to its excellent particle identification capabilities and detector performance, the ALICE experiment was able to provide a full assessment of the production of light flavor hadrons in the LHC energy regime within 2.5 years after the start of data taking. With the help of the sophisticated calibration algorithms presented in the second chapter of this thesis, it was even possible to improve the PID of the Time Projection Chamber beyond its original design values. In addition to this, the implemented calibration procedures are robust enough to run fully automatically so that time-dependent effects can be correctly taken into account without any human intervention.

Despite the preliminary status of some results, several important trends can already be established now. In pp collisions, the observed production yields of pions, kaons, and protons do not change significantly from $\sqrt{s} = 900$ GeV to $\sqrt{s} = 7$ TeV. In particular, the production of strange particles remains strongly reduced with respect to A–A collisions due to canonical suppression. Very interstingly, this observation seems to be also true for high multiplicity pp collisions. In future, a detailed analysis of data with a high multiplicity trigger will allow a direct comparison of pp collisions with peripheral Cu–Cu collisions from RHIC at the same multiplicities. A similar study of the HBT radii is already completed [101]. Both observations seem to indicate that the particles produced in elementary collisions do not show a collective behavior as expected from a medium. In principle, a detailed study based on thermal model fits would allow a further investigation of this question, but an understanding of the discrepancy between model and data in the proton yields is required before. Other analyses, which will be carried out in future, will address the particle composition towards higher momenta based on the relativistic rise of the TPC $\mathrm{d}E/\mathrm{d}x$ signal and the chemistry within jets. Also the investigation of light anti- and hyper-nuclei production in pp collisions is feasible. As a matter of fact, the integrated luminosity which can be inspected in pp collisions might compensate the smaller production yield with respect to Pb–Pb collisions.

The results which were obtained from the analysis of Pb–Pb collisions support in first order the picture of an equilibrated medium which was established at RHIC and SPS energies: the observed particle yields are in agreement with thermal model predictions and the spectral shapes can be described with hydrodynamical calculations. Furthermore, the complete momentum coverage of particle identification and tracking in ALICE now allows tests at very high precision and to look for possible physics beyond the current implementation of these models. The observed differences between the measured proton spectrum and the thermal model expectations could point into that direction, but will require more detailed studies in future. The measurement of light (anti-) nuclei plays an important role in this context as they are the only further baryonic particles which consist only of u and d quarks and which are experimentally easily accessible. This effort will evolve into a complete characterization of the anti- and hyper-nuclei production at LHC energies. Besides a comparison of the measured yields with coalescence and thermal models, this will also include a characterization of the spectral shapes based on blast-wave fits. As shown in chapter 5, all of these studies can be done for nuclei up to the anti-alpha with the present statistics and possibly for hyper-nuclei with mass five in future.

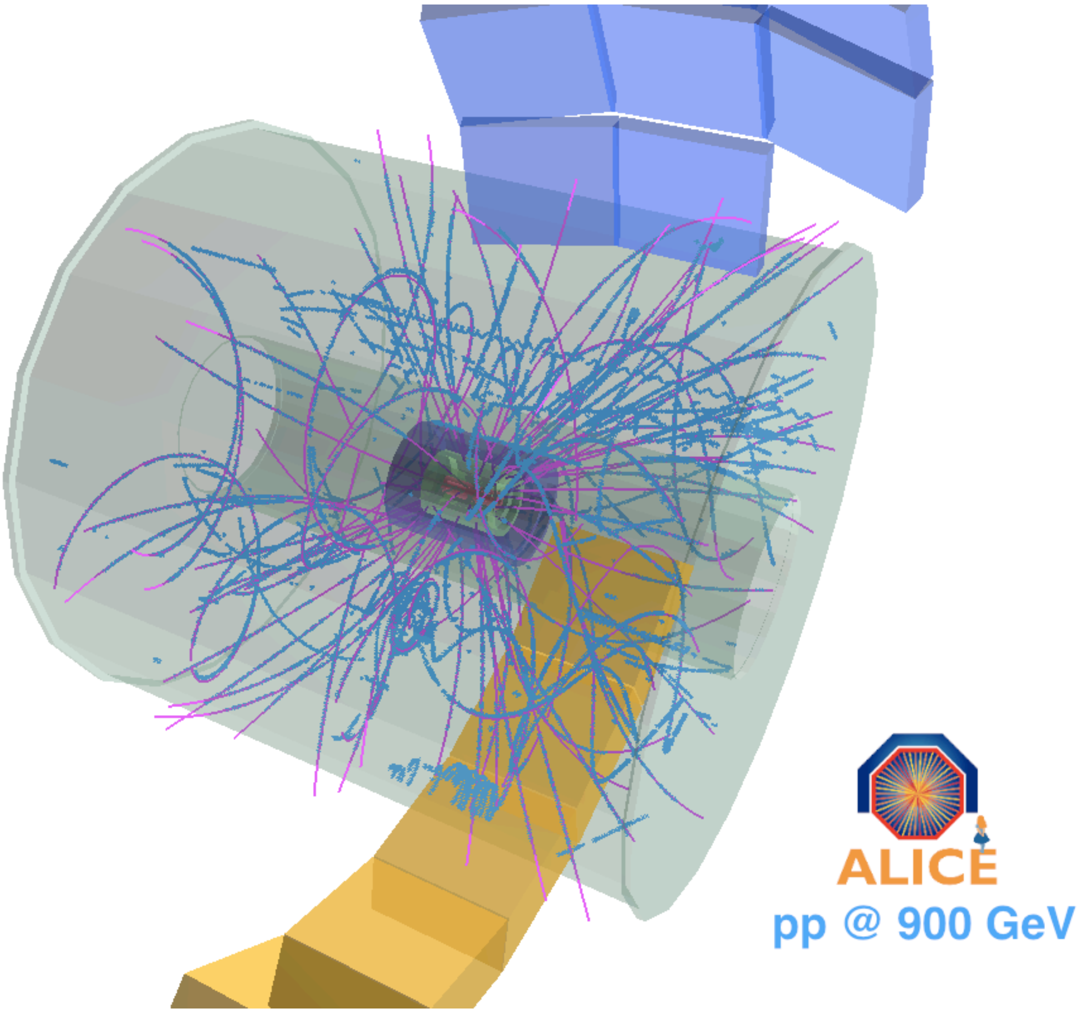

Figure 6.5: One of the first events recorded by the ALICE TPC in December 2009. A pp collision at $\sqrt{s} = 900$ GeV. The blue points represent clusters (see also chapter 2), and the purple lines show the reconstructed tracks.

A The Bethe-Bloch formula

This appendix illustrates basically the $1/\beta^2$ dependence of the Bethe-Bloch equation. In contrast to the calculation by Bethe, the one shown here is a non-relativistic approximation. Figure A.1 shows the basic situation: a projectile particle of charge ze passes a stationary charge Ze in the target.

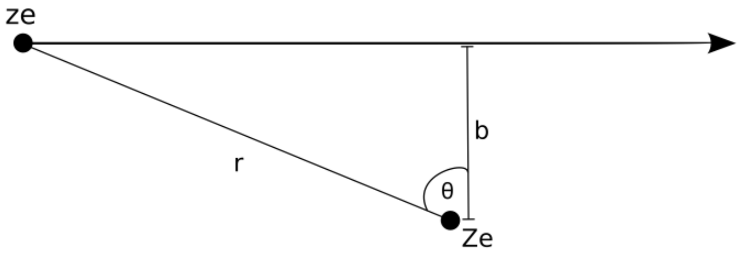

Figure A.1: Schematic illustration of the projectile with charge ze passing by the target with charge Ze.

The force on the projectile in x-direction is then given by

$$F_x = \frac{Zze^2}{r^2}\cos\theta = \frac{Zze^2}{b^2}\cos^3\theta \, . \tag{A.1}$$

The momentum transfer from projectile to target is (the contributions of F_y before and after passing the target cancel each other):

$$\Delta P = \int_{-\infty}^{+\infty} F_x dt = \frac{2Zze^2}{\beta b} \, . \tag{A.2}$$

Since the momentum transfer before and after passing the target charge is equal we find with $r = \sqrt{b^2 + \beta^2 t^2}$:

$$\begin{aligned} \Delta P &= 2\cdot \int_0^{+\infty} \frac{Zze^2 b}{(b^2+\beta^2 t^2)^{3/2}} dt && \text{(A.3)} \\ &= 2Zze^2 b\left[\frac{t}{b^2\sqrt{b^2+\beta^2 t^2}}\right]_0^{\infty} && \text{(A.4)} \\ &= \frac{2Zze^2}{b\beta} \, . && \text{(A.5)} \end{aligned}$$

The transfer of energy is thus

$$\Delta E = \frac{\Delta p^2}{2M} = \frac{(2Zze^2)^2}{2M\beta^2 b^2} \, . \tag{A.6}$$

For an electron with $M = m_e$ and $Z = 1$ we obtain:

$$\Delta E_e(b) = \frac{2z^2 e^4}{m_e \beta^2 b^2} \, . \tag{A.7}$$

This means, that the energy transfer to the target electrons depends on the impact parameter. The number of electrons dn with a certain impact parameter b can be easily calculated:

$$
\begin{aligned}
dn &= 2\pi b \cdot db \cdot (number\, of\, electrons\, per\, unit\, area) && \text{(A.8)}\\
&= 2\pi b \cdot db \cdot Z \frac{N_A}{A} \rho \Delta x \,. && \text{(A.9)}
\end{aligned}
$$

The average over impact parameters can now be calculated as

$$
\begin{aligned}
< \Delta E > &= \int_{b_{min}}^{b_{max}} \Delta E_e(b) \cdot \frac{dn}{db} db && \text{(A.10)}\\
&= 2C \frac{m_e Z z^2}{\beta^2 A} \rho \Delta x [\ln b]_{b_{min}}^{b_{max}} && \text{(A.11)}\\
&= 2C \frac{m_e Z z^2}{\beta^2 A} \rho \Delta x [\ln E]_{E_{min}}^{E_{max}} \,. && \text{(A.12)}
\end{aligned}
$$

The lower limit for energy transfer is the average ionization energy $E_{min} = I_0$ and the upper limit can be calculated from relativistic kinematics $E_{max} \approx 2\gamma^2\beta^2 m_e$ (for particles much heavier than electrons). The final result of the mean energy loss per unit path length in this non-relativistic approach is thus:

$$
< \frac{dE}{dx} >= 2C \frac{m_e Z z^2}{\beta^2 A} \rho \ln \frac{2\gamma^2\beta^2 m_e}{I_0} \,. \tag{A.13}
$$

B The Glauber model

In the Glauber (or *wounded nucleon*) model, the collision between two nuclei A and B is described by a superposition of individual collisions between two groups of nucleons [102, 103]. A brief introduction to the subject together with a small program for the numerical calculations is available at [104]. In general, one distinguishes between optical models which assume a smooth density as presented here and Monte Carlo models in which individual nucleons are stochastically distributed event-by-event (for a recent review see [105]). Both approaches lead to similar results for average quantities, but full Monte Carlo calculations can also model event-by-event fluctuations.

The density distribution of the incoming Pb nuclei can be described with a Woods-Saxon distribution of the form

$$n_A(r) = \frac{n_0}{1 + \exp\left(\frac{r-R}{d}\right)} \tag{B.1}$$

with the exemplarily chosen radius parameter $R = 6.62 \pm 0.06$ fm and the surface diffuseness $d = 0.546 \pm 0.01$ fm. The parameter n_0 is chosen such that the integral of the density corresponds to the number of nucleons N_A of the nucleus:

$$4\pi \int_0^\infty n_A(r)\,\mathrm{d}r = N_A\,. \tag{B.2}$$

We introduce the thickness function $T_A(b)$ which is the integral of the density along the beam axis z for a given impact parameter b

$$T_A(b) = \int_{-\infty}^{\infty} n_A(r = \sqrt{b^2 + z^2})\,\mathrm{d}z\,. \tag{B.3}$$

With the total inelastic nucleon-nucleon cross-section σ_{NN} the number of binary collisions encountered by a single nucleon passing through the target nucleus at impact parameter b can be calculated as $\sigma_{NN} \cdot T_A(b)$. The total number of binary collisions is then given by $N_{coll} = \sigma_{NN} \cdot T_{AB}(b)$ with the so called overlap function

$$T_{AB}(b) = \int T_A(\vec{s})T_B(\vec{s} - \vec{b})\,\mathrm{d}^2s\,. \tag{B.4}$$

at a given impact parameter $\vec{b}$ between the two colliding nuclei.

The number of nucleons which have at least encountered one binary collision is called the number of participants N_{part}. This number becomes easily accessible if we first consider the complementary probability p_0 for a single nucleon at an impact parameter b to pass through the target nucleus without a single collision:

$$p_0 = \left(1 - \frac{\sigma_{NN} T_A}{N_A}\right)^{N_A}. \tag{B.5}$$

We thus obtain for the number of participants

$$N_{part}(b) = \int T_A(\vec{s})\left(1 - (1 - \frac{\sigma_{NN} T_B(\vec{s} - \vec{b})}{N_B})^{N_B}\right)\mathrm{d}^2s + \int T_B(\vec{s})\left(1 - (1 - \frac{\sigma_{NN} T_A(\vec{s} + \vec{b})}{N_A})^{N_A}\right)\mathrm{d}^2s\,. \tag{B.6}$$

The multiplicity distribution of Pb–Pb collisions is then fitted with a two-component model which assumes that the number of particle producing sources is given by $f \cdot N_{part}(b) + (1 - f) \cdot N_{coll}(b)$ with the relative contribution f. Each of these sources produces particles according to a negative binomial distribution with the parameters μ and κ. The values of f, μ, and κ are obtained from the fit.

C The bag model

The temperature T_C of the hadron-parton phase transition can be estimated applying standard thermodynamical concepts on the basis of the bag model [13, 106]. For reasons of simplification, the plasma only consists of u- and d-quarks which corresponds to a gas of free pions in the hadronic phase. Furthermore the mass of these quarks is neglected assuming ($T \gg m$). For the gluons we then obtain with the grand potential for bosons with d degrees of freedom:

$$\frac{\Omega}{V} = d \int \frac{d^3k}{(2\pi)^3} \left\{ T \ln(1 - e^{-E/T}) \right\} + B \,. \tag{C.1}$$

With the assumption of free particles,

$$E^2 = \vec{k}^2 + m^2 \approx \vec{k}^2 \,, \tag{C.2}$$

the integral can be solved analytically:

$$\frac{\Omega}{V} = -d \frac{\pi^2}{90} \cdot T^4 + B \,. \tag{C.3}$$

A similar calculation for the fermionic quarks at $\mu_q = 0$ yields in analogy:

$$\frac{\Omega}{V} = d \int \frac{d^3k}{(2\pi)^3} \left\{ T \ln(1 + e^{-E/T}) \right\} + B = -d \frac{7}{8} \frac{\pi^2}{90} T^4 + B \,. \tag{C.4}$$

For the free pion gas in the hadronic phase the result is simply given by

$$\frac{\Omega}{V} = -d \frac{\pi^2}{90} \cdot T^4 \,. \tag{C.5}$$

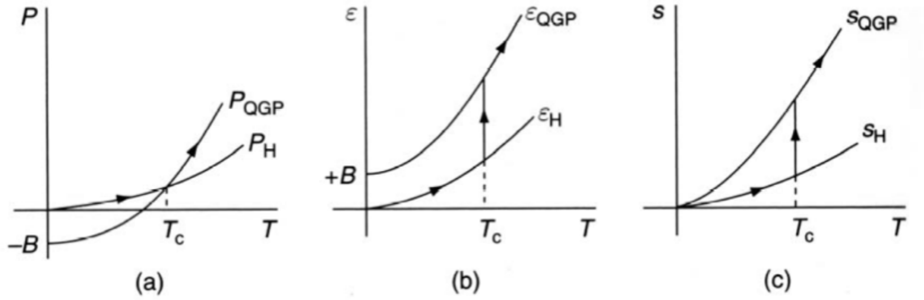

Figure C.1: Behavior of thermodynamic variables in the bag model: pressure (a), energy density (b) and entropy density (c) for the hadron gas phase (H) and quark-gluon plasma (QGP). Picture taken from [13].

The remaining task is to count the degrees of freedom for the different components, i.e. for

- the free pion gas: $d_{pion} = N_{flavors}^2 - 1 = 3$
- the quarks in the deconfined phase: $d_{quark} = 2_{spin} \cdot 2_{q\bar{q}} \cdot N_{color} \cdot N_{flavor} = 24$
- the gluons in the deconfined phase: $d_{gluon} = 2_{spin} \cdot (N_{color}^2 - 1) = 16$.

The equilibrium condition for $\mu = 0$,

$$P_{pion}(T) = P_{QGP}(T)\,, \tag{C.6}$$

leads with $P = -\frac{\Omega}{V}$ to a phase transition (critical) temperature of

$$T_C = \left(\frac{90}{\pi^2} \cdot \frac{B}{34}\right)^{\frac{1}{4}} \approx 158\text{MeV}\,. \tag{C.7}$$

In the bag model, the phase transition is of first order per construction. Figure (C.1) illustrates schematically the jump in energy and entropy density.

D The topology of the Armenteros-Podolanski space

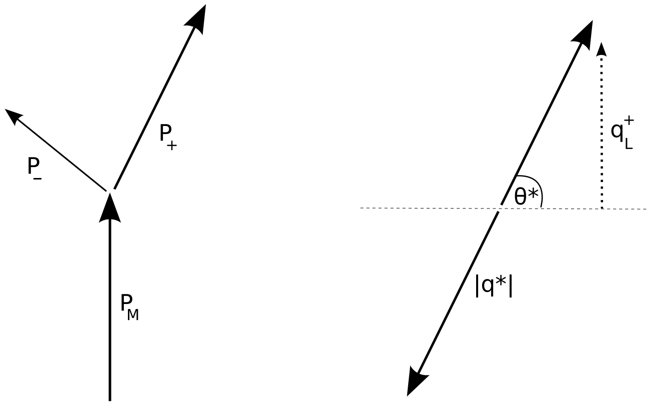

Figure D.1: Schematic representation of the decay topology. Laboratory frame (left) and rest frame of the mother particle (right).

This appendix illustrates why V^0 decays appear as ellipses with different centers and semiaxes in the Armenteros-Podolanski space, and the application of this concept to the decay of the lambda-neutron bound state is shown. The two relevant variables are given by q_T, which represents the transverse component of the positive daughter's momentum $\vec{p}_+$ with respect to the momentum $\vec{p}_M$ of the mother particle,

$$q_T^+ = \frac{|\vec{p}_+ \times \vec{p}_M|}{|\vec{p}_M|}\,, \tag{D.1}$$

and by α, which is a measure of the asymmetry in the longitudinal direction:

$$\alpha = \frac{q_L^+ - q_L^-}{q_L^+ + q_L^-}\,,\; q_L^+ = \frac{|\vec{p}_+ \cdot \vec{p}_M|}{|\vec{p}_M|}\,. \tag{D.2}$$

The momenta of the positive $(+)$ and negative daughter (-) tracks are denoted with q_L^+ and q_T^- where L and T correspond to longitudinal and transverse direction. In the rest frame of the mother particle all quantities are marked with an asterisk. According to figure D.1 we then obtain:

$$q_L^{+*} = |q^*|\cos(\theta^*)\,,\; q_T^{+*} = |q^*|\sin(\theta^*) \tag{D.3}$$

$$E_+^* = \sqrt{|q^*|^2 + m_+^2}\,. \tag{D.4}$$

With the usual transformation for 4-vectors (the relative velocity β between laboratory frame and mother particle defines the direction of the Lorentz boost) we obtain in the laboratory frame:

$$E_+^{lab} = \gamma E_+^* + \beta\gamma q_L^{+*} \tag{D.5}$$

$$q_L^{+lab} = \gamma q_L^{+*} + \beta\gamma E_+^* = \gamma|q^*|\cos(\theta^*) + \beta\gamma E_+^* \tag{D.6}$$

$$q_T^{+lab} = q_L^{+*} = |q^*|\sin(\theta^*)\,. \tag{D.7}$$

Momentum conservation in the mother's rest frame requires $q_L^{+*} = -q_L^{-*}$ and thus

$$q_L^{-lab} = -\gamma|q^*|\cos(\theta^*) + \beta\gamma E_-^*\,. \tag{D.8}$$

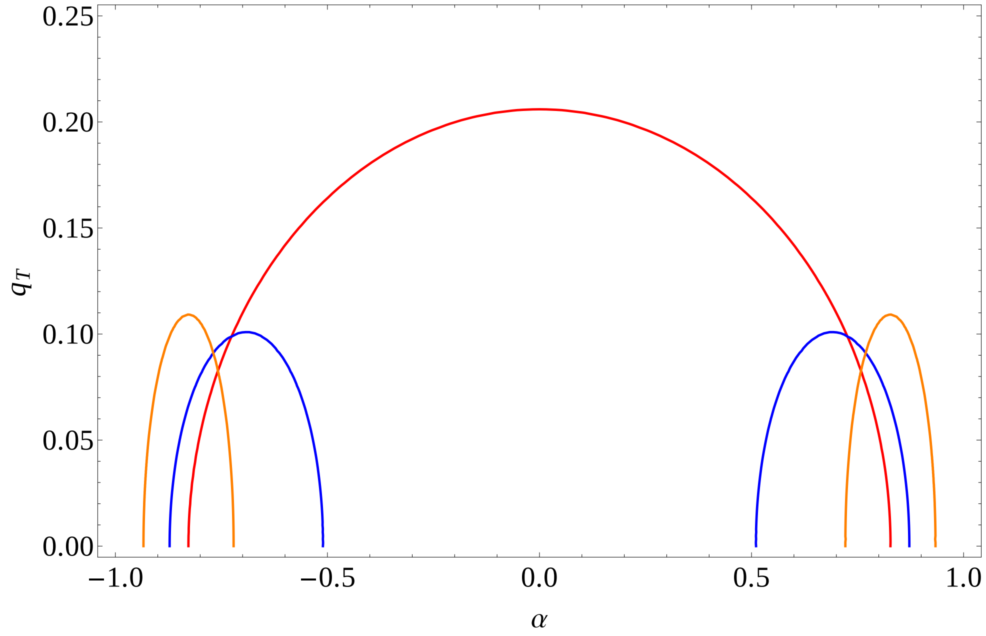

Figure D.2: Expected Armenteros-Podolanski ellipses for the K_S^0 (red), the lambda (blue), and the lambda-neutron bound state (orange). The results shown here correspond to the ultra-relativistic limit $\beta \approx 1$.

By subtracting D.8 from D.6 we obtain

$$q_L^{+lab} - q_L^{-lab} = 2\gamma |q^*| \cos(\theta^*) + \beta\gamma (E_+^* - E_-^*) \,. \tag{D.9}$$

Momentum conservation in the laboratory frame leads to

$$q_L^{+lab} + q_L^{-lab} = |\vec{p}_M| = \beta\gamma m_M \,. \tag{D.10}$$

Now α can be calculated according to its definition by dividing D.9 and D.10:

$$\alpha = \kappa \cos(\theta^*) + \lambda \,, \tag{D.11}$$

where $\kappa = \frac{2|q^*|}{\beta m_M}$ and $\lambda = \frac{E_+^* - E_-^*}{m_M}$. With

$$\sin(\theta^*) = \frac{q_T^{+lab}}{|q^*|} \tag{D.12}$$

and the relation $\sin^2(\theta^*) + \cos^2(\theta^*) = 1$ we finally obtain:

$$\left(\frac{\alpha - \lambda}{\kappa}\right)^2 + \left(\frac{q_T^{+lab}}{|q^*|}\right)^2 = 1 \,. \tag{D.13}$$

This is the formula of an ellipse with semiaxes $\frac{2|q^*|}{\beta m_M}$ and $|q^*|$ and center $(\lambda, 0)$. As a factor β appears in the ellipse parameters, it is not relativistically invariant. Only in the ultra-relativistic limit $\beta \approx 1$ all decays of the same type appear on the same arc.

The momentum $|q^*|$ can be derived from the equation

$$m_M = \sqrt{q^{*2} + m_+^2} + \sqrt{q^{*2} + m_-^2} \,, \tag{D.14}$$

which yields

$$|q^*| = \frac{1}{2m_M}\sqrt{m_M^4 + m_+^4 + m_-^4 - 2m_M^2 m_+^2 - 2m_M^2 m_-^2 - 2m_-^2 m_+^2}\,. \tag{D.15}$$

Figure D.2 shows the thus obtained ellipses for the lambda-neutron bound state, the lambda, and the K_S^0. It is important to notice that crossing points of the arcs correspond to the kinematic situation in which the particles enter each others invariant mass spectrum, if the daughter tracks are wrongly identified.

E Implementation of the dE/dx-calibration in the AliRoot software package

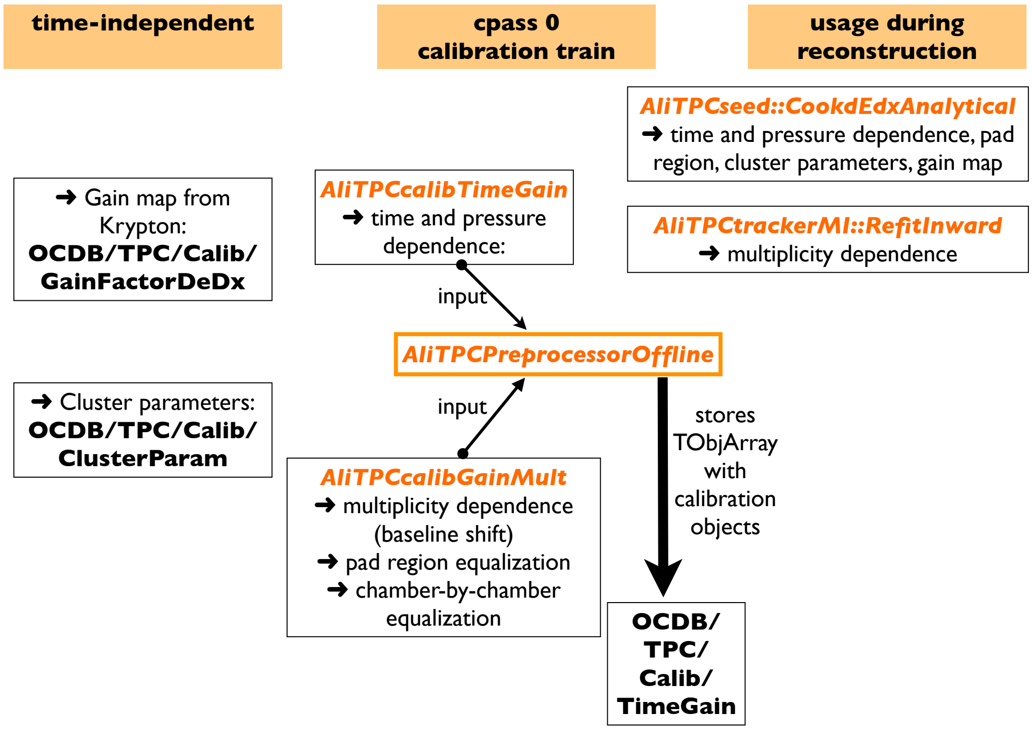

Figure E.1: Schematic illustration of the dE/dx-calibration flow in the *AliRoot* software package.

The implementation of the individual calibration steps in the *AliRoot* software is schematically illustrated in figure E.1. The calibration objects for the krypton gain map and the cluster parameters ($c_0..c_3$ in equation 2.21), whose validity spans longer periods and therefore several runs, are stored in the OCDB in the directories `OCDB/TPC/Calib/GainFactorDeDx` and `OCDB/TPC/Calib/ClusterParam`, respectively. They are manually updated in case of a significant change of chamber voltage etc. Please note, that calibration parameters of the identical type are also applied if simulated events are processed. In practice, it turns out that the values have to be slightly different in order to guarantee an optimal resolution in data as well as in MC. This behavior is natural for microscopic detector simulations as in the case of the ALICE TPC. Details of the microscopic simulator of the ALICE TPC detector response can be found in [22].

The calibration curve for gain variation due to changes of the ambient pressure is extracted within the *cpass0* of the ALICE data reconstruction chain. Before the processing of a data reconstruction pass which can be used in a physics analysis, a subset of the events is fully reconstructed in order to extract the calibration values. An analysis train consisting of several calibration tasks is run over this data. The two tasks which extract the relevant information for the gain calibration are `AliTPCcalibTimeGain` and `AliTPCcalibGainMult`. `AliTPCcalibTimeGain` extracts a spline with the gain vs. time dependence and the correction for electron attachment. The main purpose of `AliTPCcalibGainMult` is to determine the dependence of the dE/dx signal on the event multiplicity which is caused by the baseline shift. In addition to this, all basic information in this class are stored for each read-out chamber individually. Therefore, the gain of individual chambers in the gain map can be updated based on the information in this class. This is in particular important in case a chamber cannot be operated at the nominal voltage in a given run.

The output of `AliTPCcalibTimeGain` and `AliTPCcalibGainMult` from the calibration train is further post-processed in `AliTPCPreprocessorOffline`. In particular, this class is responsible for the automatic update of the OCDB. It summarizes the calibration parameters from the two input classes and stores them in an array of objects. In this step, basic checks on the calibration parameters and outliers are rejected. If the obtained calibration values are within a reasonable range, the objects are send to the calibration database. Please note, that all steps of the entire cpass0 chain are completely automatized.

The usage of the OCDB objects in the next reconstruction pass takes mainly place in the function `CookdEdxAnalytical` in the class `AliTPCseed` which calculates the $\mathrm{d}E/\mathrm{d}x$ signal for every track. It is only the multiplicity dependence which is applied in `AliTPCtrackerMI` as it requires first a full reconstruction of the event in order to determine the multiplicity.

Bibliography

[1] K. Nakamura et al. (Particle Data Group), "The review of particle physics," *J. Phys. G*, vol. 37, p. 075021, 2010.

[2] S. Bethke, "Experimental tests of asymptotic freedom," *Prog. Part. Nucl Phys.*, vol. 58, p. 351, 2007.

[3] D. Gross and F. Wilczek, "Ultraviolet behavior of non-abelian gauge theories," *Phys. Rev. Lett.*, vol. 30, p. 1343, 1973.

[4] H.J. Politzer, "Reliable perturbative results for strong interactions?," *Phys. Rev. Lett.*, vol. 30, p. 1346, 1973.

[5] D. Perkins, *Introduction to High Energy Physics*. Addision-Wesley, 2000.

[6] N. Cabibbo and G. Parisi, "Exponential hadronic spectrum and quark liberation," *Phys. Lett. B*, vol. 59, p. 67, 1975.

[7] J. Collins and M. Perry, "Superdense matter: neutrons or asymptotically free quarks?," *Phys. Rev. Lett.*, vol. 34, p. 1353, 1975.

[8] Y. Aoki, G. Endrodi, Z. Fodor, S. Katz, and K. Szabo, "The Order of the quantum chromodynamics transition predicted by the standard model of particle physics," *Nature*, vol. 443, p. 675, 2006.

[9] A. Bazavov *et al.*, "Equation of state and QCD transition at finite temperature," *Phys. Rev. D*, vol. 80, p. 014504, 2009.

[10] Y. Aoki *et al.*, "The QCD transition temperature: results with physical masses in the continuum limit II," *JHEP*, vol. 06, p. 88, 2009.

[11] K. Aamodt *et al.*, "Charged-particle multiplicity measurement in proton-proton collisions at sqrt(s) = 7 TeV with ALICE at LHC," *Eur. Phys. J. C*, vol. 68, p. 345, 2010.

[12] K. Aamodt et al. (ALICE collaboration), "Centrality dependence of the charged-particle multiplicity density at midrapidity in Pb-Pb collisions at sqrt(s) = 2.76 TeV," *Phys. Rev. Lett.*, vol. 106, p. 032301, 2011.

[13] K. Yagi, T. Hatsuda, and Y. Miake, *Quark-Gluon Plasma: From Big Bang to Little Bang*. Cambridge University Press, 2005.

[14] J. Bjorken, "Highly relativistic nucleus-nucleus collisions: The central rapidity region," *Phys. Rev. D*, vol. 27, p. 140, 1983.

[15] P. Braun-Munzinger, J. Stachel, and C. Wetterich, "Chemical freeze-out and the QCD phase transition temperature," *Phys. Lett. B.*, vol. 596, p. 61, 2004.

[16] P. Braun-Munzinger and J. Stachel, "The quest for the quark-gluon plasma," *Nature*, vol. 448, p. 302, 2007.

[17] P. Pillot, "J/Psi production at forward rapidity in Pb-Pb collisions at $\sqrt{s_{NN}}$ = 2.76 TeV, measured with the ALICE detector," *J. Phys. G*, vol. 38, p. 124111, 2011.

[18] K. Aamodt *et al.*, “Suppression of Charged Particle Production at Large Transverse Momentum in Central Pb–Pb Collisions at $\sqrt{s_{NN}} = 2.76$ TeV,” *Phys. Lett. B*, vol. 696, p. 30, 2011.

[19] T. Matsui and H. Satz, “J/psi Suppression by Quark-Gluon Plasma Formation,” *Phys. Lett. B*, vol. 178, p. 416, 1986.

[20] A. Andronic, P. Braun-Munzinger, K. Redlich, and J. Stachel, “Statistical hadronization of heavy quarks in ultra-relativistic nucleus-nucleus collisions,” *Nucl. Phys. A*, vol. 789, p. 334, 2007.

[21] A. Andronic, P. Braun-Munzinger, K. Redlich, and J. Stachel, “Evidence for charmonium generation at the phase boundary in ultra-relativistic nuclear collisions,” *Phys. Lett. B*, vol. 652, p. 259, 2007.

[22] ALICE Collaboration, “Time Projection Chamber, Technical Design Report,” tech. rep., CERN, 2000.

[23] W. Blum and L. Rolandi, *Particle Detection with Drift Chambers*. Springer, Berlin, 1998.

[24] D. Vranic. Private communication.

[25] W. R. Leo, *Techniques for Nuclear and Particle Physics Experiments*. Springer, 1994.

[26] H. Bethe, “Zur Theorie des Durchgangs schneller Korpuskularstrahlen durch Materie,” *Annalen der Physik*, vol. 397, p. 325, 1930.

[27] L. Landau, “On the energy loss of fast particles by ionization,” *Jour. of Phys. (USSR)*, vol. 8, p. 201, 1944.

[28] H. Bichsel, “A method to improve tracking and particle identification in TPCs and silicon detectors,” *Nucl. Instr. a. Meth. A.*, vol. 562, p. 154, 2006.

[29] R.E. Kalman, “A new approach to linear filtering and prediction problems,” *Trans. ASME, Series D, J. Basic Eng.*, vol. 82, p. 35, 1960.

[30] J. Wiechula, *Commissioning and Calibration of the ALICE-TPC*. PhD thesis, Universität Frankfurt, 2008.

[31] J. Alme et al. (ALICE TPC collaboration), “The ALICE TPC, a large 3-dimensional tracking device with fast readout for ultra-high multiplicity events,” *Nucl. Instr. a. Meth. A*, vol. 622, p. 316, 2010.

[32] R. L. Gluckstern, “Uncertainties in track momentum and direction, due to multiple scattering and measurement errors,” *Nucl. Instr. a. Meth.*, vol. 24, p. 381, 1963.

[33] I. Lehrhaus, R.Matthewson, and W.Tejessy, “Pressure dependence of the relativistic rise in neon and highest attainable ionization sampling resolution in neon, argon, ethylene and propane,” *IEEE Trans. on Nucl. Sc.*, vol. NS-30, p. 50, 1983.

[34] C. Grupen, *Astroteilchenphysik. Das Universum im Licht der kosmischen Strahlung*. Springer, Berlin, 2000.

[35] D. Decamp *et al.*, “ALEPH: A detector for electron-positron annnihilations at LEP,” *Nucl. Instr. a. Meth. A*, vol. 294, p. 121, 1990.

[36] W. Blum, *The ALEPH Handbook CERN-ALEPH-89-077*. CERN Geneva, 1989.

[37] A. De Min *et al.*, “Performance of the HPC calorimeter in DELPHI,” *IEEE Trans. Nucl. Sci.*, vol. 42, p. 491, 1995.

[38] S. Afanasev *et al.*, “The NA49 large acceptance hadron detector,” *Nucl. Instr. a. Meth. A*, vol. 430, p. 210, 1999.

[39] V. Eckardt, T. Eggert, H. Fessler, H. Huemmler, G. L. Curto, M. Oldenburg, N. Schmitz, A. Schuettauf, J. Seyboth, P. Seyboth, and M. Vidal, “Calibration of the STAR forward time projection chamber with krypton-83m.” arXiv:nucl-ex/0101013v2.

[40] E. Mathieson, “Cathode charge distributions in multiwire chambers 4: empirical formula for small anode - cathode separation,” *Nucl. Instr. a. Meth. A*, vol. 270, p. 602, 1988.

[41] W. Diethorn, “A methane proportional counter system for natural radiocarbon measurement,” *USAEC Report*, vol. NY06628, 1956.

[42] F. Sauli, *Principles of Operation of Multiwire Proportional and Drift Chambers*. No. CERN 77-09, CERN, 1977.

[43] W. W. M. Allison and J. H. Cobb, “Relativistic Charged Particle Identification by Energy Loss,” *Ann. Rev. Nucl. Part. Sci.*, vol. 30, p. 253, 1980.

[44] ALICE TPC offline project, “http://www-alice.gsi.de/tpc/pwg1train/lhc11h/pass2/.”

[45] A. Kalweit, “dE/dx calibration of the ALICE Time Projection Chamber,” Master’s thesis, TU Darmstadt, 2008.

[46] K. Aamodt et al. (ALICE collaboration), “Charged-particle multiplicity measurement in proton-proton collisions at $\sqrt{s} = 0.9$ and 2.36 TeV with ALICE at LHC,” *Eur. Phys. J. C*, vol. 68, p. 601, 2010.

[47] K. Aamodt et al. (ALICE Collaboration), “Transverse momentum spectra of charged particles in proton-proton collisions at $\sqrt{s} = 900$ GeV with ALICE at the LHC,” *Phys. Lett. B*, vol. 693, p. 53, 2010.

[48] R.E. Ansorge et al. (UA5 Collaboration), “Diffraction dissociation at the CERN pulsed collider at cm energies of 900 GeV and 200 GeV,” *Z. Phys. C*, vol. 33, p. 175, 1986.

[49] K. Aamodt et al. (ALICE Collaboration), “Strange particle production in proton-proton collisions at $\sqrt{s} = 0.9$ TeV with ALICE at the LHC,” *Eur. Phys. J. C*, vol. 71, p. 1594, 2011.

[50] R. Barlow and C. Beeston, “Fitting using finite monte carlo samples,” *Comp. Phys. Comm.*, vol. 77, p. 219, 1993.

[51] R. Brun, F. Carminati, and S. Giani, “GEANT – detector description and simulation tool,” *CERN-W5013*, 1993.

[52] K. Aamodt et al. (ALICE Collaboration), “Midrapidity antiproton-to-proton ratio in pp collisons at sqrt(s)=0.9 TeV and 7 TeV measured by the ALICE experiments,” *Phys. Rev. Lett.*, vol. 105, p. 072002, 2010.

[53] A. Ferrari, P. R. Sala, A. Fasso, and J. Ranft, “FLUKA: A multi-particle transport code (Program version 2005),” CERN-2005-010.

[54] K. Aamodt et al. (ALICE collaboration), “Validation of the ALICE material budget using photons from pair conversions,” *to be published.*, 2011.

[55] F. Barile, M. Chojnacki, M. Floris, B. Guerzoni, A. Kalweit, L. Milano, R. Preghenella, M. Spyropoulou-Stassinaki, and G. Volpe, “Pion, kaon, and proton spectra in pp and Pb–Pb collisions,” *ALICE internal note*, 2012.

[56] C. Tsallis, “Possible Generalization of Boltzmann-Gibbs Statistics,” *J. Stat. Phys.*, vol. 52, p. 479, 1988.

[57] R. Hagedorn, “Multiplicities, p_t-distributions and the expected hadron → quark - gluon phase transition,” *Riv. Nuovo Cim.*, vol. 6N10, p. 1, 1984.

[58] C. Albajar *et al.*, “A Study of the General Characteristics of Proton - anti-Proton Collisions at $\sqrt{s}$ = 0.2 TeV to 0.9 TeV,” *Nucl. Phys. B*, vol. 335, p. 261, 1990.

[59] E. Schnedermann, J. Sollfrank, and U. Heinz, “Thermal phenomenology of hadrons from 200-A/GeV S+S collisions,” *Phys. Rev. C*, vol. 48, p. 2462, 1993.

[60] D. D. Chinellato, “Multi-strange particle measurements in 7 TeV proton-proton and 2.76 TeV PbPb collisions with the ALICE experiment at the LHC,” *J. Phys. G*, vol. 38, p. 124079, 2011.

[61] M. Nicassio (for the ALICE collaboration), “Multi-strange baryon production in Pb-Pb collisions at $\sqrt{s_{NN}}$ = 2.76 TeV with the ALICE experiment at the LHC (to be published in Proceedings of the Strangeness in Quark Matter conference 2011) ,” *Acta Physics Polonica*, 2011.

[62] K. Aamodt et. al (ALICE collaboration), “Production of pions, kaons and protons in pp collisions at sqrt(s)= 900 GeV with ALICE at the LHC,” *Eur. Phys. J. C*, vol. 71, p. 1644, 2011.

[63] M. Floris (for the ALICE collaboration), “Identified particles in pp and Pb-Pb collisions at LHC energies with the ALICE detector,” *J. Phys. G*, vol. 38, p. 124025, 2011.

[64] B. Abelev *et al.*, “Multi-strange baryon production in pp collisions at $\sqrt{s} = 7$ TeV with ALICE,” *arXiv:1204.0282*, 2012.

[65] S. S. Adler *et al.*, “Identified charged particle spectra and yields in Au + Au collisions at $\sqrt{s_{NN}}$ = 200 GeV,” *Phys. Rev. C*, vol. 69, p. 034909, 2004.

[66] J. Velkowska. Private communication.

[67] B. I. Abelev *et al.*, “Systematic Measurements of Identified Particle Spectra in pp, d+Au and Au+Au Collisions from STAR,” *Phys. Rev. C*, vol. 79, p. 034909, 2009.

[68] L. Barnby. Private communication.

[69] J. Rafelski and B. Muller, “Strangeness Production in the Quark - Gluon Plasma,” *Phys. Rev. Lett.*, vol. 48, p. 1066, 1982.

[70] A. Andronic, P. Braun-Munzinger, and J. Stachel, “Thermal hadron production in relativistic nuclear collisions: The hadron mass spectrum, the horn, and the qcd phase transition,” *Phys. Lett. B*, vol. 673, p. 142, 2009.

[71] J. Cleymans, H. Oeschler, K. Redlich, and S. Wheaton, “Comparison of chemical freeze-out criteria in heavy-ion collisions,” *Phys. Rev. C*, vol. 73, p. 034905, 2006.

[72] J. Cleymans *et al.*, “Antimatter production in proton-proton and heavy-ion collisions at ultra-relativistic energies,” *Phys. Rev. C*, vol. 84, p. 054916, 2011.

[73] A. Andronic, P. Braun-Munzinger, J. Stachel, and H. Stöcker, “Production of light nuclei, hyper-nuclei and their antiparticles in relativistic nuclear collisions,” *Phys. Lett. B*, vol. 697, p. 203, 2011.

[74] N. Sharma, *Measurement of light nuclei production at LHC with the ALICE experiment*. PhD thesis, University of Chandigarh, 2011.

[75] H. Agakishiev et al. (STAR Collaboration), “Observation of the antimatter helium-4 nucleus,” *Nature*, vol. 473, p. 353, 2011.

[76] A. Moiseev and J. Ormes, “Inelastic cross section for antihelium on nuclei: an empirical formula for use in the experiments to search for cosmic antimatter,” *Astropart. Phys.*, vol. 6, p. 379, 1997.

[77] E. Serradilla. Private communication.

[78] ALICE Collaboration, “Transition Radiation Detector, Technical Design Report,” tech. rep., CERN, 2001.

[79] J. Klein. Private communication.

[80] B.I. Abelev et al. (STAR collaboration), “Observation of an Antimatter Hypernucleus,” *Science*, vol. 328, p. 58, 2010.

[81] N. Martin, “Investigation of light (anti-)nuclei and (anti-)hypernuclei with ALICE at the LHC,” Master’s thesis, TU Darmstadt, 2011.

[82] R. L. Jaffe, “Perhaps a Stable Dihyperon,” *Phys. Rev. Lett.*, vol. 38, p. 195, 1977.

[83] S. R. Beane *et al.*, “Evidence for a Bound H-dibaryon from Lattice QCD,” *Phys. Rev. Lett.*, vol. 106, p. 162001, 2011.

[84] K. Schweda and J. Thome. Private communication.

[85] B. Dönigus, *Measurement of the* $\Lambda(1520)$ *resonance and search for dibaryons with the ALICE experiment (working title)*. PhD thesis, TU Darmstadt, 2012 (to be published).

[86] L. Landau and E. Lifshitz, *Fluid Mechanics Course of Theoretical Physics Volume 6*. Pergamon Press, 1959.

[87] J.-Y. Ollitrault, “Relativistic hydrodynamics for heavy-ion collisions,” *Eur. J. Phys.*, vol. 29, p. 275, 2008.

[88] U. W. Heinz, C. Shen, and H. Song, "The viscosity of quark-gluon plasma at RHIC and the LHC," *arxiv 1108.5323*, 2011.

[89] C. Shen, U. Heinz, P. Huovinen, and H. Song, "Radial and elliptic flow in Pb+Pb collisions at the Large Hadron Collider from viscous hydrodynamic," *Phys. Rev. C*, vol. 84, p. 044903, 2011.

[90] F. Cooper and G. Frye, "Comment on the Single Particle Distribution in the Hydrodynamic and Statistical Thermodynamic Models of Multiparticle Production," *Phys. Rev. D*, vol. 10, p. 186, 1974.

[91] S. A. Bass *et al.*, "Microscopic models for ultrarelativistic heavy ion collisions," *Prog. Part. Nucl. Phys.*, vol. 41, p. 255, 1998.

[92] U. W. Heinz, "Concepts of heavy ion physics," *CERN Yellow Report CERN-2004-001*, p. 165, 2004.

[93] R. Scheibl and U. W. Heinz, "Coalescence and flow in ultrarelativistic heavy ion collisions," *Phys. Rev. C*, vol. 59, p. 1585, 1999.

[94] P. Braun-Munzinger, K. Redlich, and J. Stachel, "Particle production in heavy ion collisions.," *Quark Gluon Plasma 3, Eds. R.C. Hwa and Xin-Nian Wang, World Scientific*, p. 491, 2003.

[95] A. Andronic, P. Braun-Munzinger, and J. Stachel, "Hadron production in central nucleus-nucleus collisions at chemical freeze-out," *Nucl. Phys. A*, vol. 772, p. 167, 2006.

[96] F. Becattini, J. Manninen, and M. Gazdzicki, "Energy and system size dependence of chemical freeze-out in relativistic nuclear collisions," *Phys. Rev. C*, vol. 73, p. 044905, 2006.

[97] J. Cleymans, I. Kraus, H. Oeschler, K. Redlich, and S. Wheaton, "Statistical model predictions for particle ratios at $\sqrt{s_{NN}} = 5.5$ TeV," *Phys. Rev. C*, vol. 74, p. 034903, Sep 2006.

[98] I. Kraus, J. Cleymans, H. Oeschler, K. Redlich, and S. Wheaton, "Chemical equilibrium in collisions of small systems," *Phys. Rev. C*, vol. 76, p. 064903, Dec 2007.

[99] S. Wheaton, J. Cleymans, and M. Hauer, "THERMUS - a thermal model package for root," *Comput. Phys. Commun.*, vol. 180, p. 84, 2009.

[100] I. Kraus, J. Cleymans, H. Oeschler, and K. Redlich, "Particle production in p-p collisions and predictions for sqrt(s)=14 TeV at the CERN Large Hadron Collider (LHC)," *Phys. Rev. C*, vol. 79, p. 014901, 2009.

[101] K. Aamodt *et al.*, "Femtoscopy of pp collisions at $\sqrt{s} = 0.9$ and 7 TeV at the LHC with two-pion Bose-Einstein correlations," *Phys. Rev. D*, vol. 84, p. 112004, 2011.

[102] A. Bialas, M. Bleszynski, and W. Czyz, "Multiplicity Distributions in Nucleus-Nucleus Collisions at High-Energies," *Nucl. Phys. B*, vol. 111, p. 461, 1976.

[103] K. Eskola, K. Kajantie, and J. Lindfors, "Quark and Gluon Production in High-Energy Nucleus-Nucleus Collisions," *Nucl. Phys. B*, vol. 323, p. 37, 1989.

[104] D. Miskowiec, "http://www.gsi.de/˜misko/overlap/."

[105] M. L. Miller, K. Reygers, S. J. Sanders, and P. Steinberg, “Glauber modeling in high energy nuclear collisions,” *Ann. Rev. Nucl. Part. Sci.*, vol. 57, p. 205, 2007.

[106] A. Chodos, R. L. Jaffe, K. Johnson, C. B. Thorn, and V. F. Weisskopf, “New extended model of hadrons,” *Phys. Rev. D*, vol. 9, p. 3471, 1974.

Acknowledgements

First of all, I would like to thank my supervisors Prof. Dr. Peter Braun-Munzinger and Priv. Doz. Dr. Helmut Oeschler for their extraordinary support and the possibility to take part in this fascinating experiment. It was certainly a unique and memorable experience to witness the first collisions at the LHC. Special thanks also go to the HGS-HIRE and HQM graduate schools and to Prof. Dr. Henner Büsching for their support and the interesting workshops and lecture weeks.

The senior scientists at GSI, Dr. Ralf Averbeck, Dr. Anton Andronic, Dr. Uli Frankenfeld, and the team leader Dr. Silvia Masciocchi have answered a lot of my questions and also partially proofread the thesis. Special thanks go to my mentor Dr. Dariusz Miskowiec. I also would like to thank the members of the IT department at GSI for providing an excellent environment for data analysis. Similarly, I would like to thank the TPC hardware team for their excellent work in designing, building, and operating the TPC and the many interesting discussions and meetings, in particular Dr. Luciano Musa, Dr. Chilo Garabatos, Dr. Christian Lippmann, Dr. Danilo Vranic, Thomas Mohrhardt, Magnus Mager and Dr. Rainer Renfordt.

My colleagues in the ALICE soft and light flavor physics working group, who worked with me on the physics analysis, should also not be forgotten: Dr. Michele Floris, Dr. Boris Hippolyte, Emanuele Biolcati, Dr. Francesco Noferini, Dr. Marek Chojnacki, Leornado Milano, Dr. Barbara Guerzoni, Dr. Giacomo Volpe, Francesco Barile, and Dr. Roberto Preghenella.

My fellow Ph.D. students Sebastian Huber, Markus Fasel, Michael Knichel, Markus Köhler, Sedat Altinpinar, Juan Castillo, Raphaelle Bailhache, and Christian Schmidt have always been helpful, partially proofread the thesis, and - most importantly - have always been an extremely good company. Special thanks to my former students Nicole Martin and Michael Winn for proofreading the thesis and many interesting discussions. Very Special thanks to Benjamin Dönigus for his encouragement and proofreading the thesis. Thanks also to Dr. Kai Schweda for many important discussions and the blast-wave fits. For many interesting theoretical discussions I would like to thank Prof. Jean Cleymans and Prof. Krzysztof Redlich.

In particular, I would like to thank the members of the TPC offline team who worked with me on the complicated TPC reconstruction and calibration. Very special thanks to my supervisor Dr. Marian Ivanov and to my colleagues Dr. Jacek Otwinowski, Dr. Jens Wiechula, and Jochen Thäder.

Eigenständigkeitserklärung

Hiermit versichere ich, dass ich die vorliegende Doktorarbeit selbstständig und nur mit den angegebenen Quellen und Hilfsmitteln angefertigt habe. Alle Stellen, welche Quellen entnommen wurden, sind als solche gekennzeichnet. Diese Arbeit hat in gleicher oder ähnlicher Form noch keiner Prüfungsbehörde vorgelegen.

(Alexander Kalweit)

Curriculum vitae

Alexander Kalweit

- Born 21 June 1984, Schlüchtern, Germany

- Education:

  Master of Science in Physics, TU Darmstadt, May 2008,
  Thesis title: *dE/dx calibration of the ALICE Time Projection Chamber*

  Bachelor of Science in Physics, TU Darmstadt, June 2006,
  Thesis title: *Investigation of high rate effects in prototypes of the CBM transition radiation detector*

- Professional experience:

  Ph.D. student and research assistant, GSI and TU Darmstadt, since June 2008

  Member of the ALICE collaboration, since April 2007

  Chair of the ALICE-GSI computing meeting, July 2009 - June 2011

  Internship at GSI, *Simulation of high rate effects in resistive plate chambers*, August 2005 - October 2005

  Internship at the University of Frankfurt, Biophysics department, *Development of an analysis device for liquids based on Fourier transform infrared spectroscopy*, July 2003 - October 2003

- Awards:

  Excellence Award of the Helmholtz Graduate School for Hadron and Ion Research for outstanding achievements in the doctoral thesis project, December 2009

- Most important publications[1]:

  1. K. Aamodt et al., “Production of pions, kaons and protons in pp collisions at $\sqrt{s} = 900$ GeV with ALICE at the LHC”, *Eur. Phys. J. C* 71 (6) 1655, 2011.
  2. A. Kalweit (for the ALICE collaboration), “Global properties of strange particle production in pp and Pb–Pb collisions with the ALICE detector”, *Proceedings of Strangeness in Quark Matter 2011*, *Acta Physica Polonica B* 5 (2012) 225.
  3. N. Sharma and A. Kalweit (for the ALICE collaboration), “Light Nuclei and Anti-nuclei Production in pp and Pb–Pb Collisions with ALICE”, *Proceedings of Strangeness in Quark Matter 2011*, *Acta Physica Polonica B* 5 (2012) 605.
  4. J. Alme et al.,“The ALICE TPC, a large 3-dimensional tracking device with fast read-out for ultra-high multiplicity events”, *Nucl. Instrum. Meth. A* 622 (2010) 316-367.
  5. A. Kalweit (for the ALICE collaboration), “Particle Identification in the ALICE Experiment”, *Proceedings of Quark Matter 2011*, *J. Phys. G.* 38 (2011) 124073.
  6. A. Kalweit and M. Ivanov (for the ALICE TPC collaboration), “dE/dx measurements in large volume TPCs”, *Proceedings of the 11th International Conference on Advanced Technology and Particle Physics*, Como 5-9 October 2009, World Scientific, 2010.

---

[1] Only those ALICE papers with a significant contribution are listed.

7. A. Andronic, C. Garabatos, D. Gonzalez-Diaz, A. Kalweit, and F. Uhlig, "A Comprehensive study of rate capability in Multi-Wire Proportional Chambers", *Journal of Instrumentation* 4:P10014, 2009.
8. C. Lippmann, W. Riegler, and A. Kalweit, "Rate effects in resistive plate chamber", *Nucl. Phys. Proc. Suppl.*, vol. 158, pp. 127-130, 2006.

- Talks at international conferences:
    1. *Global properties of strange particle production in pp and Pb–Pb collisions with the ALICE detector*, Strangeness in Quark Matter 2011, Cracow, Poland.
    2. *Particle Identification in the ALICE-Experiment*, Quark Matter 2011, Annecy, France.
    3. *Measurement of p_t-spectra of identified hadrons with the ALICE experiment*, Kruger 2010 - Workshop on Discovery Physics at the LHC, Kruger park, South Africa.
    4. *Strange particle production in pp collisions with the ALICE experiment*, International Workshop on Interplay between Soft and Hard interactions in particle production at ultra-relativistic energies 2010, Catania, Italy.
    5. *First measurement of strange particle production from the ALICE collaboration*, Dense Nuclear Matter 2010 conference, Stellenbosch, South Africa.
    6. *dE/dx measurements in large volume TPCs*, ICATPP conference 2009, Como, Italy.